Chemical and Biochemical Sensors Based on Silicon Nanowire Field-Effect Transistor Arrays

Inauguraldissertation

zur
Erlangung der Würde eines Doktors der Philosophie
vorgelegt der
Philosophisch-Naturwissenschaftlichen Fakultät
der Universität Basel

von

Mathias Wipf
von Dorf (ZH) und USA

UNI
BASEL

Basel, 2014

Genehmigt von der Philosophisch-Naturwissenschaftlichen Fakultät
auf Antrag von
Prof. Dr. C. Schönenberger
PD Dr. M. Calame
Prof. Dr. C. Guiducci
Prof. Dr. S. Zhang

Basel, den 22. April 2014

Prof. Dr. Jörg Schibler
Dekan

Contents

Introduction

In many countries health costs continue to grow faster than national income and sustaining the access to health care and financing at its current level is becoming more challenging to meet growing populations and increasing life expectancy. The rise in chronic diseases and complex medical conditions associated with a rapidly aging population will increase the need for medical specialists, medication and monitoring, and as such, the healthcare industry has become a fast-growing sector. Medical diagnostic tools and the trend towards personalized medicine demand for cheap sensing devices, which offer real-time and parallel detection of various species. For screening and development of new drugs, as well as environmental monitoring and quality control, rapid and portable systems are in demand. There is a strong demand for multiplexed transducers that transform a multiplicity of chemical reactions into electrical signals, which is essential for the cheap detection or monitoring of various analytes.

Advances in biotechnology, microfluidics and micro- and nanotechnology have led to tremendous progress in the advancement of micro analytical systems; however the development of reliable and flexible sensing systems at reasonable cost remains a challenging task. State-of-the-art methods that require labelling are expensive and time-consuming and may possibly interfere with the targeted chemical reactions. Label-free techniques are therefore preferable. Optical systems such as surface plasmon resonance (SPR) have proven their potential to detect specific analytes at extremely low concentrations. However, these systems are difficult to integrate at large-scale and are not ideal for multiplexed sensing, which is important when considering nature's variety of genes and proteins.

Field-effect transistors (FETs) made from semiconducting nanowires (NWs) have great potential as electronic biochemical sensors if they can be integrated as an array in a CMOS-compatible architecture together with microfluidic channels and interfacing electronics. Such nanoscale electronic transducers based on ion-sensitive field-effect transistors could be mass fab-

ricated at reasonable costs. This, in combination with their small size, makes them ideal for personalized medicine and for future implanted sensing devices. During the past decade the principle of the ion-sensitive field-effect transistor (ISFET), proposed in the 1970s by Bergveld et al.[1] experienced a revival at the nanoscale. A huge variety of possible sensor applications such as pH sensing[2–4], chemical[5–10] and label-free biosensing[2,11–15] has been demonstrated by using silicon nanowire field-effect transistors (SiNWFETs). Further, kinetic studies on receptor binding[16] and even intracellular recording of action potentials[17] have been realized by downscaling the devices.

The sensing principle is based on adsorption of charged species on the sensor surface, leading to a change in surface potential and subsequently a change in current in the FET channel. Thereby, the high-impedance input signal is transformed into a low-impedance output signal, which is an advantage against classic ion-selective electrodes. The potential for downscaling and integration for the simultaneous detection of multiple parameters make SiNWFETs a promising platform to meet the demand for cheap, multifunctional and scalable sensors. This has been demonstrated by the recent commercial success of the *Ion Torrent* technology[18] for semiconductor genome sequencing, which allows for the simultaneous detection of independent sequencing reactions by measuring local pH changes in millions of reaction wells. Apart from silicon as basic material, the ISFET concept has also been applied to carbon nanotubes[19–23] and graphene devices[24–29] for pH, ion and protein sensing. Despite their drawback in terms of reproducibility, carbon based ISFETs have interesting properties since no gate oxide is needed for the operation in electrolyte solutions.

Even though many promising results on chemical and biochemical sensing have been achieved so far, a detailed understanding of the electrolyte surface interaction is still missing. Inconsistent outcomes regarding the effect of electrolyte concentrations and electrical noise, suggest that further quantitative studies are needed. The aspect of the size compatibility between the sensor unit and the analyte species is often emphasized to favor nanoscale FETs. Another aspect, often mentioned, is the surface to volume ratio. Hence smaller sensing units should enhance the sensitivity of the sensor[30], allowing the detection at ultra-low concentrations[12,13] or a small number of molecules[31]. Furthermore, the capacitances decrease for smaller sensing units, which could lead to faster response times. However, other aspects such as the intrinsic electronic noise, the analyte diffusion time and surface reaction kinetics have to be considered for the development of an applicable sensor.

This thesis was part of a research project aimed at developing a modular, scalable and integrateable sensor platform for the electronic detection of analytes in solution. Different research groups and scientists have contributed to the results presented here. For the comprehensive scientific findings within the project the reader is referred to the cited literature.

The aim of this work was to establish a versatile sensing platform based on silicon nanowire[1] arrays. The main focus lies on the sensor-solution interface and thus the thesis quantitatively compares the experimental data with analytical models. Chapter 1 gives an introduction to the ISFET theory and discusses the limits of this sensing principle. In Chapter 2, we will present the sample production and the measurement methods. The electrical characterization of the FETs and the performance of the gate dielectric in different electrolyte solutions is given in chapter 3. The realization of a sodium ion selective system is presented in chapter 4. In Chapter 5, an ISFET-based biosensor (BioFET) for the detection of a pharmacologically relevant protein is demonstrated. Additional experiments for potassium ion sensing are presented in Chapter 6.

---

[1] During the project different sensor designs have been established. Although the FET sizes eventually exceed the nanoscale, the original terminology of silicon nanowire is kept throughout this thesis.

1

Theoretical Background

The basic concept of the nanowire sensor, the Ion-Sensitive Field-Effect Transistor (ISFET) was already introduced in the 1970s. In the last forty years an advanced insight into the field was gained by a large research community[32]. However the practical applications stayed behind. Although ISFETS are used from pH metering up to human genome sequencing[18], so far the basic mechanism of commercial applications does not exceed proton sensing. This chapter gives an introduction to the fundamentals of ISFETs and their theoretical limitations.

1.1 ISFET Theory

The ion-sensitive FET is based on a metal oxide semiconductor FET. Thereby the gate metal is replaced by the solution carrying the analyte species. The electrical potential of the solution affects the output of the ISFET and hence needs to be well controlled. This section explains the basics of an ISFET including the field-effect transistor as transducer element and the interactions at the solid-liquid interface.

1.1.1 The Field-Effect Transistor

A Field-Effect Transistor (FET) is a three terminal semiconductor device. The resistance between the source and the drain contacts is controlled by the voltage applied to the gate contact (transfer resistor). The theoretical principle of such a device was patented in 1925 by Julius E. Lilienfeld. The first working transistor device was presented in 1947 by William B. Schockley,

Walter H. Brattain and John Bardeen at Bell Labs, for which they got the No-
bel price in 1956[33]. Ever since the transistor has become the most important
element in electronics. An enormous development, predicted by Gordon E.
Moore, doubled the transistor density on integrated circuits every two years
over the last decades. Current microprocessors have a density close to 9 mil-
lion transistors per mm^2 [34].

The most commonly used type of transistor is the metal oxide semicon-
ductor field-effect transistor (MOSFET). Here we will present the very basics
of silicon on insulator (SOI) MOSFETs, where the semiconducting channel
is separated from the bulk substrate. For a more detailed description the
reader is refereed to standard literature, e.g.[35–37]. The primary material
used in semiconductor industry is silicon. Intrinsic silicon has a band gap
of 1.12 eV, with the Fermi level in the middle of the bands. At tempera-
tures above absolute zero electrons are excited across the band gap into the
conduction band and form a hole in the valence band, thus the number of
electrons n and holes p is equal. This results in a charge carrier density of
$1.5 \cdot 10^{10}$ cm^{-3} at room temperature[36]. To increase the number of charge
carriers in silicon doping atoms are implanted. The substitution of silicon
atoms with boron ions creates free holes, where phosphorus ions add addi-
tional free electrons. According to the type of doping the Fermi level shifts
towards the valence or conduction band.

The operating mechanism of a low-doped p-type SOI MOSFET is shown
in Fig. 1.1. The semiconducting channel is separated from the metal gate
by an insulating oxide layer. The difference in the work functions of the
semiconductor (Φ_s) and the metal (Φ_m) leads to a band bending in the semi-
conductor. By applying a compensating bias (flatband voltage, V_{fb}) the band
bending can be removed (flat band condition in Fig. 1.1 a).

Depletion   If a positive voltage is applied to the metal with respect to the
semiconductor, the bands bend downwards as shown in Fig. 1.1 b. The
Fermi level in the metal gate is lowered by a certain gate voltage V_g with
respect to the semiconductor, causing the valence band to move away from
the semiconductor Fermi level. As a result the hole density near the interface
falls below the bulk value in the p-type semiconductor and the conductance
decreases.

Hole accumulation   If a negative gate voltage is applied, the nega-
tive charge on the metal accumulates an equal positive charge at the
semiconductor-oxide interface. The bands bend upwards as shown in Fig.

1.1 c. The valence band comes closer to the Fermi level, causing an accumulation of holes at the interface and an increased p-type conductivity.

Fig. 1.1 d and e show the schematic cross section of a low-doped p-type SOI MOSFET with highly p-doped source and drain contacts. The inversion regime is not addressed here, since electron dominated current is suppressed by the p-type contacts (p-n diode). The high doping is needed for low contact resistance.

In addition to the metal gate which is isolated from the semiconductor, we have highly doped ohmic source and drain contacts. If a bias is applied between the source and drain, a current will flow in the channel. This current is determined by the concentration of charge carriers in the channel which is controlled by the gate voltage. The conductance G is given by the channel dimensions (width W, thickness t and length L) and the conductivity σ, which depends on the number of charge carriers p and their mobility μ.

$$G = \sigma \frac{W \cdot t}{L}, \quad \sigma = pe\mu \tag{1.1}$$

With e being the elementary charge. The charge per volume $p \cdot e = (C_{ox}^{\square}/t) \cdot \Delta V_g$ is given by the oxide capacitance per area $C_{ox}^{\square}$, the channel thickness t and the gate voltage V_g. Additionally the difference in workfunction Φ_{ms} between the metal gate and semiconductor as well as fixed charges in the oxide Q_{ox} have to be taken into account. The compensating flatband voltage is calculated as follows.

$$V_{fb} = \Phi_{ms} - \frac{Q_{ox}}{C_{ox}}, \text{ with } \Phi_{ms} = \Phi_m - \Phi_s \tag{1.2}$$

If the transistor is in accumulation, the source-drain current I_{sd} through the channel is described by

$$I_{sd} = \mu C_{ox}^{\square} \frac{W}{L} (V_g - V_{fb}) V_{sd} \tag{1.3}$$

with V_{sd} being the source-drain voltage. This is referred to the linear regime and only holds for $V_{sd} << V_g - V_{fb}$. At higher V_{sd} the channel can pinch off at the source or drain contacts and the current saturates.

However, the process of charge accumulation is not sudden. Below the so-called threshold voltage V_{th} (in accumulation $V_{th} = V_{fb}$) a small source-drain current can flow due to thermal activation of charge carriers. The number of charge carriers N_a is given by the Boltzmann statistics

$$N_a = N_i \cdot e^{\frac{-eV_g}{k_b T}} \tag{1.4}$$
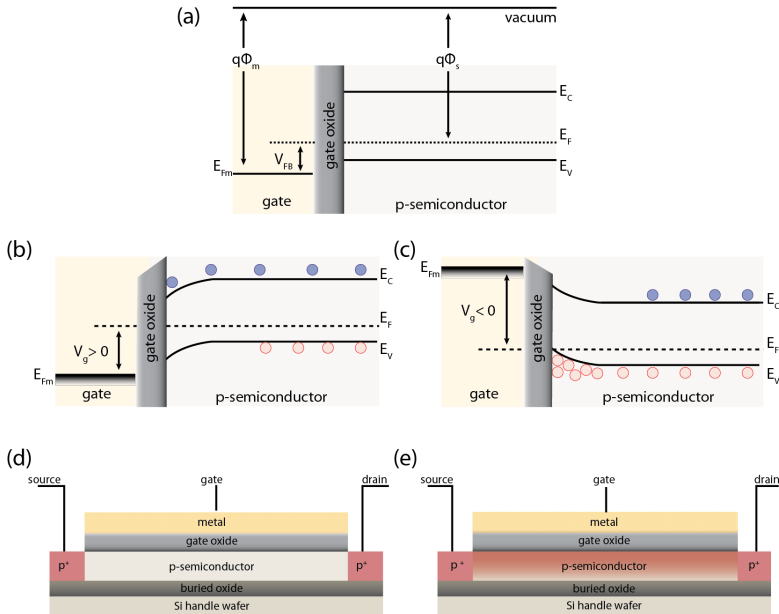
Figure 1.1: MOSFET model: (a) Bandstructure of a low-doped p-type MOSFET in flatband condition. E_F is the Fermi energy of the semiconductor, where E_V and E_C denote the valence and conductance band. $q\Phi_s$ is the workfunction of the semiconductor. E_{Fm} is the metal gate Fermi energy, V_{FB} the flatband voltage and $q\Phi_m$ is the metal workfunction (b) At positive gate voltage V_g the bands bend downwards and the MOSFET is in depletion. (c) If a negative gate voltage is applied, the bands bend upwards and holes accumulate close to the gate oxide. The MOSFET is in accumulation. (d) Sketch of a SOI MOSFET cross section in depletion mode. The buried oxide separates the handle wafer from the p-type channel. Highly doped (p^+) contact regions represent the source and drain contacts. The gate oxide separates the semiconducting channel from the metal gate electrode. (e) At negative V_g the transistor is in accumulation and a current flows.

where N_i is the intrinsic carrier concentration, k_b the Boltzmann constant and T the temperature. Thus the subthreshold current is exponentially dependent on the gate voltage. The exponential function appears as a straight line on a semi-log scale (Fig. 1.2). The reciprocal slope of this line defines the subthreshold swing S

$$S = \frac{\partial V_g}{\partial(log_{10}I_{sd})} = -ln(10)\frac{k_bT}{e} \cdot n \qquad (1.5)$$

The subthreshold slope factor n of a uniformly doped device can be calculated using expressions for the gate oxide and depletion capacitances C_{ox} and C_d, respectively.

$$n = 1 + \frac{C_d}{C_{ox}} \qquad (1.6)$$

Since n is always larger than 1, the minimum swing is limited by temperature and is $-59\,\text{mV/dec}$ at room temperature $(24,5°\text{C})$[38]. A small subthreshold swing is highly desired since it improves the ratio between the on- and off-currents.

Equations 1.3 and 1.6 show that a high C_{ox} is advantageous for a high current variation for a given change in gate voltage.

The theory presented here only holds for normally-off MOSFET devices operated in accumulation or inversion-mode. The physics changes for heavily doped junctionless transistors, where the doping concentration in the channel is identical to that in the source and drain contacts. Such normally-on MOSFETs are interesting for short channel devices due to the lack of junctions and doping concentration gradients[35,39].

1.1.2 Electrolyte Dielectric Interface

Replacing the metal gate with a conductive liquid changes the difference in workfunction Φ_{ms} and thereby affects the threshold voltage. Because the liquid potential is controlled via a gate electrode, additional potential drops between gate electrode and gate dielectric need to be included.

If a reference electrode (which will be described later) is used to control the potential in the liquid, the difference in liquid gate voltage ΔV_{lg} is a direct measure of the change in surface potential $\Delta\Psi_0$. However, for a metal electrode the electrochemical potential of the electrolyte solution has to be considered.
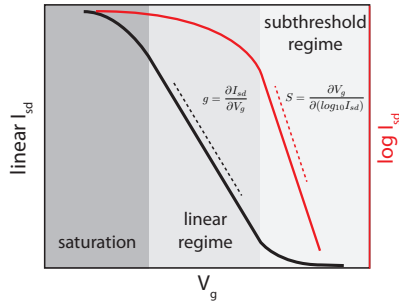
Figure 1.2: Transfer curve for a p-type transistor in accumulation. Source-drain current I_{sd} on a linear and log scale as a function of gate voltage V_g. The dashed line in the subthreshold regime denotes the subthreshold slope. It's reciprocal value is the subthreshold swing S. The dashed line in the linear regime denotes the transconductance g_m. In saturation the resistance of the contacts start to dominate and the current saturates.
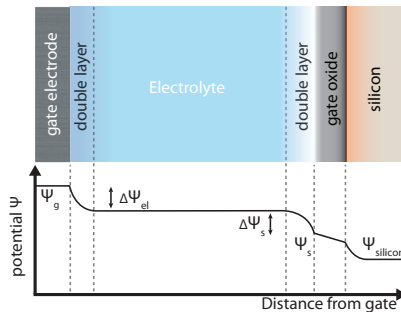
Figure 1.3: Potential distribution in an ISFET. The potential applied to the gate electrode Ψ_g drops over the double layers at the gate electrode and the sensor surface.

Electrochemical Potential   Similar to the Fermi energy E_F in semiconductors, the chemical potential μ_i is a form of potential energy for a certain species i. It can be defined as the slope of the free energy of a system with respect to a change in the number of moles species i.

$$\mu_i = \frac{\partial G}{\partial n_i} \tag{1.7}$$

Temperature, pressure and the amount of other species than i are kept constant. Here G is the Gibbs free energy, given by $U + pV - TS$ (where U is the internal energy, p is the pressure V is the volume, and S is the entropy).

The energy of an ion in a given medium depends not only on chemical forces but also on the electrostatic field. The electrostatic potential energy per mole is given by $z_i F \Psi$, where z_i is the charge of ion i, F the Faraday constant and Ψ is the electrostatic potential of the phase. The electrochemical potential can be written as the sum of chemical and electrostatic potential:

$$\overline{\mu}_i = \mu_i \pm z_i F \Psi \tag{1.8}$$

An interface between two conductors is in equilibrium if the electrochemical potentials in the two phases are the same. Depending on the nature of the two phases (difference in chemical potentials) an electrical potential establishes at equilibrium.

$$\Delta \Psi = -\frac{\Delta \mu_i}{z_i F} \tag{1.9}$$

This potential difference is called the *Galvani potential*[40]. Figure 1.3 shows how the presence of an electrolyte changes the potential distribution. For V_{th} of an ISFET, the contributions from gate electrode to electrolyte ($\Delta \Psi_{el}$) and electrolyte to gate oxide ($\Delta \Psi_s$) need to be considered[41,42]. Equation 1.2 for the flatband voltage needs to be modified accordingly[43]:

$$V_{fb} = \Phi_{el} - \Delta \Psi_{el} - \Delta \Psi_s - \chi^{sol} - \Phi_s - \frac{Q_{ox}}{C_{ox}} \tag{1.10}$$

where Φ_{el} is given by the gate electrode workfunction and χ^{sol} is the surface dipole potential of the solvent, which has a constant value. If a true reference electrode is used, Φ_{el} and $\Delta \Psi_{el}$ are constant and $\Delta \Psi_s$ is the only variable in eq.1.10. As we will see in the following $\Delta \Psi_s$ depends on the surface reactions and is the measurand for analyte binding.

Reference electrode

Reference electrodes are essential components of potentiometric systems. From eq.1.10 and Fig.1.3 we see that the potential drop from reference electrode to electrolyte ($\Delta\Psi_{el}$) must remain defined and stable. The potential of the standard hydrogen electrode (SHE) was defined as origin of the electrochemical potential and is (conventionally) regarded as zero[44]. However, the SHEs are not used as a reference electrode in practice due to their complicated handling (hydrogen gas flow). Reference electrodes of second kind such as Ag/AgCl or Hg/Hg$_2$Cl$_2$ (calomel) electrodes are more convenient to use. Their potential is well defined in relation to the SHE and stable for a large range of electrolytes. The main components of a reference electrode are the metal electrode, reference solution and a junction that provides electrical connection between the electrolyte and reference solution. For the Ag/AgCl reference electrode a AgCl coated silver wire is immersed in a saturated KCl reference solution. The reactions in the reference cell are given by

$$
\begin{aligned}
Ag^+ + e^- &\rightleftharpoons Ag(s) \\
AgCl(s) &\rightleftharpoons Ag^+ + Cl^-
\end{aligned}
\tag{1.11}
$$

where (s) denotes solid. The overall reaction can be written as:

$$
AgCl(s) + e^- \rightleftharpoons Ag(s) + Cl^-
\tag{1.12}
$$
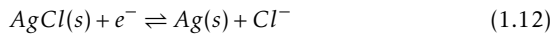
This reaction works at very high efficiency due to fast electrode kinetics, meaning a sufficiently high current can be passed through the electrode. The potential drop $\Delta\Psi_{el}$ between the metal and reference solution is given by the Boltzmann distribution.

$$
a_{Cl(s)} = a_{Cl^-} \exp\left(-\frac{e\Delta\Psi_{el}}{k_b T}\right)
\tag{1.13}
$$

$$
\text{with } a_{Cl(s)} = \text{constant: } \Delta\Psi_{el} = \frac{2.3 k_b T}{e} log_{10}(a_{Cl^-})
\tag{1.14}
$$

Thus the electrode potential only depends on the activity of Cl$^-$ ions in the reference solution. Usually a saturated KCl solution is used to keep the concentration of Cl$^-$ and hence the potential drop constant. The need for the reference solution is the substantial drawback of reference electrodes. It makes them fragile and hard to miniaturize. Although many attempts have been made to scale down or develop solid state reference electrodes[44–46], its implementation remains one of the large drawbacks of micro- and nanoscale ISFET sensors.

Electric Double Layer at Interfaces   When a surface is in contact with an electrolyte, an electric double layer (EDL) with a characteristic potential distribution is formed at the interphase. Charges at the surface attract counter ions in the solution. Due to their finite size, a single layer of ions cannot sufficiently screen the surface charges. Hence a diffuse layer of counter-ions near the surface screens the exceeding charges, which leads to a certain potential profile. The Gouy-Chapman-Stern model is most commonly used to describe the potential and charge distribution in EDLs[43]. It describes the EDL as a series of layers as shown in Fig. 1.4. Due to the size of the ions and the solvent molecules of the solvation shell, an electrically neutral layer called Stern or Helmholtz layer is located closest to the surface. The outer Helmholtz plane (OHP) is defined at the center of the counter ions, where the diffuse layer (Gouy-Chapman layer) starts. The charge in the diffuse layer is:

$$\sigma_{dif} = -\sqrt{8k_b T \epsilon \epsilon_0 c} \cdot \sinh\left(\frac{e\Psi_{OHP}}{2k_b T}\right) = -C_{dl}\Psi_0 = -\sigma_0 \qquad (1.15)$$

where ϵ denotes the relative permittivity and ϵ_0 is the permittivity of vacuum. Due to charge neutrality, it is equal to the surface charge σ_0. Here Ψ_{OHP} is the charge at the outer Helmholtz plane, c is the ion concentration in the electrolyte, Ψ_0 is the surface potential drop ($=\Delta\Psi_s$) and C_{dl} is the double layer capacitance. $C_{dl} = C_{St}C_{dif}/(C_{St} + C_{dif})$ consists out of a series of capacitances, the constant Stern layer capacitance ($C_{St} = 0.2\,\mathrm{F/m^2}$) and the diffuse capacitance C_{dif}. C_{dif} is mainly determined by the ionic strength of the electrolyte, since the characteristic length of the diffuse layer, is given by the Debye length[47]:

$$\lambda_D = \sqrt{\frac{\epsilon\epsilon_0 k_b T}{2N_A e^2 I_c}}, \text{ with } I_c = \frac{1}{2}\sum c_i z_i^2 \qquad (1.16)$$

where N_A is the Avogadro constant, I_c the ionic strength, c_i the ion concentration in mole per liter and z_i the charge number of the ion. Fig. 1.4 c shows the calculated Debye length and C_{dl} at different electrolyte concentrations.

1.1.3 pH Sensing

pH sensing is the most important application for ISFETs. The gate oxide surfaces are intrinsically sensitive to protons. They display surface hydroxyl groups at a very high density. In contact with aqueous solutions the hydroxyl groups undergo protonation and deprotonation and thereby building up a
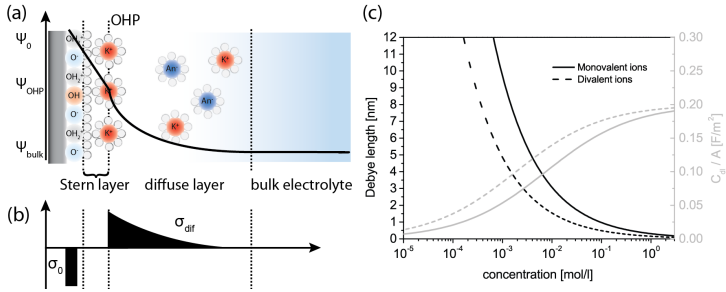
Figure 1.4: (a) Scheme of the electric double layer at the gate oxide surface according to the Gouy-Chapman-Stern model. Here the surface is slightly negative charged. cations (K^+) surrounded by a solvation shell of water molecules are attracted to the surface (Stern layer). At the outer Helmholtz plane (OHP) the diffuse layer starts and extends to the Debye length. The black line indicates the potential distribution at the interface. (b) Charge distribution at the oxide/electrolyte interface (adapted from ref. [43]). (c) Calculated Debye length (black lines) and double layer capacitance per area (C_{dl}/A, grey lines) *vs.* electrolyte concentration. C_{dl}/A is calculated as a series of Stern capacitance ($C_{st} = 0.2\,F/m^2$) and diffuse capacitance (C_{dif}).[48,49]

surface charge σ_s. The site-binding model derived by Bousse, de Rooij and Bergveld[48] provides a relationship between the surface potential Ψ_0 and the pH value of the bulk solution.
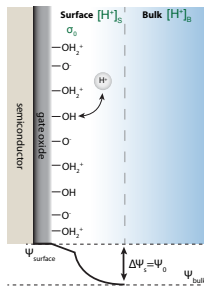
Figure 1.5: Scheme of surface protonation and deprotonation. The surface pH is buffered by the surface hydroxyl groups. Hence, a change in bulk pH changes the surface charge which leads to a potential gradient at the interphase.

The surface reactions at the amphoteric OH surface groups of a metal (Me) can be expressed by the equilibrium constants for deprotonation K_a and protonation K_b:

$$MeOH \rightleftharpoons MeO^- + H_s^+, K_a = \frac{\nu_{MeO^-} \cdot a_{H_s^+}}{\nu_{MeOH}} \tag{1.17}$$

$$MeOH_2^+ \rightleftharpoons MeOH + H_s^+, K_b = \frac{\nu_{MeOH} \cdot a_{H_s^+}}{\nu_{MeOH_2^+}} \tag{1.18}$$
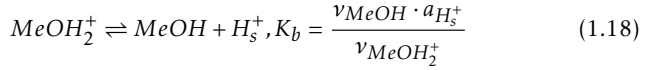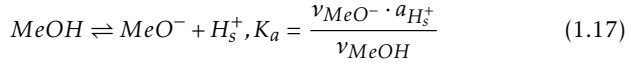
with ν being the number of sites of a particular species and $a_{H_s^+}$ the activity of the surface protons. The surface can either be neutral (MeOH), positively charged ($MeOH_2^+$), or negatively charged (MeO^-).

The total number of these surface sites is

$$N_s = \nu_{MeOH} + \nu_{MeO^-} + \nu_{MeOH_2^+} \tag{1.19}$$

The total surface charge is generated by the protonated and deprotonated sites

$$\sigma_0 = e\left(\nu_{MeOH_2^+} - \nu_{MeO^-}\right) \tag{1.20}$$

At the point of zero charge (PZC) $\sigma_0 = 0$. This situation occurs if $pH = (pK_a + pK_b)/2$. Equation 1.20 can be rewritten using eq. 1.17 and 1.18:

$$\sigma_0 = eN_s \left(\frac{a_{H_s}^2 - K_a K_b}{a_{H_s}^2 + a_{H_s} K_b + K_a K_b}\right) \tag{1.21}$$

As we have seen in fig.1.4 the surface charge σ_0 is screened by the ions in the double layer. The surface potential Ψ_0 is given by the double layer capacitance C_{dl}

$$\sigma_0 = C_{dl}\Psi_0 \tag{1.22}$$

The relationship of surface proton activity ($a_{H_s^+}$) with bulk proton activity (a_{H_b}) can be described by the Boltzmann distribution:

$$a_{H_s^+} = a_{H_b^+} \exp\left(-\frac{e\Psi_0}{k_b T}\right) \text{ or } pH_s = pH_b + \frac{e\Psi_0}{2.3 k_b T} \tag{1.23}$$

with $pH = -log_{10}(a_{H^+})$ and pH_s being surface pH and pH_b being bulk pH. Maximum pH response is given if the surface is able to keep pH_s constant. This is the so called Nernst limit of $\Delta\Psi_0/\Delta pH_b = 59\,\text{mV/pH}$ at room temperature. However, this is only possible if an unlimited number of hydroxyl groups can be protonated or deprotonated. In a real system $\Delta\Psi_0/\Delta pH_b$ strongly depends on N_s, K_a and K_b as we will see in the following

Discussion of the site-binding model   Equations 1.17 to 1.23 can be used to provide the relation between Ψ_0, σ_0 and $a_{H_b^+}$ [48,50]

$$a_{H_b^+} = \sqrt{K_a K_b} \exp\left(\frac{e\Psi_0}{kT}\right) \times \tag{1.24}$$

$$\frac{\frac{e\Psi_0}{kT}\frac{C_{dl}}{C_s}\frac{1}{2}\sqrt{\frac{K_b}{K_a}} + \sqrt{1 + \left(\frac{e\Psi_0}{kT}\frac{C_{dl}}{C_s}\frac{1}{2}\sqrt{\frac{K_b}{K_a}}\right)^2 \left(1 - \left(2\sqrt{\frac{K_a}{K_b}}\right)^2\right)}}{1 - \frac{e\Psi_0}{kT}\frac{C_{dl}}{C_s}}$$

where the surface buffer capacitance C_s is related to the number of sites N_s via

$$C_s = \frac{e^2 N_s}{2.3 k_b T} \tag{1.25}$$

In Fig. 1.6 the surface potential Ψ_0 is plotted against the pH of the bulk solution according to eq. 1.24. Here the point of zero charge PZC= $(pK_a + pK_b)/2$ is set to $pH = 7$. The double layer capacitance C_{dl} at a constant ionic strength of $100\,\text{mM}$ is taken as a series connection of the Stern layer capacitance C_{st} and the diffusive layer capacitance C_{dif}. Thus $C_{dl} = C_{dif}C_{st}/(C_{dif} + C_{st}) \approx 0.16\,\text{F/m}^2$, if $C_{st} = 0.2\,\text{F/m}^2$ [4,48,49] and $C_{dif} = 0.7\,\text{F/m}^2$ is taken by assuming a simple parallel plate capacitor. The pH has only a small effect on C_{dl} and is neglected in the following [4,51]. The number of reactive sites per unit area N_s has a significant influence on the pH response ($\frac{\Delta\Psi_0}{\Delta pH}$). In Fig. 1.6 a pK_a and pK_b are set equally. For a large number of surface sites ($N_s > 10^{14}\,\text{cm}^{-2}$), which is the case for many oxides, the surface potential decreases linearly with increasing bulk pH. These pH responses ($58.8\,\text{mV/pH}$ for $10^{15}\,\text{cm}^{-2}$ and $56.9\,\text{mV/pH}$ for $10^{14}\,\text{cm}^{-2}$) are very close to the Nernst limit. Reducing N_s results in a S-shaped curve ($10^{13}\,\text{cm}^{-2}$) with the steepest slope around the PZC. At even lower surface group density ($N_s = 10^{12}\,\text{cm}^{-2}$) the curve is almost flat and pH response vanishes. Hence, a reduction of N_s by at least three orders of magnitude is needed to suppress the pH response of a highly proton sensitive surface such as Al_2O_3 and HfO_2.

To emphasizes the dependence of Ψ_0 on N_s vertical cuts along a constant pH value (dashed line) are plotted in the inset. No potential shift due to a change in pH is seen for $N_s < 10^{12}\,\text{cm}^2$. At higher N_s the pH response increases and saturates at the Nernst limit.
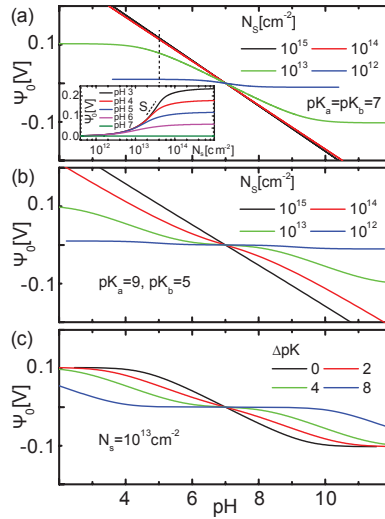
Figure 1.6: Theoretical curves of the surface potential Ψ_0 as a function of pH according to the site-binding model. pK_a and pK_b are chosen such that the PCZ is at pH 7. In (a) both pK_a and pK_b are set to 7 and the density of surface hydroxyl groups N_s is changed. The inset shows Ψ_0 $vs.$ N_s at different pH values. In (b) ΔpK is set to 4. (c) shows the influence of ΔpK at constant and intermediate N_s.

Figure 1.6 b shows the pH response for a larger $\Delta pK = 4$. Assuming that protonation is more likely to happen as deprotonation, we set pK_a larger than pK_b ($K_a < K_b$). The full Nernstian slope cannot be reached any more and becomes non-linear already at $N_s = 10^{14}\,\mathrm{cm}^{-2}$. At the same time the shape of the curve has changed. Around the PCZ the curve is flat and has the steepest slope around the pK values. The transition from sigmoid (Fig. 1.6 a) to double-sigmoid (Fig. 1.6 b) is pointed out in Fig. 1.6 c. To get a clearly non-linear behaviour N_s is kept constant at $10^{13}\,\mathrm{cm}^{-2}$ while ΔpK is changed. With increasing ΔpK the shape changes from sigmoid to double-sigmoid. At the same time saturation occurs at more extreme pH values.

From equation 1.24 we see that the transition from a linear to a sigmoid shaped pH response is given by the capacitance ratio of C_{dl}/C_s. At high ionic strength ($> 100\,\mathrm{mM}$) C_{dl} is assumed to be constant. Therefore the ratio strongly depends on the density of active surface groups N_s. Bare oxides like Al_2O_3 or HfO_2 have a high density of surface hydroxyl groups, hence $C_s >> C_{dl}$. The high number of OH groups buffer changes in the bulk pH by taking up or releasing protons, resulting in a high pH response.

1.2 Sensitivity and Limitations

Terms like sensitivity, selectivity, response, resolution, measurement range and limit of detection (LOD) are used to characterize a sensor. However the definition of those terms is not always clear. In this section we describe these figures of merit according to their further use in this work.

The input of the sensor is e.g. a change in analyte concentration. The consequent change in surface potential $\Delta\Psi_0$ is described by the ***response***, given by $\Delta\Psi_0/\Delta log[c]$ (where c is the analyte concentration). The ***resolution*** of $\Delta\Psi_{0,\min}$ is limited by the gate referred voltage noise S_{VG}, described in 1.2.1. The ***signal to noise ratio (SNR)*** is the change in surface potential, given by a certain input, divided by the random fluctuations of the surface potential $\mathrm{SNR} = \Delta\Psi_0/\Delta\Psi_{0,\min}$. The ***sensitivity*** is the detectable relative change in concentration $\Delta c/c$ and is directly related to the SNR. The ***limit of detection (LOD)*** is the minimum detectable change in concentration Δc at a certain concentration.

1.2.1 Noise in ISFETs

The quality of a signal is given by the signal to noise ratio. Noise is referred to as random and uncorrelated fluctuations of the signal over time. It is observed in all conductive materials and is especially important in electronic

sensors, as it determines the resolution of the signal. The noise spectral density S is the noise power per unit of bandwidth; that is, the power spectral density of the noise. It's dimension is power/frequency. In general the origin of the noise can be external e.g. from power lines or internal. Since external noise can be removed we will focus on the internal noise present in ISFET sensors. Different types of independent noise sources are known[52].

Thermal Noise   also called Johnson-Nyquist noise is caused by thermodynamic fluctuations of charge carriers. Resistive materials generate thermal noise independent of the applied bias. The power spectral density of the voltage fluctuations due to thermal noise is given by the resistance R and the temperature:

$$S_{JN} = 4k_b T R \tag{1.26}$$

Thermal noise is frequency independent (also called white noise) and given in units of V^2/Hz.

Shot Noise   Shot noise in electronic circuits consists of random fluctuations of the electric (DC) current which originate due to fact that current actually consists of a flow of discrete charges. It is temperature and frequency independent. It's power spectral density is given by $S_I = 2eI$ and is given in units of A^2/Hz. However for most electronic systems operated at room temperature the contribution of shot noise to the total noise is insignificant and is therefore neglected in this work.

1/f Noise   also called pink noise is present in all semiconductors, metals and superconductors under bias. It is a resistance fluctuation, which is transformed to voltage or current fluctuations via Ohm's law. The noise power spectrum is proportional to $1/f$. It is the dominant noise source in transistors operated at low frequencies.

The origin on $1/f$ noise in MOSFETs and thus in ISFETs is still under discussion. The current is sensitive to charge traps present at the gate interface in the form of contaminants, dangling bonds or vacancies. Number fluctuation of these traps is generally believed to be the dominant $1/f$ noise mechanism. In reference[53] we investigated the dominant $1/f$ noise source in our silicon nanowire sensors. Comparing different transistor dimensions and gate oxide capacitances supports the trap state noise model in which the source of $1/f$ noise is due to trap states residing in the gate oxide (most likely in the interface between the semiconductor and the oxide). Hence we will

focus on this model in the following. In the trap State Noise Model the trapping and detrapping of charge carriers into trap states at the semiconductor-oxide interface cause $1/f$ noise. Hence the interface quality determines the noise. The charge fluctuations in the gate oxide are given by a power spectral density $S_{Q_{ox}}$:

$$S_{Q_{ox}} = e^2 N_{ot} WL \frac{1}{f} \tag{1.27}$$

where N_{ot} is the trap state density per area, W and L denote width and length and f the frequency. The gate referred voltage noise is then given by:

$$S_{VG} = \frac{S_{Q_{ox}}}{C_{ox}^2} = \frac{e^2 N_{ot}}{WLC_{ox}^{\square 2}} \frac{1}{f} \tag{1.28}$$

where $C_{ox}/WL = C_{ox}^{\square}$ is the gate oxide capacitance per area. S_{VG} is given in units of V^2/Hz and represents the theoretical noise which would have to be applied to the gate voltage to obtain the same drain current noise in the transistor [54]. S_{VG} directly defines the resolution of the surface potential and thus limits the sensitivity. To reduce S_{VG} the quality of the semiconductor-oxide interface needs to be improved to achieve a lower N_{ot} and $C_{ox}^{\square}$ needs to be increased.

Signal to Noise Ratio

If a certain amount of charge Q at the sensor surface is taken as a signal, the noise from fluctuating charges in the semiconductor-oxide interface δQ will be given by $\sqrt{S_{Q_{ox}}}$. The total charge Q is proportional to the sensor area (WL). From eq.1.28 follows that $\delta Q \propto \sqrt{WL}$. Hence the signal to noise ratio is better for a larger sensor surface according to:

$$\text{SNR:} \frac{Q}{\delta Q} \propto \frac{WL}{\sqrt{WL}} \propto \sqrt{WL} \tag{1.29}$$

1.2.2 Dynamic Range Sensing

According to Eq. 1.24 the surface potential changes linearly upon an exponential change in analyte concentration. However, this is only valid in a certain concentration range which is given by the density of reactive surface groups and their reaction constants (as shown in Fig. 1.6). Outside this range the response weakens and eventually saturates. To exemplify the dependency on concentration we generated a model sensor response. Fig. 1.7 a shows a model of an ISFET which is sensitive to a negatively charged

analyte at a given concentration c. Increasing the analyte concentration in the bulk solution changes the surface potential. Taking the derivative reveals the response $\Delta\Psi_0/\Delta log[c]$ as a function of the concentration (Fig. 1.7 b). The strongest response is in the concentration range between 1 mM and 1 M. Since the intrinsic noise of the system is independent of the analyte concentration [53] the resolution $\Delta\Psi_{0,\min}$ is always the same. However, the minimum detectable Δc strongly depends on the analyte concentration. Fig. 1.7 c shows the LOD for our model system, using the gate referred noise of $\sqrt{S_{VG}}$ of $1 \cdot 10^{-5}$ V/Hz$^{1/2}$ from [53] as $\Delta\Psi_{0,\min}$, calculated according to:

$$\text{LOD: } \Delta c = \frac{\Delta\Psi_{0,min}}{\text{response}(c)} \cdot c \qquad (1.30)$$

The lower the concentration, the better the LOD. Here a minimum in Δc of $0.6\,\mu$M is achieved around 1 mM analyte concentration. At even lower concentrations the LOD increases again due to the decrease in response.

ISFETs are only able to measure relative changes in analyte concentrations. However using calibration or differential sensing the sensor can be tuned to measure absolute concentrations. Estimating the LOD for protons for a pH sensitive ISFET exemplarily reveals the dynamic nature of the sensor. As an example for an oxide surface showing a response of 50 mV/pH in the range of pH 3-10, the LOD changes from $0.2\,\mu$M at pH 3 to 20 fM at pH 10.

1.2.3 Detection of Large Molecules

The potential of ISFETs to sense adsorbed molecules has increased the motivation for building a BioFET for protein sensing. Proteins are composed of a linear sequence of amino acids. Their size is usually given by their weight and ranges from a few kDa to a few hundred kDa. Hence, their radius quickly exceeds a few nm. The pH level of the electrolyte solution determines the total net charge of the protein. Each protein has a characteristic pH at which the protein has no net charge, the isoelectric point (pI). Below this value the protein is positively charged. At higher pH the protein carries a negative charge. By specifically adsorbing the protein to the sensor surface, the change in $\Delta\sigma_0$ can be detected by the ISFET. However, in electrolytes charges are screened due to the presence of solvent molecules and counter ions (see section 1.1.2). At the sensor surface the characteristic distance at which the external electrical potential decays by $1/e$ is given by the Debye length (Eq. 1.16). Linker molecules such as antibodies or glycoconjugates are used to adsorb proteins specifically. The length of the linker molecules on the surface plus the protein size can easily exceed 5 nm.
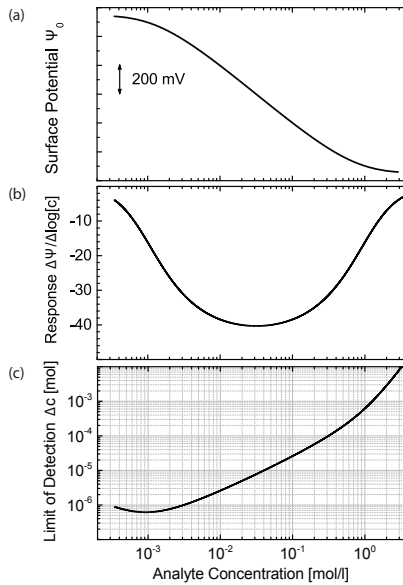
Figure 1.7: Model for dynamic range sensitivity. (a) Surface potential Ψ_0 plotted against the log of concentration of the analyte. (b) The derivative of the surface potential shows the response to the analyte. (c) LOD: Δc as a function of c. Small changes are only detectable at a low analyte background concentration.

Fig. 1.4 b in the previous section 1.1.2 shows the Debye length as a function of electrolyte concentration. Charges which are located further away from the surface are screened by counter ions and hence do not influence the surface potential. Hence, direct protein sensing is highly limited at physiological conditions ($\approx 150\,$mM electrolyte concentration) where the Debye length is already < 1 nm.

To minimize the screening effect, the ionic strength of the solution can be reduced. In a work by Vacic *et al.*[55] Debye screening manipulation is used for quantitative spatial analysis of adsorbed charge on a nanosensor surface. DNA and Streptavidin detection in diluted buffers has been shown by X. Duan *et al.*[16]. G. Zheng *et al.* showed detection of cancer markers with Silicon nanowires (SiNWs) even in undiluted serum[12].

If the size of an analyte such as a protein is comparable to the Debye lentgh, the surface analyte activity becomes equal to the bulk analyte activity. Hence, the relationship is no longer described by the Boltzmann distribution as it is given for protons in Eq. 1.23. The surface potential is then given by the total charge of the adsorbed analyte inside the double layer, the capacitance and the reaction kinetics. This will be further described in section 5.2.

Due to Debye screening direct potentiometric sensing of protein charges is difficult and only works as long as charged parts of the protein fit into the double layer at the electrolyte-insulator interface. However, since the two double layers (from surface and protein) overlap, the ISFET response upon protein binding is difficult to describe. As we have seen from Eq. 1.23 the pH near a charged interface (pH_s) depends on the potential drop over the double layer and can be different from the bulk pH. Due to this change, the protein net charge can be changed accordingly. Hence the final signal is linked to the effects of ionic strength, bulk pH, protein pI and effective distance of the protein layer from the surface, etc. In references[47,56] Bergveld and Schasfoort *et al.* analysed the limitations of direct protein detection by calculating the measurable potential as a function of electrolyte concentration based on the Donnan equilibrium. It describes the ion distribution across a semi-permeable membrane given by the adsorbed protein layer.

1.2.4 Effect of Competing Surface Reactions on ISFET Response

Full selectivity is given if a sensor only responds to one specific type of analyte. However, full selectivity is most likely not possible, since competing and nonspecific reactions cannot be suppressed completely. Dielectric surfaces are proton sensitive by the majority. By surface functional-

ization the proton sensitivity does not vanish completely. Further, linker molecules such as ion traps or antibodies show some cross-reactivity with species which are similar to their targeted analyte. As long as an ISFET is not fully selective for a certain analyte, the response to background species limits the performance of the sensor[57].

In a simple model we demonstrate how the response of a functionalized ISFET which is specific to a certain analyte is influenced by its proton sensitivity. In analogy to the site-binding model explained in section 1.1.3 the model assumes the protonation and deprotonation of surface hydroxyl groups and an additional reaction between the immobilized linker molecule $L()$ and the negatively charged analyte A^-.

$$
\begin{aligned}
MeOH &\rightleftharpoons MeO^- + H_s^+, K_a \\
MeOH_2^+ &\rightleftharpoons MeOH + H_s^+, K_b \\
MeL(A^-) &\rightleftharpoons MeL() + A^-, K_c
\end{aligned}
\tag{1.31}
$$
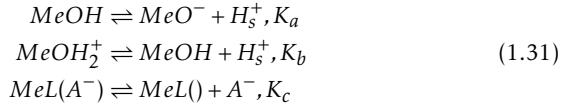
K_a, K_b, K_c are the dissociation constants which are fixed and given by the surface linker properties. The number of proton sensitive surface hydroxyl groups N_s and linker groups N_L is defined as follows:

$$
\begin{aligned}
N_s &= \nu_{MeOH} + \nu_{MeO^-} + \nu_{MeOH_2^+} \\
N_L &= \nu_{MeL()} + \nu_{MeL(A^-)}
\end{aligned}
\tag{1.32}
$$

with ν being the number of the particular species. Hence, the surface charge of the sensor is given by

$$
\sigma_0 = e\left(\nu_{MeOH_2^+} - \nu_{MeO^-} - \nu_{MeL(A^-)}\right) = C_{dl}\Psi_0.
\tag{1.33}
$$

The relations of bulk and surface activities of protons and analyte are given by the Boltzmann distribution: $a_{H_s^+} = a_{H_b^+}\exp(-e\Psi_0/k_bT)$ for protons and $a_{A_s^-} = a_{A_b^-}\exp(e\Psi_0/k_bT)$ for the analyte species. In this approach the reactions including protons are independent of the reactions including the analyte. The coupling is only given by the surface potential Ψ_0. In analogy to Eq. 1.24 the system can be solved for $\Psi_0(a_{H^+}, a_{A^-})$. For a surface which shows a Nernstian response to pH, Ψ_0 is not affected by analyte binding. Charges from the analytes are fully compensated by exchange of protons. However, if the proton sensitivity is strongly reduced changes in Ψ_0 upon analyte binding start to be visible at certain concentration ranges.

To illustrate this interference effect, we assume the following model system. A gold surface (which is slightly oxidized, according to[58]) with $N_s =$

$1.5 \cdot 10^{17}\,\mathrm{m}^{-2}$ and $K_a = K_b = 10^{-7}$ is functionalized with a specific linker molecule. The corresponding analyte is a small negative charged species with dissociation constant $K_D = 10^{-9}\,\mathrm{M}$. We assume the maximum occupancy to be one charge per $10\,\mathrm{nm}^{-2}$, resulting in a $N_L = 1 \cdot 10^{17}\,\mathrm{m}^{-2}$, which is reasonable considering the dimensions of proteins. Fig.1.8 shows the calculated surface potential plotted against analyte and proton concentration. It shows that the concentration range in which the sensor is sensitive to the analyte is limited by the electrolyte pH. As pH increases the surface becomes more sensitive to protons and the range of large response is shifted to higher analyte concentration. Close to the PZC (here at pH 7) the change in surface potential due to the analytes becomes smaller. The largest response at lowest concentration range (best LOD) is seen if the buffer pH is far below the PZC. In real systems, the pH range is limited because certain analytes, such as proteins denature if the pH is far off compared to their natural environment of operation. Fig. 1.8 b shows that also the pH response changes for different analyte concentrations. Its concentration influence is strongest at extreme pH values and weak around the PZC.
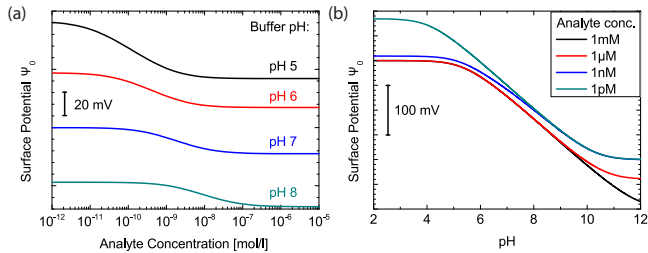
Figure 1.8: Model to demonstrate the influence of protons on analyte sensing. The full site-binding model from [51,58] ($K_a = K_b = 10^{-7}$, $N_s = 1.5 \cdot 10^{17}$) is extended with the analyte dissociation constant $K_D = 10^{-9}\,\mathrm{M}$ and a ligand density of $N_L = 1 \cdot 10^{17}\,\mathrm{m}^{-2}$. (a) Theoretical curves of the surface potential Ψ_0 *vs.* analyte concentration at different buffer pH. (b) Ψ_0 *vs.* pH for different analyte concentrations.

This model illustrates that direct detection of adsorbed analytes is highly limited by interfering proton sensitivity. Surfaces with low pH sensitivity and PZC far away from the analyte buffer pH are then preferable to optimize analyte detection.

1.2.5 Nanoscale ISFETs

By reducing the sensor size people achieved to reduce the sample volumes down to the microliter range. Recently, specific detection of proteins at very low concentration (down to femtomolar) has been reported [2,13,16,59]. Many researchers focus on the point that miniaturizing a sensor increases its charge sensitivity and its surface-to-volume ratio which could lead to lower detection limits. The shift in surface potential for a given change in surface charge is larger for small areas, according to $\Delta\Psi_0 = \Delta\sigma_0/C_{dl}$ where the capacitance scales with the sensor area. However, although the charge sensitivity is increased for smaller structures, the SNR decreases according to Eq. 1.29 since both, charge and C_{dl} depend on the area.

Analyte binding is a uniform process which is determined by reaction kinetics. Where surface properties (*e.g.* density of reactive surface sites) and electrolyte composition play a role, the underlying transducing FET has no influence on analyte adsorption. Hence, the resulting sensor response ($\Delta\Psi_0/\Delta log[c]$) should not depend on the ISFET size. Regarding the LOD, only the SNR needs to be maximized.

A further important consequence of a reduced sensor surface is the predominance of reaction kinetics at very low concentrations. In a study by *Sheehan et al.* [59] the accumulation times for single stranded DNA molecules on micro- and nanoscale objects are calculated. Even if a very low number of analyte molecules (≈ 10) is needed for a reliable detection, the time for their accumulation on nanoscale surfaces quickly exceeds reasonable measurement periods (*i.e.* days) at femtomolar concentration. Even if long measurement times are acceptable, the stability can become an issue. Effects like drift, nonspecific adsorption or desorption of previously adsorbed molecules will limit a reliable detection.

Nevertheless, this limitation inherent to small sensors could be overcome by large scale integration of many sensors into a closely packed array. At the same time this could allow spatially resolved analyte detection. A way to overcome the limits of diffusion time scale is to actively direct molecules to a sensor surface. At which the lab-on-a-chip [60,61] is a promising approach for the necessary speed-up.

<div style="text-align: right">

2

</div>

Experimental Methods

2.1 Device Fabrication

Different fabrication techniques for SiNW sensors have been published in literature. Generally they can be divided into two basic approaches: The *bottom-up* approach[2,31], where nanowires are grown in a chemical vapour deposition process and the *top-down* approach, where the structures are lithographically defined and etched out of bulk material[13,62,63]. The latter allows precise control over the dimensions and layout and enables the possibility for high density integration and up-scaling.

During my PhD two different processes were used for the fabrication of SiNW sensors. Both approaches are based on a top-down process on silicon on insulator wafers. First a UV-lithography based process flow was developed at the Nanoelectronics Lab at the *University of Basel*. This process is described in detail in the PhD thesis by O. Knopfmacher[64]. Later this process was adapted and modified into an electron beam lithography based sample fabrication at the *Paul Scherrer Institut* (*PSI*, *Villigen*) by K. Bedner[65]. This section presents a summary of the process flow of the device fabrication. Further details are given in appendix A.

2.1.1 Sensor Design

The sensor layout, as shown in Fig. 2.1, contains 48 nanowires and their corresponding contacts. They are divided in four spatially separated arrays with a common drain contact referred as "bus line". Each array is separated in four pixels of three nanowires. This design allows multiple surface func-

tionalizations for differential measurements and time-resolved correlation experiments.

To study the influence of the nanowire dimensions on the signal and noise performance we used different nanowire widths on the same chip. Eight different widths are implemented, ranging from $100\,nm$ up to $1\,\mu m$.

In the next chapter we will see that the wider the wires (larger surface area), the better the performance regarding the signal to noise ratio. Therefore, the latest design contained only wide SiNWs of $1\,\mu m$ and nanoribbons of $25\,\mu m$ width. Nevertheless, for simplicity we keep the term nanowire throughout this thesis. Also at least one dimension remains in the nanoscale.
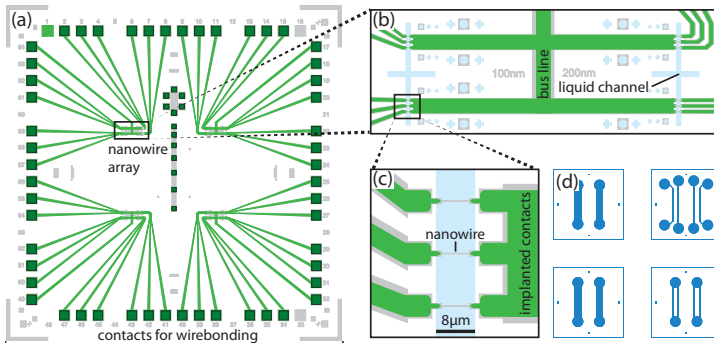
Figure 2.1: (a) Sensor device layout. 48 individually addressable nanowires, arranged in four spatially separated arrays. Each array has a common bus line. The nanowires are $6\,\mu m$ in length. The width varies from $100\,nm$ up to $1\,\mu m$. Grey is the lithography design for the silicon, bright green for the ion implantation and dark green for contact metallization. (b) Close up of the top left array with $100\,nm$ and $200\,nm$ wide wires. The bright blue is the design for the SU-8 opening which defines the liquid channel. (c) Close up of an individual pixel with three SiNWs. (d) Layout for different PDMS microchannel molds. The round structures denote the in- and outlets. A maximum of four individual channels was used for differential functionalization of the SiNWs.

2.1.2 Fabrication Process

Silicon On Insulator (SOI) wafers (*Soitec*, France[66]) with a SiO_2 buried oxide (BOX) layer of $145\,nm$ in thickness were used. The $85\,nm$ thick p-Si(100) device layer with a resistivity of $8.5-11.5\,\Omega cm$ was oxidized thermally until a $15\,nm$ thick SiO_2 layer was grown. The nanowire pattern from Fig. 2.1 was defined in *AZ nLOF* 2000[67] resist by electron beam lithography (EBL).

The nanowires were then carved out by reactive ion etching of SiO_2 in a CHF_3 plasma and anisotropic wet etching of the Si device layer with tetramethylammonium hydroxide (TMAH and isopropyl alcohol 9:1 volume ratio at 45°C). This process etches the Si(111) crystallographic planes about 100 times slower than other planes, resulting in a trapezoidal shape of the nanowire cross-section with 54.7° tilted Si(111) side faces (see Fig. 2.3 d). The resulting NW were $6\,\mu m$ long, 80 nm high, and 100 nm - $1\,\mu m$ wide.
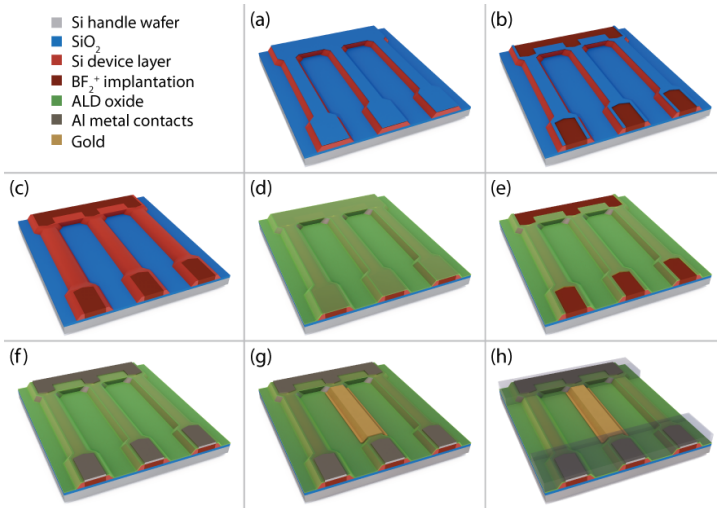
The source and drain contact areas were defined in poly(methyl methacrylat) PMMA resist by EBL and heavily doped by BF_2^+ ions (energy = 33 keV, dose $2.3 \cdot 10^{15}\,cm^{-2}$). The dopants were activated by thermal annealing in a forming gas (6 min at 950°C).

Gate Dielectric The top oxide layer was removed in buffered HF. RCA standard cleaning procedure[68] was used for cleaning the samples from organic and metallic contaminants prior to the gate oxide deposition. After the cleaning a native oxide layer ($\approx 1\,nm$ SiO_2 is formed. On top of this layer 20 nm of either Al_2O_3 or HfO_2, materials with high dielectric constants, were deposited by Atomic Layer Deposition (ALD) at 225°C (*Savannah S100*, *Cambridge NanoTech*[69]). The high quality of the ALD oxide ensures a high gate oxide capacitance C_{ox}, low hysteresis and low leakage currents in the liquid. In addition, it exhibits a high density of surface hydroxyl groups ensuring a good response to pH[3,70]. ALD layers are conformal coatings of very high quality due to the sequential layer-by-layer deposition. The thickness is well controlled by the number of deposition cycles.

For certain experiments gold-coated SiNWs were used. For this purpose a 5 nm thick film of chromium (adhesion layer) and a 20 nm thick gold film was deposited onto the ALD oxide by e-beam evaporation. The film overlapped the SiNWs by 200 nm on each side.

Ohmic Contacts The ohmic contacts were metallized by Al-Si (1%) and annealed at 450°C after local etching of the ALD oxide. A $2\,\mu m$ thick protection layer (SU-8 2002 *MicroChem*) with $6\,\mu m$ wide openings (aligned to the NWs), which is defined by UV lithography, was used as liquid protection. To operate the samples in liquid, they were wire bonded into a chip carrier. The bonds were sealed with epoxy (*Epotek 353ND*[71]).

Fig. 2.2 shows an overview of the fabrication steps. Further details of the protocol are given in Appendix A or in the PhD thesis by K. Bedner[65].

Figure 2.2: Overview of the fabrication process. Schematic structure of three SiNWs. (a) The pattern is defined by e-beam lithography. RIE and TMAH etching are used to carve out the structures. (b) The source and drain contact areas are implanted with BF_2^+ ions. (c) Buffered HF and RCA cleaning are used to get rid of the top oxide as well as organic and metallic contaminations. (d) Atomic layer deposition of Al_2O_3 or HfO_2. (e) Etching of the ALD layer to open the contact regions. (f) Contact metallization with AlSi(1%). (g) Evaporation of a gold film for the gold-coated SiNWs. (h) Contact sealing and definition of the liquid channel in SU-8 photoresist.
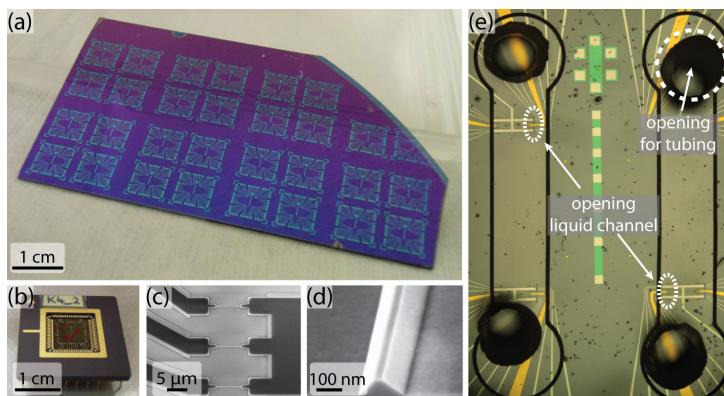
Figure 2.3: (a) Optical image of a wafer part after lithography. (b) Chip after bonding into a chip carrier. (c) SEM micrograph of a pixel with three nanowires. The dark area are the highly doped contact regions. (d) SEM micrograph of a single nanowire. (e) Optical micrograph of a sample covered with PDMS having two individual microchannels.

2.2 Liquid Measurements

For the measurements of the SiNWs in contact with electrolyte solutions different flow cells and measurement instruments have been used during the project. Here we focus on the most advanced stage which we used for most of the experiments. A leakage free system with small volume is beneficial due to a fast exchange of analyte solution and shorter molecular diffusion length. At the same time the electric potential of the solution needs to be well controlled. A simultaneous and fast electrical readout of multiple SiNWs is needed for differential or time resolved correlation experiments. Short measurement and liquid exchange times are advantageous to minimize the influence of drift.

2.2.1 Liquid Cell

The flow cell (Fig. 2.5) was carved out of a piece polyether ether ketone (PEEK). The opening which is pressed onto the sample is sealed with an o-ring. A platinum wire and a Ag/AgCl reference electrode (MI-401F, *Microelectrodes*, *Inc.*) are included in the cell to apply and control the liquid potential. To seal the electrodes and the polytetrafluoroethylene (PTFE, *Teflon*) inlet and outlet tubes, the cell was grouted in polydimethylsiloxane

(PDMS). The total cell volume was $\approx 15\,\mu$l.

To achieve even smaller volumes, PDMS microchannels were used as flow cell. The microchannels were produced by pouring PDMS (*SYLGARD 184 Silicone Elastomer*) onto SU-8 (*SU-8 100 MicroChem*) patterned Si wafers (layout Fig. 2.1 d), degassing, and heating at 60°C for 2 h for cross-linking. Afterwards, the PDMS was peeled off the substrate and pierced to insert the PTFE tubes. A *16-702 Flow-thru* Ag/AgCl Reference Microelectrode (*Microelectrodes, Inc.*) included in the tubing was used to control the liquid potential. The SU-8 molds were defined in $100\,\mu$m thick SU-8 layers by e-beam lithography.

Although the PDMS had good adhesion on the sample surface (SU-8 liquid protection layer), a strong binding was not desired. On the contrary, being able to remove the microchannel from the sample allowed surface cleaning with UV-ozone or O_2-plasma. The microchannels were merely pressed onto the samples. To achieve better mechanical support and sealing of the in- and outlets, the microchannels were grouted into a second layer of PDMS as shown in Fig. 2.4 b.

2.2.2 Measurement Setup

A peristaltic pump *(MCP, Ismatec)* and a valve selector system (*CHEMINERT VICI, Valco Instruments Co. Inc.*) were used to exchange the solutions. The liquid potential was applied to the platinum electrode and controlled by the reference electrode (V_{ref}), or directly applied to the reference electrode. A *Keithley 2636A* source meter with two channels was used to apply the source drain bias V_{sd} and to measure source drain current I_{sd}. A switching box (*Keithley 3706*) was used to address all the 48 NWs on the chip. The back gate-voltage V_{bg} was applied at the handle wafer. All devices were automatically controlled by a self-made LabView program. Fig. 2.4 and 2.5 present the measurement setup for the two different liquid cells.

Measurement Procedure

Basically two different measurement procedures were used. A steady state measurement to determine the shift in surface potential due to a change in analyte solution and a time-resolved measurement to study binding kinetics.

Samples without surface functionalization were UV-ozone cleaned for 10-20 min. Functionalized samples were treated as described in section 2.3. Prior to a measurement series, the samples were left in contact with the solution for ≈ 1 h to stabilize the sensor/solution interface.
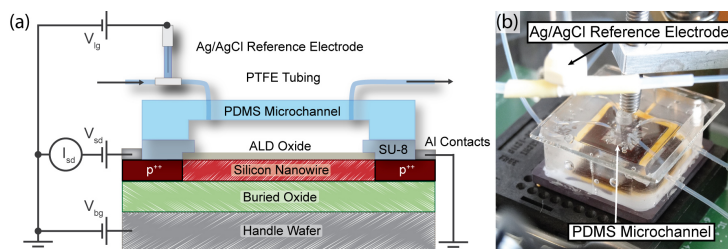
Figure 2.4: (a) Cross section of the fabricated device and a sketch of the measurement setup (not to scale). The liquid is delivered to the custom-made PDMS microchannels by a pump (indicated by arrows). A flow-through Ag/AgCl reference electrode is integrated in the Teflon (PTFE) tubing close to the microchannel. The working point of the nanowire transistor is adjusted by the liquid gate voltage V_{ref} applied to the reference electrode. A constant source-drain voltage $V_{sd} = 0.1\,\mathrm{V}$ drives the source-drain current through the nanowire channel I_{sd}.[51] (b) Sensor with grouted PDMS microchannel and a Ag/AgCl reference electrode connected to the PDMS tubing.
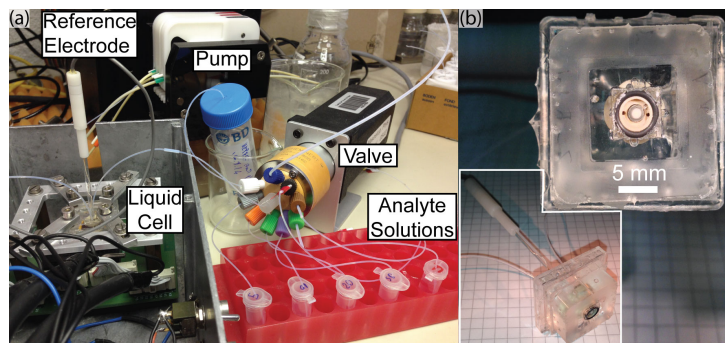
Figure 2.5: (a) Arrangement of the liquid measurement setup. A peristaltic pump is used to pull the liquid through the liquid cell, mounted on the SiNW sensor. A switching valve is used to select the different analyte solutions. The length of the tubing and the volume needed for the reference electrode are the limiting factors to further reduce the total sample volume. (b) Optical images of the liquid cell.

To obtain the shift in surface potential, the liquid potential was changed while the conductance of each SiNW was measured sequentially by addressing it via the switching unit and applying the source-drain voltage $V_{sd} = 100\,mV$. Thereby, we obtained the SiNW transfer curve to read out the threshold voltage. After having changed the solutions, the samples were stabilized for a few minutes to reach equilibrium before each measurement. Depending on the number of wires and the voltage step size, a bidirectional sweep of V_{ref} took several minutes. Typically eight solutions of different analyte concentrations were measured up and down. Such a measurement took 60-90 min including pump and stabilization time.

For time-resolved measurements the liquid potential was kept constant while I_{sd} was measured as a function of time. Ideally, a constant liquid flow rate of $\approx 20 - 40\,\mu l/min$ was used. However, when using the PDMS microchannels discontinuous flow (to exchange solutions) was better, since the liquid gating was less stable due to moving air bubbles in the system.

The global back-gate was used to reach the optimal operation regime. However, during most of the measurements the back-gate voltage was fixed to 0 V. More detailed studies of back-gate dependence were published earlier. We showed how the dual-gating can be used to amplify the pH response by taking the capacitance ratio between liquid- and back-gate into account[3]. *Tarasov et al.* showed how to minimize the 1/f noise for SiNWs without implanted contacts by using the back-gate[72].

Threshold Voltage Readout

To extract the threshold voltage from the transfer curves ($G(V_{ref})$) a *MAT-LAB* (*MathWorks*) script was used. For reasons of simplification the threshold voltage was arbitrarily defined at a given conductance value in the sub-threshold regime (usually at 20 nS). V_{th} is extracted from V_{ref} by interpolating of the two closest data points at a given conductance. Plotting V_{th} as a function of analyte concentration shows the change in surface potential.

2.3 Surface Functionalization

In order to achieve the selective sensing of distinct species other than protons, the sensor surface needs to be modified in such a way that only the targeted analyte gets adsorbed. Different methods were developed during this thesis (in collaboration with the Nanotechnology group at *Fachhochschule Nordwestschweiz*, Department of Pharmaceutical Sciences and the Department of Chemistry at *University of Basel*). The covalent chemical anchoring

of linker molecules has proven to be a viable method. Self-assembled mono-layers (SAMs) exhibit the linker binding sites close to the FET surface at a high density. The field of SAMs has extensively been studied[73]. In ISFET systems, a widely used method is the self-assembly of silane monolayers to modify various types of oxide surfaces.[2,6,10]. The silanes can either be specific on their own or can be used as linkers for further functionalization steps. Silanization can be applied for various types of oxide surfaces. Prior to the silanization the samples were cleaned with ethanol and activated (hy-droxylated) by a UV-ozone or O_2-plasma treatment. The sample surfaces were then modified either by vapour phase or liquid phase self assembly of the silanes. Liquid phase functionalization was done by using the PDMS microchannels to individually functionalize different SiNW arrays. Accord-ing to the analyte we used different types of dimethylmethoxysilanes, which have only one binding site and hence do not polymerize on the surface dur-ing the SAM formation. The layer density strongly depends on the reaction time. Following the reaction, the samples were cleaned with ethanol and cured at 80°C for $1-2$ h. Contact angle and ellipsometry measurements on control samples (*i.e.* roughly $1\,cm^2$ large Si wafer pieces) were used as meth-ods to control the reactions.

Gold-Coated Silicon Nanowires

With the idea of having a reduced pH response and the possibility of using different surface chemistry we covered the SiNWs with a thin gold layer. A 5 nm chromium adhesion layer and a 20 nm gold film was evaporated onto the Al_2O_3 or HfO_2 dielectric layer. More details are provided in chapter 4 and in reference[58]. Having gold as surface material we were able to use thiol molecules for the formation of SAMs. The molecules were dissolved in ethanol or methanol at a concentration of $\approx 2\,mM$. The SAMs were obtained by pumping the solution through the (active) microchannels with long sta-bilization intervals for 16 h. After the functionalization, the channels were rinsed with ethanol and deionized water.

3

Characterization of Silicon Nanowire Sensors

In the previous chapter, we described the fabrication and measurement techniques. In the following, the sensor performance is investigated. The characterization of SiNWFET operated in liquid is done by analyzing the transfer curve, 1/f noise and the influence of the FET channel width. Furthermore, this chapter discusses the dielectric's performance regarding pH response and background ion concentration and also stability issues. It is important to understand the individual effects to gain the right information out of often superimposed signals.

3.1 Electrical Characterization

The transfer characteristic of SiNWFET sensors was characterized in pH buffer solutions. Fig. 3.1 shows the transfer curve of a $1\,\mu$m wide SiNW were conductance G is plotted on a linear and logarithmic scale *vs.* the gate-drain voltage measured at the reference electrode V_{ref}. The source-drain and back-gate voltage were kept constant at $V_{sd} = 0.1\,$V and $V_{bg} = 0\,$V, respectively. Due to the low p-type doping the transistor is in depletion at low and positive liquid gating. The off-state conductance is limited by leakage currents from the solution to the SiNW and the source and drain contacts, which is in the order of a few hundred pico ampere. This is at least three orders of magnitude smaller than the on-state channel current. Gating via the electrolyte solution increases leakage currents compared to the use of a metal gate. The origin of the leakage current is assumed to be diffusion

of protons through the gate oxide. Various theories assume electrochemical reactions including hydrogen at the direct vicinity of the oxide surface, both, within the oxide layer and at the oxide silicon interface[74,75]. By using atomic layer deposition technique to deposit the Al_2O_3 and HfO_2 gate oxides and a SU-8 photoresist protection layer to cover the contacts, leakage currents were suppressed to be lower as a few hundred pico ampere. Conductance in inversion (at more positive gate voltage) is suppressed by the p-n junctions at the highly p-doped contacts.

At low negative gate voltage, holes accumulate and the subthreshold conductance starts. As described in section 1.1 the subthreshold swing is given by the total liquid gate capacitance, including C_{ox}, C_{dl} and trap states. Typically, values between 120 and 180 mV/dec were obtained. At more negative voltage the linear regime starts. Here, the conductance is directly proportional to V_{ref}. At even higher negative voltage the serial resistance of the contacts starts to dominate and the SiNW conductance starts to saturate. On-off-current ratios I_{on}/I_{off} between 10^3 and 10^5 were obtained, depending on the SiNW dimension. The transconductance, which is the slope of the transfer curve $g_m = \partial I_{sd}/\partial V_{ref}$, is usually read out in the linear regime, where it is constant. Unlike the common definition of the threshold voltage, which is at the transition from exponential to linear gate dependence, we define V_{th} at a given conductance value in the subthreshold regime to simplify the readout. Usually $G = 20$ nS was chosen because it is deep inside the subthreshold regime and still above the level from the leakage current. From Eq. 1.10 follows that V_{th} depends on the properties of the gate dielectric and the surface potential, given by the composition of the solution.

Both g_m and V_{th} are dependent on the back-gate voltage, since it also influences the surface potential at the liquid gate[35]. At negative V_{bg} an increase in V_{th} is observed. However, at high negative back-gate voltage the subthreshold swing degrades, caused by a current that flows at the back interface. Due to this reason V_{bg} was usually set to 0 V. Studies on the influence of the back-gate on transfer curve[64], pH response[3] and $1/f$ noise in SiNWs with undoped contacts[72] have been done prior to this work.

The hysteresis in the transfer curve upon sweeping of the liquid gate is small. Usually, variations < 5 mV were measured. The hysteresis corresponds to the amount of charge trap states in the gate oxide and on the sensor surface. We see a clear dependence of the SiNW width on transconductance and threshold voltage (as seen in Fig. 3.3 a). Where the change in transconductance can be explained by the effective wire width (top and sidewalls), the cause for the shift in V_{th} is expected to be due to different electrostatic coupling between liquid and back gate. A detailed study on SiNW width

dependence and the influence of dielectric material and thickness is given in the PhD thesis by K. Bedner[65] and references[53,70].
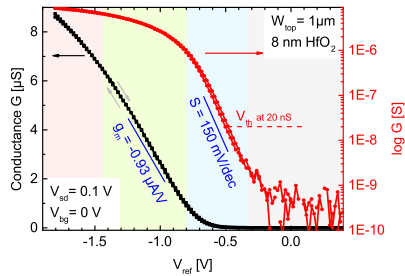

Figure 3.1: Transfer curve of a $1\,\mu$m wide SiNW with $8\,$nm HfO$_2$ as gate oxide measured in pH 3 buffer solution at $V_{sd} = 0.1\,$V and $V_{bg} = 0\,$V. Conductance G on linear (black) and logarithmic (red) scale *vs.* reference electrode voltage V_{ref}. The blue lines indicate transconductance g_m and subthreshold swing S. The background indicates the different regimes: Contact dominated, linear, subthreshold and leakage (from left to right).

3.2 1/f Noise Investigations

As we have seen in section 1.2, the evaluation of noise is important, since it ultimately defines the resolution and hence the detection limit of the sensor. We measured the low-frequency $1/f$ noise of our SiNWs of different widths and gate oxide capacitance. For further details the reader is referred to the PhD thesis of K. Bedner and reference[53].

3.2.1 Noise Measurement Setup

A special set-up was used for the noise measurements. The schematics is shown in Fig. 3.2. A 9-Volt battery and a voltage divider were used to apply the DC source-drain voltage. The gate voltage was applied to the platinum electrode and measured at the reference electrode. The conductance of the SiNW was measured by a *National Instrument* DAQ board using a current-voltage converter (variable gain from -10^5 to $-10^9\,$V/A). Via fast Fourier transformation a noise spectrum was obtained from the time dependent voltage signal. Measurements were performed in pH 7 buffer solution, deionized water and argon. In the latter case, the device was gated by the back-gate.
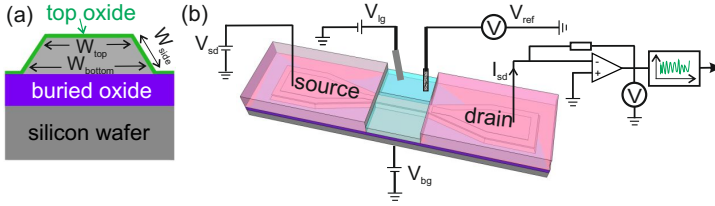
Figure 3.2: Noise measurement setup. (a) Cross section of a SiNW. Due to the anisotropic silicon etch, the side walls have an angle of $54.7°$. The width of the SiNWs is referred to the top width (W_{top}). However, the effective gated width is $W_{eff} = W_{top} + 2W_{side}$. (b) Schematics of the noise measurement setup. A DC source-drain voltage of 90 mV was applied to an individual SiNW. The source-drain current I_{sd} is measured by a DAQ board using a current-voltage converter. V_{lg} is applied at the platinum electrode, V_{bg} to the handle wafer and V_{ref} is measured at the reference electrode. (Figure from reference [53])

3.2.2 1/f Noise in Silicon Nanowire Sensors

Figure 3.3a shows the transfer characteristics of SiNWs of different widths. At the given conductance values a noise spectrum was recorded. Fig. 3.3 b depicts the frequency dependence of the noise power per unit of bandwidth of a 100 nm wide SiNW with 20 nm Al_2O_3 as gate oxide, measured in pH 7 buffer solution. The input referred voltage noise $S_V(f)$ is calculated with the SiNW resistance R and the gain of the I-V converter G.

$$S_V(f) = \left(\frac{R}{G}\right)^2 S_{V,\,\text{measured}}(f) \tag{3.1}$$

The corresponding thermal background noise, measured at zero bias, has been subtracted from the data. The thermal noise agrees with the theoretical value given by $S_{JN} = 4k_bTR$ (Eq. 1.26). In the analyzed conductance and frequency regime, $S_V(f)$ follows $1/f$, as indicated by the dashed line.

In reference [53], we find that noise is mainly generated by the gate oxide and not in the SiNW itself. The main noise source is the trapping and release of charge carriers at trap states near the semiconductor-oxide interface. The trap state noise model is described in section 1.2.1 with Eq. 1.28. The extracted trap state density per area was $N_{ot} = 2.5 \cdot 10^8 \, \text{cm}^{-2}$, which is in the expected range [76,77] and low compared to similar structures [78,79]. To calculate the gate referred noise S_{VG} at 10 Hz we use the relation

$$S_{VG} = \frac{S_V(10\,\text{Hz})}{(R \cdot g_m)^2} \tag{3.2}$$
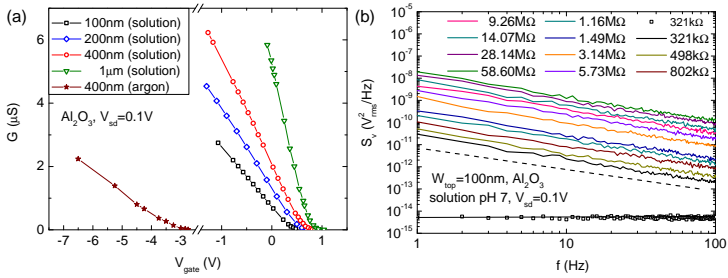
Figure 3.3: (a) Conductance G *vs.* gate voltage V_{gate} for SiNWs of different widths measured in pH 7 buffer solution (open symbols, liquid gated) or argon (full symbols, substrate gated). (b) Power spectral density of the voltage fluctuations S_V *vs.* frequency f for a 100 nm wide SiNW with 20 nm Al_2O_3 as gate oxide. The dashed black line indicates $1/f$ characteristics. Black open symbols show the thermal noise for the SiNW gated to 321 kΩ, which is not frequency dependent. The corresponding black line indicates the theoretical value of the thermal noise. (Figure from reference [53])

where the slope $g_m = \partial I_{sd}/\partial V_{ref}$ is taken from the transfer curve. Fig. 3.4 shows the gate-referred voltage noise of SiNWs of different widths (with 20 nm Al_2O_3 as gate oxide). On the one hand, Fig. 3.4 a compares S_{VG} for a 400 nm wide SiNW measured in pH 7 buffer solution and DI water. S_{VG} remains constant over a wide range of resistance values (SiNW regime; linear and subthreshold) and slightly increases for low resistance values when the total resistance starts to be dominated by the contact resistance (contact regime). Both, pH buffer solution and DI water show a similar noise level, suggesting that the ions in the buffer solution do not significantly influence the noise behaviour. When measuring in argon/air atmosphere, the SiNW is gated by the back-gate. A higher noise level is measured, due to the much smaller gate capacitance. On the other hand, Fig. 3.4 b compares S_{VG} for wires of different width, by normalizing S_{VG} and R to an effective width of 1 μm. The data for all different widths falls on top of each other with a constant value in the SiNW regime and an increase in the contact regime. This follows the trap state model (Eq. 1.28) according to $S_{VG} \propto 1/W_{eff}$, where the noise increases with decreasing wire width. The sensor resolution limit $\Delta\Psi_{0,min}$ directly corresponds to $\sqrt{S_{VG}}$. The lowest value of $1 \cdot 10^{-5}$ V/Hz$^{1/2}$ measured at 10 Hz with 1 Hz bandwidth was measured for the SiNW with $W_{top} = 1$ μm. This corresponds to a resolution limit of 0.017% of an ideal pH shift of 60 mV/pH.
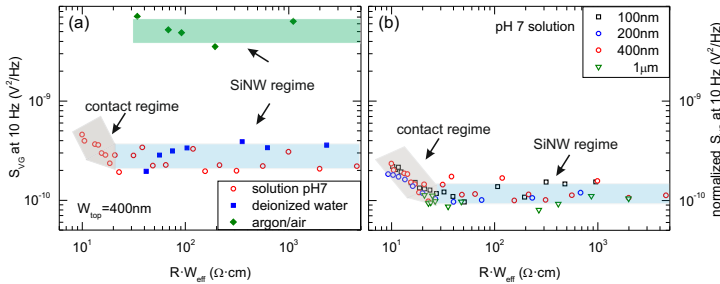
Figure 3.4: (a) Gate referred voltage noise S_{VG} at $10\,\text{Hz}$ of a $400\,\text{nm}$ wide SiNW *vs.* resistance R times effective SiNW width W_{eff}, measured in pH 7 buffer solution, deionized water and argon/air mixture. (b) S_{VG} normalized by W_{eff} relative to the SiNW with $W_{top} = 1\,\mu\text{m}$ *vs.* R, measured in pH 7 buffer solution. (Figure from reference [53])

1/f Noise in Gold-Coated Silicon Nanowires

Samples from a different production run, also having $20\,\text{nm}$ Al_2O_3 as gate oxide, were used to analyze the influence of a floating gold film on top of the SiNW on $1/f$ noise. Fig. 3.5 a shows the transfer curve and the corresponding transconductance for a $1\,\mu\text{m}$ wide SiNW with Al_2O_3 surface. In Fig. 3.5 b the unnormalized values of S_{VG} at $10\,\text{Hz}$ *vs.* resistance for $1\,\mu\text{m}$ wide SiNWs and $25\,\mu\text{m}$ wide SiNWs with gold and Al_2O_3 surface exemplify that the wide SiNWs have a lower noise level according to $S_{VG} \propto 1/W_{eff}$. A noise level of $\sqrt{S_{VG}} = 3 \cdot 10^{-6}\,\text{V/Hz}^{1/2}$ for $1\,\mu\text{m}$ wide SiNWs and $6 \cdot 10^{-7}\,\text{V/Hz}^{1/2}$ for $25\,\mu\text{m}$ wide SiNWs was measured at $10\,\text{Hz}$ with $1\,\text{Hz}$ bandwidth. However, we observed no clear difference between the two distinct surfaces. The assumption that the gold film could reduce the gate referred noise by screening surface charges does not hold. This is a further evidence that $1/f$ noise is mainly generated by trap states in the gate oxide and not by ions in the solution. As compared to Fig. 3.4 b, S_{VG} in Fig. 3.5 b is one order of magnitude larger. This could be explained by the different production runs, since batch-to-batch variations in the trap state density are not unexpected.

3.2.3 RMS Noise in Time-Resolved Measurements

With the $1/f$ noise analysis the theoretical resolution $\Delta\Psi_{0,\text{min}}$ can be obtained at a given frequency and bandwidth. As we have seen, $1/f$ noise is an intrinsic property of the SiNWs and, hence, this is the best method for
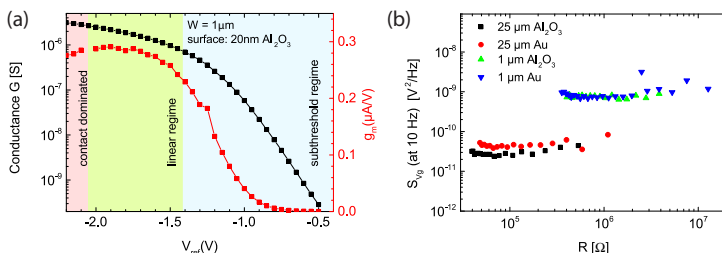
Figure 3.5: (a) Conductance G (black, left axis) and transconductance $g_m = \partial I_{sd}/\partial V_{ref}$ (red, right axis) vs. gate voltage V_{ref}. The transconductance reaches its maximum in the linear regime and drops as soon as the contact dominated regime starts. (b) Unnormalized S_{VG} at 10 Hz vs. resistance for 1 μm nanowires and 25 μm SiNWs with gold and Al_2O_3 surfaces measured in pH 7 buffer solution.

benchmarking. However, for time-resolved measurements the root mean square (RMS) noise and peak-to-peak variations are easier to extract. In order to obtain the RMS noise, the noise spectral density curve can be integrated over the bandwidth of interest.

$$\text{Noise}_{\text{RMS}} = \sqrt{\int_{f_{\text{low}}}^{f_{\text{high}}} S_{VG}(f)\,df} \qquad (3.3)$$

In Fig. 3.6 the change in surface potential ($\Delta\Psi_0 = I_{sd}/g_m$) is plotted against time for two gold-coated SiNWs of 1 μm and 25 μm width. The surface of the SiNWs is functionalized with a monolayer which is selective to a certain protein. The electrolyte solution is 10 mM HEPES buffer at pH 8. This system will be explained in chapter 5. For a typical sensing measurement the sampling rate is in the order of $1 - 10$ Hz, and the measurement takes about $10 - 60$ min. If f_{low} and f_{high} are set to 0.001 Hz and 10 Hz and taking the $\sqrt{S_{VG}}$ values from the $1/f$ measurements, the calculated RMS noise is around 300 μV and 60 μV for the 1 μm and 25 μm wide SiNWs, which is close to the measured values in Fig. 3.3. However, the conditions for the two different types of noise measurements are not entirely comparable. The slightly increased noise could be explained by considering the fact that a different sample was used, or by external contributions, such as the different measurement setup. Particularly the switching of I_{sd} between the measurement points (which was needed to individually address several SiNWs) induces noise. Nevertheless, comparing the RMS noise among the two wires of different areas displays the width dependency on the resolution $\Delta\Psi_0 \propto \sqrt{\text{area}}$

accurately. The peak-to-peak values can be defined in various ways. If we want to include 99.9% of the peaks we have to take 6.6 times the standard deviation. This results in peak-to-peak values of 2.1 mV and 0.4 mV for the 1 μm and 25 μm wide wires respectively.
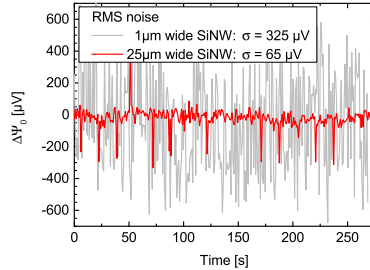
Figure 3.6: Surface potential fluctuations ($\Delta\Psi = I_{sd}/g_m$) in a time-resolved measurement for two different gold-coated SiNWs of 1 μm and 25 μm width measured in the switching setup. The RMS noise which is equivalent to the standard deviation of the measurement points ($\sigma = \sqrt{\text{variance}}$) scales with $\sqrt{\text{area}}$.

3.2.4 Conclusion of the Noise Studies

We have studied the low-frequency $1/f$ noise in silicon nanowire and nanoribbon FET sensors. The relevant figure of merit for sensing is the gate referred voltage noise. It removes the dependence on g_m and allows to focus on the minimum detectable voltage change. We found that S_{VG} is constant over a large operation range (linear and subthreshold regime), as long as the intrinsic FET resistance dominates and the contact resistance can be neglected. Further, S_{VG} inversely scales with the channel area. Hence, the signal-to-noise ratio is better for larger sensors, as long as the response to the analyte is independent of the sensor size.

A constant value of S_{VG} within a wide range of parameters suggest that the noise is dominantly generated by the gate. We have shown that the noise does not depend on the ion concentration in the electrolyte solution. Therefore, the source of the noise is not at the sensor-electrolyte interface, but most likely at the interface between the gate oxide and the transistor channel.

A resolution limit $\Delta\Psi_{0,\text{min}}$ of $\sqrt{S_{VG}} = 1 \cdot 10^{-5}\,\text{V/Hz}^{1/2}$ was measured at 10 Hz with 1 Hz bandwidth for a 1 μm wide SiNW. For the latest batch

$3 \cdot 10^{-5}$ V/Hz$^{1/2}$ for $1\,\mu m$ wide SiNWs and $6 \cdot 10^{-6}$ V/Hz$^{1/2}$ for $25\,\mu m$ wide nanoribbons measured at 10 Hz with 1 Hz bandwidth was achieved. The signal-to-noise ratio is shown to increase with $\sqrt{\text{area}}$.

These values are more than one order of magnitude better as compared to the similar structures in reference [78–80], where SiO_2 was used as gate dielectric. Noise has also been studied in transistors made of other materials such as carbon nanotubes (CNT) and graphene [81–84]. A comparison of the noise level between those systems and our SiNW sensor is possible after a rescaling to the reference SiNW of $W_{top} = 1\mu$. A noise level of $\sqrt{S_{VG}} = 7.1 \cdot 10^{-6}$ V/Hz$^{1/2}$ and $5.5 \cdot 10^{-5}$ V/Hz$^{1/2}$ reveals for the CNT and the graphene transistor, respectively.

3.3 pH Sensing

The surface potential at the sensor interface strongly depends on the pH of the electrolyte solution, as described by the site-binding model in section 1.1.3. Fig. 3.7 a and c show how the change in surface potential affects the transfer curve and, hence, the threshold voltage. The curves shift to more positive gate values with increasing pH. Since a reference electrode was used, the change in threshold voltage ΔV_{th} directly reveals the change in surface potential $-\Delta\Psi_0$. The opposite sign is due to holes as majority charge carriers. Plotting V_{th} as a function of pH reveals the pH response (Fig. 3.7 b). The average value is extracted from the linear fits to these data points. For UV-ozone cleaned Al_2O_3 and HfO_2 surfaces, a linear response of ≈ 56 mV/pH is observed in the pH range from 3 to 10. This value is close to the Nernst limit of 58.2 mV/pH at 20°C. This result is associated to the high quality of the ALD oxide layers that provide a large number of proton sensitive surface hydroxyl groups. The relative shifts ΔV_{th} are independent of the ionic strength (Fig. 3.7 b). This will be further explained in the next section.

Alternatively, the source-drain current I_{sd} can be measured as a function of time, as indicated in Fig. 3.7 d. If the working point is chosen such that the NWs are operated in the linear regime, the transconductance g_m can be used to calculate the change in threshold voltage $\Delta V_{th} = I_{sd}/g_m$. g_m is extracted from the linear regime in Fig. 3.7 c. The step height is close to the Nernst limit, as indicated by the horizontal grid lines. The response time upon changing the pH buffer solution is mainly limited by the fluidic system due to solution mixing and diffusion. Sensor response times below 200 ms have been achieved at high liquid exchange rates.

We see no impact of SiNW width on pH sensing. Fig. 3.7 e demonstrates

that for both surfaces, Al_2O_3 and HfO_2, all SiNWs of widths ranging from 100 nm up to 25 μm show the same response to pH. Although the absolute threshold voltage depends on the SiNW geometry, dopant concentration and gate dielectric, ΔV_{th} is only given by the change in surface potential. From Eq. 1.24, we see that the response is given by the density of reactive surface groups and the dissociation constants of the surface reactions. A detailed study on impact of SiNW width on pH response is presented in reference[70].

3.3.1 Surface Passivation

We have seen that Al_2O_3 and HfO_2 are good candidates for pH sensing. However, to be sensitive to other species than protons, the high density of surface hydroxyl groups becomes disadvantageous. As described in section 1.2.4, competing surface reactions prevent selective sensing at high sensitivity. Besides the potential to reduce interference from protons, passivation of surface hydroxyl groups can also be used to realize a nanoscale reference electrode. The on-chip integration of a reference electrode that only reacts to the changes of the electrostatic potential but not to the chemical one, is a major challenge in the field of ISFETs. In reference[50] we demonstrate a reference FET, whose proton sensitivity is suppressed by as much as 2 orders of magnitude. This was achieved by passivating Al_2O_3-coated SiNWs with a self-assembled monolayer of silanes with a long alkyl chain (octadecyldimethylmethoxysilane in vapour phase, Fig. 3.8 a). To achieve full passivation, several days of self-assembling at 80°C is needed. We can estimate the density of surface hydroxyl groups by comparing the achieved pH responses after passivation with the site-binding model described in 1.1.3.

Fig. 3.8 b shows $\Delta V_{th} = V_{th}(\text{PZC}) - V_{th}$ as a function of pH for different passivation times. Without the silane (0 d) a linear, nearly nernstian response can be observed. With increasing reaction time the pH response becomes weaker and nonlinear. The saturation at low and high pH becomes narrower until the pH response is rather flat with some scattering. After a UV-ozone or a mild O_2-plasma cleaning the pH response can be almost fully restored (55 mV/pH, empty squares). We fit the data using the site-binding model (Eq. 1.24) to obtain the number of active surface sites N_s. Because a single sigmoid shape is observed and a response close to the Nernst limit is found for the bare Al_2O_3 surface, a small $\Delta pK \approx 0.4$ is taken for the fits. Since the pH buffer solutions are of rather high electrolyte concentration (in total $\approx 60 - 100$ mM) the double-layer capacitance is set to $C_{dl} = 0.16$ F/m^2.

Fig. 3.9 a shows the average pH response $s_{pH} = (\Delta V_{th}(\text{pH 3}) - \Delta V_{th}(\text{pH 11}))/8$ and N_s as a function of passivation time. Both numbers monotonically decrease with increasing passivation time. Contact angle
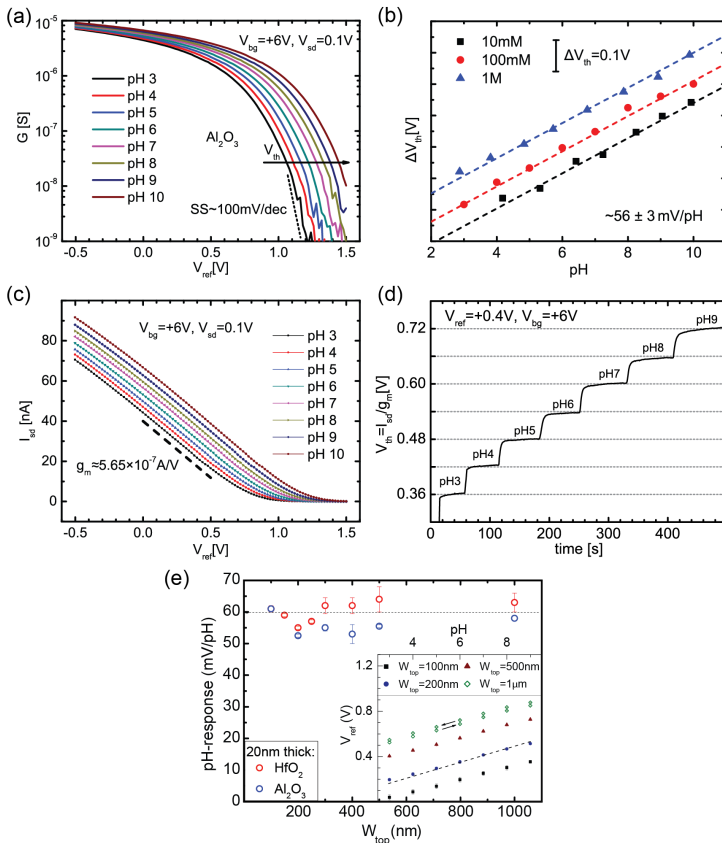
Figure 3.7: Transfer curve for an Al_2O_3-coated nanowire measured in different pH buffer solutions. (a) I_{sd} *vs.* V_{ref} on a linear scale. (c) G *vs.* V_{ref} on a semilog plot. The curves shift linearly to more positive V_{ref} values with increasing pH. The transconductance can be extracted from the linear region. V_{th} at a given conductance value is extracted in the subthreshold region. (b) Threshold voltage shift ΔV_{th} for three different ionic strengths of the electrolyte. ΔV_{th} is a linear function of pH with the slope of $\approx 56\,mV/pH$ (indicated by the dashed lines). No significant dependence of the slope on the ionic strength is found. (d) Time resolved pH meaurement (I_{sd} *vs.* time). The measured I_{sd} was divided by g_m to obtain the shift in threshold voltage ΔV_{th}. The step height is close to the Nernst limit (58.2 mV/pH at 20°C, indicated by horizontal grid lines). (e) The pH response of Al_2O_3 and HfO_2-coated SiNWs with W_{top} ranging from 100 nm to 1 μm is close to the Nernst limit. An effect of the width is not observed. Inset: Liquid potential V_{ref} extracted at 20 nS *vs.* pH. For all widths a linear dependence is found over the whole pH range. Figures taken from reference [51,70].
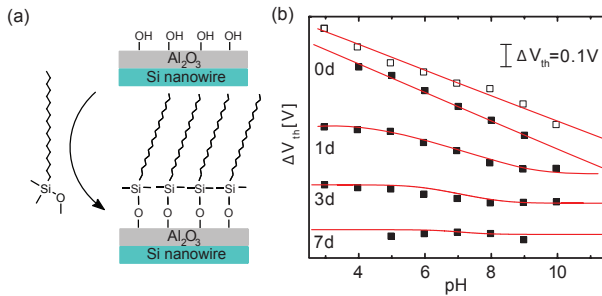
Figure 3.8: (a) Schematics of the chemical modification of a UV-ozone activated Al_2O_3 surface. Vapour phase deposition of octadecyldimethylmethoxysilane replaces hydroxyl groups by alkane chains. The reaction time varied between 6 h and 7 days. (b) Change in threshold voltage $\Delta V_{th} = V_{th}(\text{PZC}) - V_{th}$ of Al_2O_3-coated SiNWs $vs.$ pH of the buffer solution for several reaction times (from top to bottom: 0 to 7 days). Empty squares after 7 days passivation and subsequent cleaning. Nonlinear curves are fits of the site-binding model with following parameters: $\Delta pK \approx 0.4$, $C_{dl} = 0.16\,\text{F/m}^{-2}$ and varying N_s. Curves are shifted for clarity. Figure adapted from reference[50].

(CA) measurements on test wafers were used to get a control about the surface reaction (Fig. 3.9 b). A rapid increase in CA from $\approx 0°$ (UV-ozone activated) to $70 - 80°$ is observed within the first hours. After it saturates around $102 - 105°$. Macroscopically the hydrophobic nature is achieved in less than two days. Nevertheless, a longer reaction time is needed for a proton tight surface.

A different approach to reduce the number of hydroxyl groups is to take a surface with intrinsically low N_s. As we will describe in the following chapters 4 and 5, we used a gold surface for the selective detection of other species than protons.

3.4 Electrolyte Concentration

Understanding the influence of the electrolyte background on the sensor response is important for biochemical sensing. There are several studies on adsorption of inorganic salt ions on colloidal oxide surfaces[85,86], glass electrodes[87–89] and ISFETs[90,91]. Different models have been developed over the past decades, such as surface complexation of ions with oppositely charged oxide sites and the semi-empirical Nikolky-Eisenmann equation. However, for nanoscale ISFETs, inconsistent results have been published so far. Zafar and co-workers did not observe any response from HfO_2-coated SiNWs to
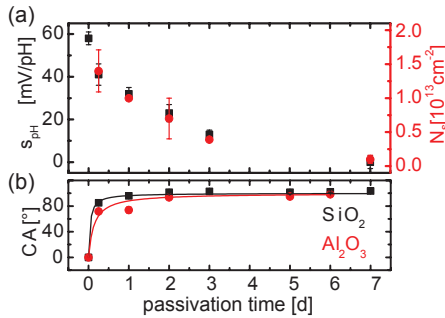
Figure 3.9: (a) Average pH response s_{pH} and density of surface hydroxyl groups N_s vs. passivation times. N_s is obtained from the fits in Fig. 3.8 b. (b) Contact angle (CA) of a water droplet on a test wafer surface (SiO$_2$, squares; Al$_2$O$_3$, circles) vs. passivation time. Figure adapted from reference [50].

ionic strength up to 1 M [92], Nikolaides et al. [93] and Park et al. [62] reported a weak nonlinear response of SiO$_2$-coated FETs to KCl or NaCl and Clément et al. [77] claimed full linear response of ≈ 60 mV/dec to NaCl with SiO$_2$-coated SiNWs.

We have studied the response of Al$_2$O$_3$ and HfO$_2$-coated SiNWs to changes in KCl concentration up to 1 M, and observed a nonlinear behaviour, which does not depend on the pH of the solution. In reference [51] we compare the results with three different models and propose a new adsorption model, which agrees better with our measurements and will be presented in the following. For further details the reader is referred to the PhD thesis of A. Tarasov [94].

In Fig. 3.7 b in the previous section we see that the pH response of Al$_2$O$_3$-coated SiNWs is independent of the ionic strength of the pH buffer solutions. Similar results were obtained for HfO$_2$-coated samples. Fig. 3.10 shows that V_{th} goes to more positive voltage at higher KCl concentration. This shift is nonlinear. Up to 10 mM almost no shift occurs. At higher concentration the response becomes close to nernstian. We conclude that the positive shift occurs due to adsorption of anions. In the case of Fig. 3.10 the chloride ion. Yet, we found similar results for sodium nitrate and sodium sulphate [51].

In addition to the protonation and deprotonation reaction of the site-binding model (see section 1.1.3) we propose a complexation of the anion with the protonated hydroxyl groups at the oxide-electrolyte interface with the reaction constant K'_c,

$$MeOH_2^+ + Cl_s^- \rightleftharpoons MeOHCl^- + H_b^+, \ K_c' = \frac{\nu_{MeOHCl^-} \cdot a_{H_b^+}}{\nu_{MeOH_2^+} \cdot a_{Cl_s^-}} \qquad (3.4)$$
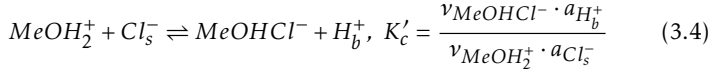
with ν being the density of sites and a the activity of a particular species. Index (s, b) denote surface or bulk concentration. We deduce a value of $K_c' \approx 3.3 \cdot 10^{-6}$ by fitting the extended site-binding model to our data. We set the parameters as follows: $K_a = K_b = 10^{-7}$, $N_s = 10^{19}\,\mathrm{m}^{-2}$ and $C_{dl} = 0.16\,\mathrm{F/m}^2$. These values agree with the high pH response and N_s corresponds to the upper limit for oxide surfaces. Fig. 3.10 b shows that our model agrees well with the data obtained for increasing electrolyte concentration at different pH values. The model can be solved analytically, if a constant double layer capacitance is assumed. This holds as long as the surface buffer capacitance C_s is much larger as C_{dl} (in other words, for a large N_s - see Eq. 1.25). For surfaces showing a low pH response, the effect of C_{dl} starts to play a role. Furthermore, in the measured concentration range C_{dl} is always larger than the gate oxide capacitance. Therefore, the total gate capacitance is always dominated by C_{ox} and the ion concentration has no influence on the FET transfer curve (see appendix B).

Eq. 3.4 implies that a chloride ion from the solution forms a complex with the surface hydroxyl group and replaces a proton at the surface, which goes to the bulk solution. The reaction constant K_c' is therefore not a true chemical equilibrium constant for a local system. However, if the equation is expressed only in local surface concentrations it does not explain the measured data. Eq. 3.4 has to be considered as a substitute equation, solving the discrepancy between our measurements and the previously mentioned models by an unspecific realization. Very similar results were obtained with other types of salts (NaCl, NaNO$_3$, Na$_2$SO$_4$, NaF).

3.5 Stability Measurements

Short term fluctuations and long term threshold voltage instability (drift) is a known problem for pH sensors and especially ISFET based sensor systems. Several mechanisms for drift in threshold voltage have been proposed in the literature [62]. Slow hydration of SiO$_2$ surfaces as described in reference [95] could similarly occur for other types of oxides. Ion exchange of OH$^-$ ions and incorporation in the solid [96], injection of electrons from electrolyte into the gate oxide [97] and migrations of ions such as H$^+$ and OH$^-$ into the surface [98] have also been proposed. Although the ALD technique provides a very good oxide layer quality, the stability is affected by the electrolyte conditions. *E.g.* It is known that Al$_2$O$_3$ is slowly etched at high
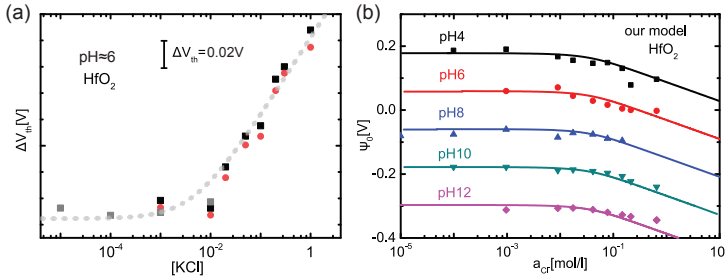
Figure 3.10: (a) Threshold shift ΔV_{th} vs. KCl concentration. Three different data sets were obtained from measurements with two different HfO$_2$-coated SiNWs. The pH value of all solutions was ≈ 6. A nonlinear response is observed. Below $10\,$mM KCl almost no shift occurs. Above this value, the response increases and gets close to the Nernst limit. The positive shift is induced by the adsorption of anions (here Cl$^-$). The dashed line is a guide to the eye. (b) The same response as in (a) plotted as surface potential $\Psi_0 = V_{th}(\text{PZC}) - V_{th}$ vs. activity of the chloride ions in the bulk solution a_{Cl^-}, measured at different pH values. The lines are theoretical fits based on our ion complexation model. Figure adapted from reference [51].

pH (>10)[99]. Functionalized surfaces are even more sensitive to the environment. Silanized surfaces degrade in highly basic conditions and self-assembled monolayers of different functionalities (CH$_3$-, OH-, and EG$_4$-) oxidize in air and water.[100]. Further, accumulation of contaminants on the sensor surface can change the surface potential. This not only affects the threshold voltage, but also the sensitivity of the sensor.

To reduce the influence of drift, shorter measurement periods are beneficial. However, the kinetics of the analyte adsorption reaction, as well as analyte diffusion limit the signal time constants. Especially at low concentration and for weakly buffered solutions this effect becomes predominant as described in section 1.2.5. For our sensor system a very small solution volume of less than $50\,\mu$l is needed, which can be exchanged rapidly ($< 20\,$s). For pH and salt concentration measurements, where rather high concentrations of small analytes are used, the stabilization time to reach equilibrium is only a few seconds. Fig. 3.11 a shows V_{th} for a Al$_2$O$_3$ and gold-coated SiNW at different pH buffer solutions measured back and forth, starting at pH 3. The time needed for this series of measurement is about $1\,$h. This is limited by the switching time which is needed to measure the transfer curve of multiple SiNWs. The total drift and fluctuations in V_{th} is very low. Fig. 3.11 b shows a time-resolved measurement, where I_{sd} was recorded while

the pH buffer solutions were changed. Due to the fast liquid exchange the response times are very low. The inset shows that 90% of the signal change is reached in 2.5 s.
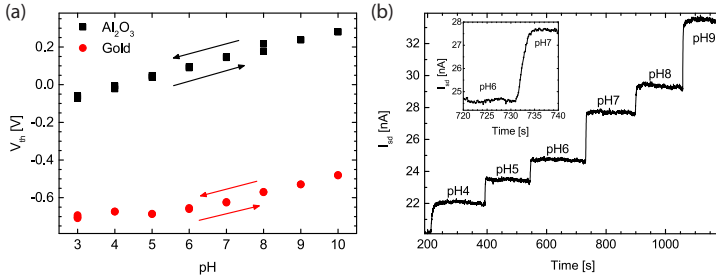
Figure 3.11: (a) V_{th} *vs.* pH for a Al_2O_3 and a gold-coated SiNW measured from pH 3 to 10 and back. Very low drift is observed, as the corresponding points overlap very well. (b) Time-resolved pH measurement of a 300 nm wide Al_2O_3-coated SiNW. I_{sd} is recorded while different pH buffer solutions are pumped through the microchannel system. The inset shows that the stabilization time upon a pH change is only a few seconds.

3.5.1 Long Term Stability

Long term stability is of crucial importance if a sensor is deployed for continuous monitoring of chemical species for long periods of time. In Fig. 3.12 the threshold voltage was monitored for 72 h, keeping the electrolyte at constant pH 7. Every 30 min the solution was replenished by a short pump interval. After a stabilization time of a few minutes the transconductance was recorded. The extracted V_{th} is plotted against time. Within the first hours a substantial drift occurs. Afterwards, the drift is reduced to 0.02 mV/h for the gold-coated SiNWs (linear fit 20 – 72 h). The drift among SiNWs of the same surface is very similar, as indicated in Fig. 3.12 b. The differential threshold voltage $\Delta V_{th} = V_{th,\,SiNW1} - V_{th,\,SiNW2}$ scatters within a few mV. The average drift deviation of the differential threshold voltage is only 0.01 mV/h for the Al_2O_3-coated SiNWs. Hence, measuring in a differential mode can compensate long term drifts.
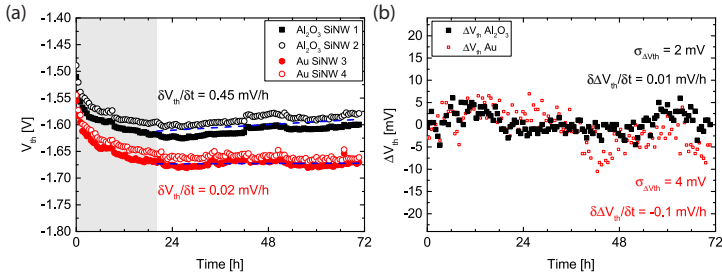
Figure 3.12: Long term stability measurement over 72 h in pH 7 buffer solution. (a) V_{th} was monitored for Al_2O_3 and gold-coated SiNWs (indicated by the dashed blue lines). Within the first hours a substantial drift can be observed. After 20 h the drift is reduced to less than 0.5 mV/h for Al_2O_3 and even 0.02 mV/h for gold-coated SiNWs. Among the same surfaces the drift of the different NWs is very similar. (b) Differential threshold voltage ΔV_{th} for two Al_2O_3 (black) and gold (red) coated NWs shifted to 0 mV. A very low drift deviation among the wires is found. The standard deviation $\sigma_{V_{th}}$ is in the range of a few mV.

3.6 Summary

In this chapter we have characterized the electrical and sensing properties of our SiNW sensors. We find good transistor characteristics in terms of leakage current, transconductance and on-off-current ratio. We have analysed the low frequency $1/f$ noise in SiNWs of different width to determine the signal-to-noise ratio over a large resistance range. The deduced sensor resolution limit $\Delta\Psi_{0,min}$ is constant over an extended operation range from the linear to the subthreshold regime. The analysis clearly shows that the resolution limit improves with increasing SiNW width. Hence, a better signal-to-noise ratio is achieved for larger sensors as long as the response to the analyte is independent of the sensor dimension.

We have measured the response to pH and electrolyte concentration for SiNWs of different width and surface material. SiNW-ISFETs with Al_2O_3 or HfO_2 exhibit a very high linear response to pH, which is close to the Nernst limit. We observe a nonlinear response to ionic strength, due to anion adsorption, which is independent of the pH. No effect of the wire width or the operating regime is observed on the pH or ionic strength response. Such background effects of the electrolyte ions have to be understood and clearly separated from the signals caused by the actual analyte. Even slight changes of the ionic strength in the physiological range can significantly influence the sensor signal. Therefore, the pH changes and ionic strength variations

should always be monitored in parallel to any other specific detection experiment.

Surface passivation of highly pH sensitive surfaces has been achieved by silanization of the surface hydroxyl groups. A gradual decrease of the pH response was observed with increasing surface coverage. A practically pH insensitive surface was achieved after reducing the density of active surface groups by approximately three orders of magnitude. Such passivated SiNWs could be used as nanoscale pH reference electrodes in a differential setup.

We have found a good long term stability of the SiNWs. The average drift rate of V_{th} is less than 0.5 mV/h and very similar among NWs with the same surface material. This is an important quality for differential and multiplexed measurements. However, drift and short term fluctuations are the main limiting factor for the signal accuracy. To reach the chemical equilibrium of the surface reactions, often measurement times of several minutes are required. Such long measurement times limit the theoretical resolution, measured by the $1/f$ noise at 10 Hz by orders of magnitude. In our system only very small analyte volumes ($< 50 \mu l$) are needed for a reliable sensor operation. This reduces the amount of sample solution and speeds up the measurement procedure, which helps to reduce the influence of drift.

4

Selective Sodium Sensing with Gold-Coated SiNWFETs in a Differential Setup

As we have seen in the last chapter, ISFETs based on silicon nanowires with high dielectric constant gate oxide layers (*e.g.* Al_2O_3 or HfO_2) display hydroxyl groups which are known to be sensitive to pH variations but also to other ions present in the electrolyte at high concentration. This intrinsically non-selective sensitivity of the oxide surface greatly complicates the selective sensing of ionic species other than protons. In this chapter, we describe the modification of individual nanowires with thin gold films as a novel approach to surface functionalization for the detection of specific analytes. We demonstrate sodium ion (Na^+) sensing by a self-assembled monolayer (SAM) of thiol-modified crown ethers in a differential measurement setup. A selective Na^+ response of $\approx -44\,mV$ per decade in a NaCl solution is achieved and tested in presence of protons (H^+), potassium (K^+), and chloride (Cl^-) ions, by measuring the difference between a nanowire with a gold surface functionalized by the SAM (active) and a nanowire with a bare gold surface (control). We find that the functional SAM does not affect the unspecific response of gold to pH and background ionic species. This represents a clear advantage of gold compared to oxide surfaces and makes it an ideal candidate for differential measurements. These results have been published elsewhere[58].

4.1 Introduction

In the following we cover SiNWFETs with a thin gold layer. Using a metal instead of an oxide surface enables new possibilities of surface chemistry to achieve selective sensing. Furthermore, the pH response is significantly reduced when using gold as surface material instead of Al_2O_3 or HfO_2. Due to competing surface reactions (as described in section 1.2.4) it is a requirement to lower the pH response as far as possible to increase the selective detection of other species than protons. We functionalize one half of a sample with SAMs of sodium selective crown ethers whereas the other half remains untreated. Thereby, we obtain two groups of SiNWs with different surfaces: Gold-coated NWs functionalized by the SAM (active NWs) and non-functionalized SiNWs with just a bare gold surface (control NWs). We demonstrate specific sodium ion sensing in a differential measurement. Measuring an active NW against a control NW leads to a response of $\approx -44\,$mV/dec NaCl in the biologically relevant concentration range of $1-1000\,$mM. We find that the clean gold surface shows a response to protons and changes in the background ion concentration. We explain this behaviour by the formation of gold oxide at the gold film surface[101–103] and its reaction with protons and chloride ions (Cl^-)[50,51]. Interestingly we find that the thiol-gold bonds of the SAM do not affect the number of oxidized gold atoms, thereby leaving the response of functionalized gold to pH and Cl^- unchanged. This is contrary to the behaviour of oxide coated devices where the functionalization does affect the pH response of the device[50]. Thanks to this special property of the gold surface it is possible to compare active and control NWs directly, as realized by the proposed differential measurement.

4.2 Results and Discussion

The samples were fabricated using the process described in chapter 2. For the gold-coated NWs a 5 nm chromium adhesion layer and a 20 nm gold film was evaporated onto the Al_2O_3 dielectric layer. The SEM micrograph in Fig. 4.1 a shows the lateral dimensions of the gold film, highlighted by the dashed line, with respect to a NW. The gold area was lithographically defined and overlaps the NWs in length and width. Fig. 4.1 b shows the schematics of the cross section of a device and Fig. 4.1 c shows a sketch of the measurement setup.

Fig. 4.1 d shows the conductance G *vs.* the liquid potential V_{ref} of a nanowire with a 20 nm thick gold film on top. With increasing pH the transfer curve shifts to the right. To quantify the shift we define the threshold

voltage V_{th} at a fixed conductance value of 20 nS (indicated by the arrow). The inset shows the pH response of nanowires with different surface materials. Compared to Al_2O_3 surfaces, gold also shows a linear response but with a significantly smaller slope of ≈ 38 mV/pH. Furthermore, gold-coated NWs show a response to the ionic strength when measuring in NaCl and KCl solutions, similar to Al_2O_3 and HfO_2. As described in section 3.4 and reference [51], we attribute this effect to the adsorption of chloride ions at the nanowire surface. No significant change of the response to protons and Cl^- has been observed over time. Even though gold is not expected to be corroded, the moderate response to protons indicates the formation of a gold-oxide layer [101–103]. With the site-binding model for protonation, deprotonation and Cl^- adsorption described in section 3.4 and references [50,51] we estimate the number of hydroxylated gold surface atoms to be only $\approx 1\%$. A detailed characterization of the gold surface and the estimation of the hydroxyl group density is given in section 4.3.

4.2.1 Sodium Sensing

Preparing self-assembled monolayers (SAM) of organic molecules at surfaces is an effective functionalization process for chemical sensing. Functional groups designed for trapping specific analytes can be immobilized close to the surface in this way. Crown ethers, consisting of a ring containing several ether groups, strongly bind cations due to the negatively polarized oxygen atoms. The selectivity to the type of ion can be controlled by varying the number of ether groups and the cavity diameter [104]. Here we used a Na^+ selective 15-crown-5 functionalized with a dithiolane anchoring moeity (Fig. 4.2 d). The samples were cleaned in oxygen plasma and closed with a PDMS microchannel. The samples were divided in two (active and control) parts by individual channels in the PDMS. The wires in the active channel were then functionalized with the 15-crown-5. This results in a differential setup having both, SiNWs with functionalized gold surface (active NWs) and bare gold-coated SiNWs (control NWs), on the same chip.

Fig. 4.2 a shows the response of an active and a control NW to NaCl. For the control NW, we find a positive shift in V_{th} with increasing salt concentration due to adsorption of Cl^- on the gold surface. The immobilization of the 15-crown-5 changes this response: Instead of the positive shift, a slightly negative shift is observed for the active NW, indicating adsorption of positive charges on the surface. The differential signal ($\Delta V_{th} = V_{th,\,active} - V_{th,\,control}$) shown in Fig. 4.2 e shows a response to NaCl of ≈ -44 mV/dec. Control measurements with KCl in Fig. 4.2 b show no difference between bare and functionalized gold, suggesting a high selectivity of the 15-crown-5 towards Na^+
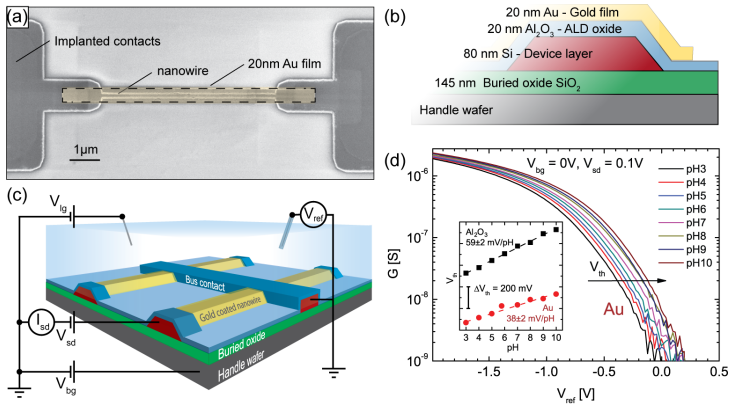
Figure 4.1: Device structure and measurement setup. (a) SEM micrograph of a 150 nm wide silicon nanowire coated with a 20 nm thick Al_2O_3 dielectric (by atomic layer deposition, ALD). NWs are lithographically defined in silicon on insulator wafers. 5 nm chromium as adhesion layer and 20 nm gold are deposited on top of the nanowire by electron beam evaporation. Contact regions are highly p-doped. (b) Schematics of a nanowire cross-section with the gold film covering the NWs. (c) Schematics of the measurement setup. A source meter is used to apply a source-drain voltage V_{sd} and to measure the source-drain current I_{sd}. Using a switching box, up to 48 NWs can be measured on one sample. The back-gate voltage V_{bg} is applied to the wafer substrate. The liquid-gate voltage V_{lg} is applied by a platinum wire immersed into the electrolyte. The liquid potential V_{ref} is measured by a calomel reference electrode. (d) Conductance curves G vs. V_{ref} of a 250 nm wide gold-coated Si-NW in different pH buffer solutions. The transfer curves shift to the right with increasing pH. The threshold voltage V_{th} is defined in the subthreshold regime at a constant conductance value of $20\,\mu S$ (arrow). Inset: V_{th} at different pH for Al_2O_3 (59.5 mV/pH) and Au (38 mV/pH). Figures adapted from reference [58].

and none for K^+. In the case of pH response (Fig. 4.2 c) the two different sur-
faces behave the same way. The differential signal (ΔV_{th}) in Fig. 4.2 e empha-
sizes that only a change in Na^+ concentration induces a different response of
the two surfaces. Thus a good Na^+ sensor with high response and specificity
was realized. Further it indicates that protonation and deprotonation of sur-
face hydroxyl groups, as well as their interaction with Cl^- is unaffected by
the self-assembly of the crown ethers. In Fig. 4.2 d we propose a functional-
ization scheme where the sulfur-gold binding only happens at non-oxidized
gold atoms ($\approx 99\%$ of the surface), leaving the number of hydroxyl groups
unchanged [102]. It is our picture that the crown ether functionalization adds
a third type of surface reaction to the system, without affecting the number
of hydroxyl groups and their interaction with the electrolyte. Thus, the re-
sponse of 15-crown-5 is a superposition of the positive shift coming from
Cl^- adsorption at -OH_2^+ sites and Na^+ reacting with the crown ether. Sub-
tracting the signal of a control gold-coated NW from an active NW (ΔV_{th})
reveals the response of the crown ether.

4.3 Methods

Surface Functionalization   For immobilization of thiol terminated 15-
crown-5 half of the SiNWs on a sensor chip were covered with 5 nm
chromium as adhesion layer and 20 nm gold by e-beam evaporation. The
samples were cleaned in O_2 plasma (Oxford Plasmalab 80 plus, 30 W, 45 s)
and covered with a PDMS microchannel. The 15-crown-5 molecule, synthe-
sized by Iain A. Wright from the Edwin C. Costable group at the depart-
ment of chemistry, *University of Basel* was dissolved in ethanol (≈ 2 mM).
The SAMs were obtained by pumping the solution through the (active) mi-
crochannels with long stabilization intervals for 16 h. After the functional-
ization the channels were rinsed with ethanol and deionized water.

Characterization of the Gold Surface   Fig. 4.3 shows the response of a
gold-coated SiNW to changes in pH and NaCl. The vertical axis shows the
shift in threshold voltage (ΔV_{th}). This corresponds to the difference in sur-
face potential ($-\Delta\Psi$) since a p-type semiconductor was used. To quantify
the number of hydroxyl groups of the gold oxide we use the full site-binding
model described in section 1.1.3 and the model for anion adsorption by pos-
itively charged hydroxyl groups described in section 3.4.

The following expressions describe the reactions at the gold surface. Due
to the amphoteric character of the OH surface groups of the metal oxide
surface, two reaction constants for deprotonation (K_a) and protonation (K_b)
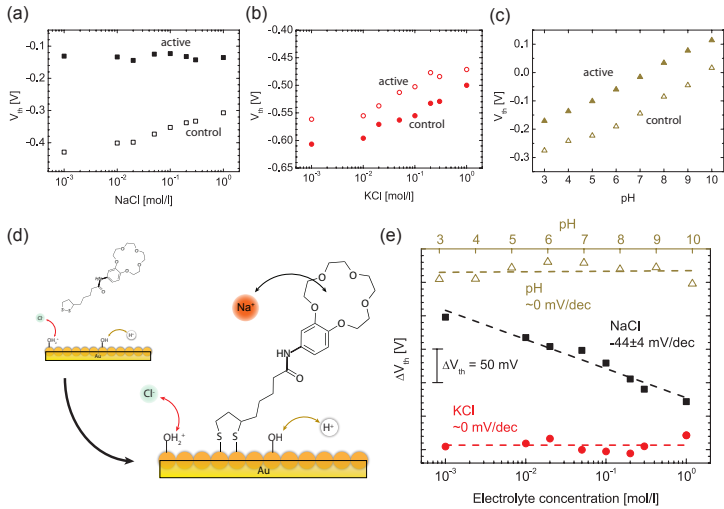
Figure 4.2: Surface functionalization with 15-crown-5 for Na$^+$ sensing. (a-c) V_{th} for a 1 μm wide functionalized (active) and 400 nm wide bare gold (control) NWs against c[NaCl] (a), c[KCl] (b) and pH (c). The response to NaCl changes with crown ether functionalization, whereas no difference between active and control NWs is seen when measuring in KCl and pH buffer solutions. (d) Immobilization reaction scheme of the sodium selective crown ether on gold. We propose that the thiol only reacts with (reduced) gold atoms, leaving the number of hydroxyl groups unchanged. (e) Differential threshold voltage (ΔV_{th}) of gold-coated NWs (active 15-crown-5 - control gold) $vs.$ the electrolyte concentration and pH. The crown ether shows high selectivity towards Na$^+$. Figures adapted from reference [58].

are needed. A third reaction constant (K_c') describes the Cl^- adsorption.

$$MeOH \rightleftharpoons MeO^- + H_s^+, \ K_a = \frac{v_{MeO^-} \cdot a_{H_s^+}}{v_{MeOH}} \tag{4.1}$$

$$MeOH_2^+ \rightleftharpoons MeOH + H_s^+, \ K_b = \frac{v_{MeOH} \cdot a_{H_s^+}}{v_{MeOH_2^+}} \tag{4.2}$$

$$MeOH_2^+ + Cl_s^- \rightleftharpoons MeOHCl^- + H_b^+, \ K_c' = \frac{v_{MeOHCl^-} \cdot a_{H_b^+}}{v_{MeOH_2^+} \cdot a_{Cl_s^-}} \tag{4.3}$$
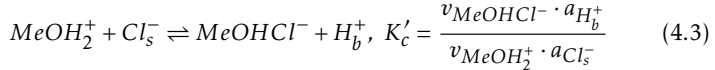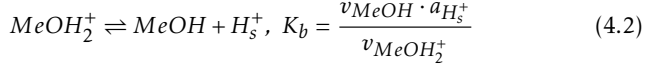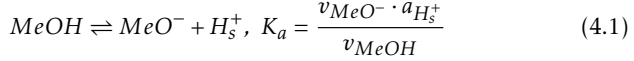
Indices s and b denote surface and bulk. $a_{H_s^+}$ is the activity of the surface protons and v is the number of sites per m^2 for one particular species. The total number of sites per m^2 is

$$N_s = v_{MeOH} + v_{MeO^-} + v_{MeOH_2^+} + v_{MeOHCl^-} \tag{4.4}$$

The resulting surface charge density σ_0 is screened by the double layer capacitance per m^2 C_{dl} leading to the surface potential drop Ψ

$$\Psi = \frac{\sigma_0}{C_{dl}}, \ \sigma_0 = e(v_{MeOH_2^+} - v_{MeO^-} - v_{MeOHCl^-}) \tag{4.5}$$

The parameters were set as follows: $K_a = K_b = 10^{-7}$, $C_{dl} = 0.16\,\text{F/m}^2$ according to [50,51]. Protonation and deprotonation are equally probable ($K_a = K_b$). Otherwise a double s-shaped response would be expected, as exemplified in [50]. C_{dl} can be taken as a fixed value since it is dominated by the Stern layer capacitance which is independent of the ionic strength. Fitting the response of gold to pH and ionic strength with our combined site-binding model for Cl^- adsorption (red lines in Fig. 4.3) results in an estimated surface hydroxyl group density $N_s = 1.5 \cdot 10^{17}\,\text{m}^{-2}$ and a reaction constant $K_c' \approx 2 \cdot 10^{-5}$. Here N_s is ≈ 60 times smaller for Au than for Al_2O_3. Although only few gold surface atoms ($\approx 1\%$) are oxidized, the s-shaped response to pH with a linear behaviour between pH 4 and pH 8 of $\approx 40\,\text{mV/pH}$ is well described by this site-binding model. K_c' is roughly seven times larger than the value found for Al_2O_3 and HfO_2 [51]. This affects the response to Cl^-, where the threshold of the linear region is shifted to lower electrolyte concentration.

4.4 Conclusion

In conclusion we demonstrate a selective cation sensing by the self-assembly of Na^+-selective crown ethers on gold-coated NWs. In a differential measurement with active and control NWs on the same chip, a response of
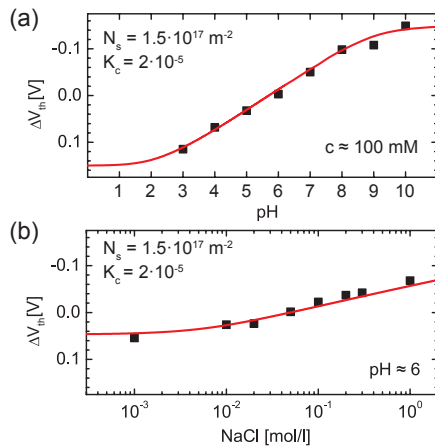
Figure 4.3: Response to pH and ionic strength of a gold-coated SiNW (solid squares) fitted with a combined site-binding model for protonation, deprotonation and Cl^- adsorption (red lines). (a) Change in threshold voltage ΔV_{th} *vs.* pH of a 250 nm wide wire. From the pH response the number of active hydroxyl groups N_s is estimated to be $1.5 \cdot 10^{17} \, m^{-2}$ which is a factor 60 less than for a Al_2O_3 surface. (b) ΔV_{th} *vs.* c[NaCl] for a 300 nm wide wire. Although the number of hydroxyl groups on gold is significantly lower than on Al_2O_3, a pronounced response to Cl^- is still observed for gold. Taking the obtained N_s to fit our chloride adsorption model to the response of gold to NaCl yields a reaction constant for Cl^- adsorption $K_c = 2 \cdot 10^{-5}$. Figure adapted from reference [58].

≈ -44 mV/dec in the concentration range of 1 mM up to 1 M was achieved. The response to NaCl is more than an order of magnitude larger than for KCl, indicating good selectivity. We showed that gold surfaces are slightly sensitive to changes in proton and Cl^- concentration. Both effects indicate the small density of hydroxyl groups at the gold surface. We infer from our measurements that the thiol-gold binding during the SAM formation happens only at non-oxidized gold atoms, leaving the number of hydroxyl groups unchanged. As a consequence, the thiol functionalization of gold does not affect the pH sensitivity and the response to Cl^-.

Our results underline the importance of monitoring the changes in pH and ionic strength simultaneously for specific ion-detection experiments. It enables the distinction of the signal caused by the target analyte and the contributions of the background electrolyte. In this work, this is realized by the differential measurement setup using the non-functionalized control gold surface as a proton and chloride sensitive reference electrode. However, the influence of the background electrolyte only cancels out in the differential signal, if the functionalization does not change the response to any analyte except the targeted one. In this respect, the gold surface appears to be an ideal candidate.

5

Real-Time Detection of Protein Interactions with Gold-Coated SiNW Biosensors

Detection and quantification of biological and chemical species are central to many areas of healthcare and research in life sciences, ranging from diagnosing diseases to discovery and screening of new drug molecules. Monitoring the binding affinities and kinetics of protein interactions is crucial in drug research. Such information is the key to identify their roles in cellular function. A real-time transduction of molecular interactions by a sensing device reveals the information on binding affinities [105] and offers a useful tool for disease diagnosis [106], genetic screening [18] and drug discovery [16]. The search for new therapeutic candidates often requires screening of various candidates. At present, the state of the art is surface plasmon resonance (SPR), such as *Biacore (GE Healthcare)* [107]. However, this technique is limited by low throughput analysis and is cost-intensive since it is based on optical components. It has been shown that SiNW FETs can be used as biosensors to measure protein-ligand interactions. The direct transduction of the analyte-surface interaction into an electrical signal allows real-time and high-throughput detection of biomolecules. Attaching the interaction partner, the so-called ligand directly on the sensor surface allows highly specific dection without the requirement for any labels [108,109]. In the past, it has been demonstrated that SiNW FET biosensors can detect biomolecular interactions down to picomolar concentrations [2,13,109]. However, most of this research has been focused on reducing the limit of detection. So far, studies on quantifying the signals - specifically the binding affinities and kinetic data

- have primarily been done on DNA interaction [110] and biotin-streptavidin interactions [16]. However, the biotin-streptavidin binding is well-known and is one of the strongest non-covalent interactions known in nature (its dissociation constant K_D is on the order of $\approx 10^{-14}$ M) [111]. Hence, its significance for interaction studies and benchmark for minimum LOD is questionable.

In this chapter we demonstrate the real-time detection of a physiologically relevant protein with gold-coated SiNWs. Clear concentration dependent signals were obtained upon protein injection. The simultaneous measurement of several SiNWs in active and control arrays increased the amount of data and allowed the comparison of different sensor dimensions. Our results are an important step towards kinetic studies of protein-ligand binding.

5.1 FimH Lectin-Sugar Interaction

For our biosensing experiments we have chosen the physiologically relevant FimH lectin as analyte. Lectins are highly specific sugar binding proteins which play a key role in bacterial infectious diseases such as respiratory tract infections and urinary tract infections. FimH is terminally expressed on type 1 pili of uropathogenic *Escherichia coli*, which is the main cause of urinary tract infections. It enables bacterial adhesion to epithelial cells, the initial step of infection [112]. The molecular pharmacy group of Prof. Beat Ernst at the *Pharmacenter (University of Basel)* designed and evaluated high affinity mannosides for the carbohydrate-binding protein. Derivatives that antagonize FimH are promising therapeutic agents for the treatment of urinary tract infections. A crucial factor for the efficacy of a therapeutic agent is the half-life of the drug-receptor complex. Therefore, kinetics of the binding process and equilibrium dissociation constants are of special interest. Nanowire-based sensors are potential candidates to compete with SPR, which is widely applied to study these parameters. The possibility for high integration and up-scaling would speed up the screening of antagonists for the development of anti-infective drugs.

5.2 Binding Kinetics

The signal upon binding of analyte molecules in solution to an immobilized ligand on the sensor surface depends on mass transport of the analyte to the reaction site and on the affinity of the analyte-ligand system. From the time-dependent signal, the association (k_a), dissociation (k_d), and equilibrium dissociation (K_D) constants can be derived. This information is valuable for biomolecular interaction studies in many applications.
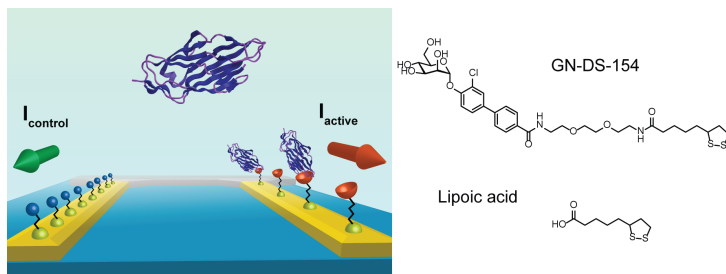
Figure 5.1: Sketch of FimH adsorption on gold-coated silicon nanowires with immobilized mannose linker (GN-DS-154). The control wires are functionalized with lipoic acid.

The most commonly used model is the Langmuir, which describes a 1:1 interaction where one analyte molecule interacts with one ligand molecule. It assumes that the binding is equivalent and independent for all binding sites. Further, the reaction is not limited by mass transport (k_a is small compared to the diffusion of the analyte from the bulk phase to the sensor surface)[113]. The basic equation for a conjugation between an analyte-receptor pair can be written as follows:

$$A + B \underset{k_d}{\overset{k_a}{\rightleftharpoons}} AB \qquad (5.1)$$

with A being the analyte and B the ligand. AB denotes the bound analyte-ligand pairs. The equilibrium dissociation constant K_D [M] is defined as:

$$K_D = \frac{[A][B]}{[AB]} = \frac{k_d}{k_a} \qquad (5.2)$$

The brackets denote the corresponding concentrations in mol/l. K_D indicates the strength of the binding energy between analyte and linker. A higher K_D means a weaker interaction. The association (k_a [M^{-1}s^{-1}]) and dissociation (k_b [s^{-1}]) constants are related to each other by the differential equation:

$$\frac{d[AB]_t}{dt} = k_a \cdot [A] \cdot ([B]_0 - [AB]_t) - k_d \cdot [AB]_t \qquad (5.3)$$

where $[AB]_t$ is the number of bound analyte molecules per unit area and $[B]_0$ is the areal density of linker molecules. For a sensor, the response signal

$R(t)$ is assumed to be proportional to the concentration of bound analytes ($R(t) \propto [AB]_t$) and the maximum response $R_{max} \propto [B]_0$ where all the ligand sites on the surface are occupied. During the association phase the analyte in the solution is present at a constant concentration. The sensor signal as a function of time can be written as follows:

$$R(t) = \frac{[A] \cdot k_a \cdot R_{max}}{[A] \cdot k_a + k_d}(1 - e^{-([A] \cdot k_a + k_d) \cdot t}) \qquad (5.4)$$

Assuming that during the dissociation phase no analyte is present in the solution ($[A] = 0$), hence, Eq. 5.3 can be solved by the exponential decay

$$R(t) = R_0 \cdot e^{-k_d \cdot t} \qquad (5.5)$$

with R_0 being the signal level at the end of association.

Fig. 5.2 a shows the association and dissociation following Langmuir 1:1 kinetics for a system with $K_D = 10 \, \text{nM}$ and an analyte concentration of 100 nM. Although the affinity is the same, the kinetics strongly depends on the rate constants k_a and k_d. Fig. 5.2 b shows how the analyte concentration (relative to K_D) affects the response.
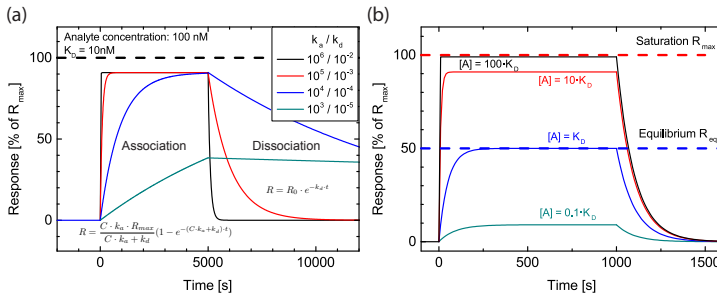
Figure 5.2: Theoretical plots of the Lagmuir 1:1 adsorption model. (a) Response in percentage of R_{max} (all ligand sites occupied) *vs.* time for a analyte-ligand interaction with $K_D = 10 \, \text{nM}$. Different kinetics can result in the same affinity. (b) Response for $k_a = 10^6 \, \text{M}^{-1}\text{s}^{-1}$, $k_d = 10^{-2} \, \text{s}^{-1}$ at different analyte concentration. The occupancy at equilibrium depends on the bulk analyte concentration relative to K_D.

In equilibrium $d[AB]/dt = 0$, the ratio of occupied ligands is given by:

$$\frac{[AB]_{eq}}{[B]_0} = \frac{[A]}{K_D + [A]} \qquad (5.6)$$

Hence, the K_D determines the occupancy of the ligand sites at a certain analyte bulk concentration. As exemplified in Fig. 5.3, the sensitive concentration range and the limit of detection depend on K_D of the analyte-ligand interaction.
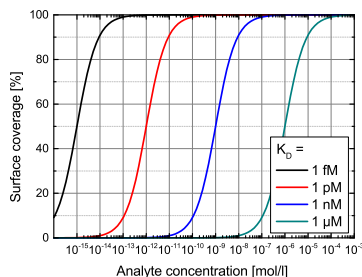
Figure 5.3: Theoretical plot of the surface coverage *vs.* analyte concentrations for different equilibrium dissociation constant (K_D) values.

5.2.1 Two-Compartment Model for Transport Limited Kinetics

In the case of strong binding affinity, the transport of the analyte to the reaction site starts to be a limiting factor. A typical model to describe this so-called transport limited regime is the two-compartment model[16,114]. If the association of proteins to the surface is faster than the diffusion of proteins to the proximity of the surface sites, a depletion zone will be formed, where the local concentration of the analyte is lower than in the bulk. In reverse, in the dissociation phase a retention zone is present close to the surface sites that allow dissociated analytes to rebind to empty surface sites. This additional two-compartment reaction can be described as follows:

$$A \underset{}{\overset{k_M}{\rightleftharpoons}} A_s + B \underset{k_d}{\overset{k_a}{\rightleftharpoons}} AB \tag{5.7}$$

where A_s denotes the analyte surface concentration and k_M the effective transport rate constant in $[M/s]$. The reaction rates for A_s and AB are defined as follows:

$$\frac{d[A]_s}{dt} = k_M([A]-[A]_s) - k_a[A]_s([B]_0-[AB]) + k_d[AB] \tag{5.8}$$

$$\frac{d[AB]}{dt} = k_a[A]_s([B]_0 - [AB]) - k_d[AB] \tag{5.9}$$

Appendix C shows a model system where the influence of k_M and $[B]_0$ is illustrated.

5.3 Methods and Materials

5.3.1 Linker Immobilization

The sensor surface was cleaned in UV-ozone for 20 min and enclosed by the PDMS microchannel, separating the chip in active and control channels. The channels are then rinsed with ethanol for ≈ 30 min.

The active linker, synthesized by Giulio Navarra from Prof. Beat Ernst's group (molecular pharmacy, *University of Basel*), was dissolved in ethanol (2 mM). The control channel was treated with lipoic acid dissolved in ethanol (2 mM) (see Fig. 5.1). The microchannels were flushed with 200 μl of the respective solution, then 200 μl were slowly injected over ≈ 15 h using a syringe pump. After the functionalization, the channels were washed with ethanol before the PDMS microchannel was removed for the measurement.

5.3.2 Protein and Buffer solution

The protein solutions were provided by the molecular pharmacy group. FimH-CRD-Th-6His[115] has a molecular weight of 18.6 kDa. Concentrations from 1 μg/ml up to 50 μg/ml (54 nM - 2.7 μM) were used. 10 mM HEPES at pH 8 was used as buffer solution. HEPES (4-(2-hydroxyethyl)-1-piperazineethanesulfonic acid) is a zwitterionic organic chemical buffering agent which is widely used. A long Debye length is preferred for the detection of large molecules. An intermediate ionic strength was chosen to have a well buffered solution and a Debye length of > 3 nM. The theoretical isoelectric point of the FimH protein is at pH 6.7, so the protein is negatively charged in pH 8 buffer solution.

5.3.3 Sensing Mechanism and Device Calibration

In order to obtain the kinetics of the analyte-ligand binding, time dependent measurements were performed. The SiNWs were operated in the linear regime (by applying a constant negative voltage to the reference electrode) while I_{sd} was recorded. At constant flow (≈ 26 μl/min), the buffer solution was pulled through the liquid cell. FimH at different concentrations was injected by changing the switching valve.

Changes in surface potential shift the threshold voltage (ΔV_{th}) which changes I_{sd}. The relation is given by the transconductance g_m according to

$$-\Delta\Psi_0 = \Delta V_{th} = \frac{\Delta I_{sd}}{g_m} = \frac{q_A}{C_0}[B]_0 \times \frac{[A]}{K_D + [A]}. \qquad (5.10)$$

Here q_A is the electric charge given by an adsorbed analyte and C_0 is the capacitive coupling (in $[F/m^2]$) between the charge of the analyte molecule within the double layer and the bulk solution. It is influenced by the double layer capacitance and hence dependent on the ionic strength of the buffer. g_m was determined through I_{sd}-V_{ref} measurements of each SiNW [16]. Using this conversion the signal is no longer a function of the FET performance and only depends on $\Delta\Psi_0$ induced by the analyte.

5.3.4 Surface Regeneration

Regeneration is the process of removing bound analyte from the sensor surface after a measurement to prepare the next analysis cycle. Ideally regeneration removes analyte from the ligand without changing the ligand density or activity. Efficient regeneration is important for the lifetime of the sensor. Incomplete regeneration or loss of the surface binding activity lowers the density of free linker sites and, hence, the maximum signal range.

Regeneration was accomplished by denaturing the structure of the analyte. Usually strong bases or acids as well as detergents are used to denature proteins. However, since pH also affects the surface potential of the gold-coated nanowires, we chose concentrated urea (6 M) as regeneration solution, since pH was similar to the running buffer.

5.4 Results and Discussion

Fig. 5.4 a presents the real-time sensor response of five different SiNWs of the same array to 20 µg/ml FimH. The measured ΔI_{sd} has been normalized by $\Delta I_{sd}/g_m$ to obtain the change in surface potential. The response among the different wires is very similar, although the individual drifts do not correspond. The total response based on association is ≈ 20 mV. No equilibrium state was visible after 10 min of FimH injection. After switching back to running buffer, a clear decrease in signal was observed. However, the signal seems to saturate above the original baseline, which indicates that no complete dissociation of FimH proteins occurs. Surface regeneration with 6 M

urea strongly affects the surface potential due to the high concentration and slight variation in pH.

Fig. 5.4 b shows the response of a SiNW for three different FimH concentrations. $10 \mu g/ml$, $20 \mu g/ml$ and $50 \mu g/ml$ were used, which corresponds to $\approx 0.55 \mu M$, $1.1 \mu M$ and $2.75 \mu M$. A straight line, taken from the 400 s prior to the binding event, was subtracted from the data to take out the drift and set the baseline to zero. Time= 0 is defined as the onset of FimH adsorption, which occured 40 s after switching the valve. The response to FimH is clearly concentration dependent. During adsorption a pronounced kink is visible. A possible explanation for the change in kinetic is mass transport limitation, which occurs if the association rate is faster as the diffusion of the proteins to the ligand sites. Such phenomena occur if the ligand density on the surface is extremely high or the solution flow rate is too low. The change to running buffer is indicated by the dashed lines. The dissociation is similar for all the concentrations.

A different measurement is shown in Fig. 5.4 c and d. The two figures compare the response for a $1 \mu m$ and a $25 \mu m$ wide SiNW. Here the kink in the adsorption is less pronounced. Also the dissociation was not the same for the different concentrations, which can be associated with a change in baseline drift. The dashed lines in Fig. 5.4 c show the response of a control SiNW functionalized with lipoic acid. No protein interaction was observed, indicating an absence of nonspecific binding to the control wires. For SiNWs of different widths the response was of the same strength. However, the signal-to-noise ratio is better for the lager sensor surface, as predicted by the noise analysis measurements in section 3.2. Fig. 3.6 (in the previous section 3.2) shows the RMS noise for the baseline in Fig. 5.4 c and d. Taking these values a SNR of more than 600 was achieved for the $25 \mu m$ wide SiNWs. Surface contaminations or moving air bubbles in the liquid cell can disturb the gating and induce additional noise. This was observed for the $10 \mu g/ml$ signal in Fig. 5.4 d, where kind of two level fluctuations occur and vanish over time.

5.4.1 FimH Adsorption Kinetics

The clear signals from FimH adsorption allow the investigation of the binding kinetics. To compare and validate our signals, similar measurements were performed in a commercial Biacore system. The Biacore chip functionalization had to be done slightly differently. A sensor chip with bare gold surface was used. A monolayer of 16-Mercaptohexadecanoic acid (MHDA, 2 mM in Ethanol over night) was used as surface linker. In a second step the ligand was immobilized by amine coupling in borate buffer at pH 8.5. We
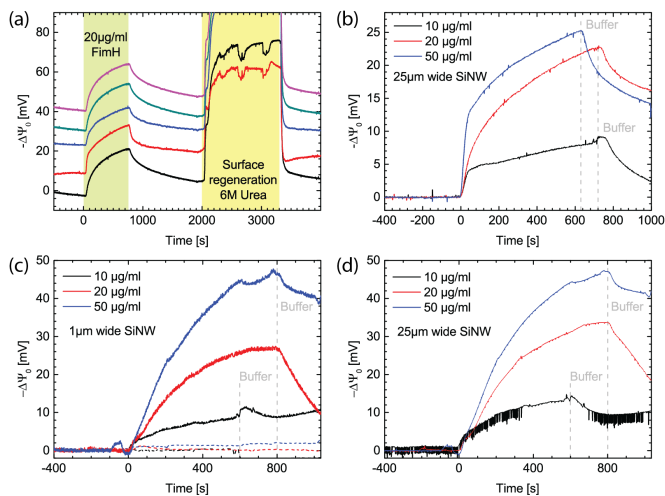
Figure 5.4: Measurements of FimH-ligand binding on gold-coated SiNWs. (a) Real-time sensor response ($\Delta\Psi_0 = I_{sd}/g_m$) for five different SiNWs of the same array upon injection of $20\,\mu g/ml$ FimH, running buffer and surface regeneration (indicated by background color). (b) Response of a $25\,\mu m$ wide SiNW for different FimH concentrations. A straight line, defined from the $400\,s$ prior to the binding event, was subtracted to take out the drift and set the baseline to zero. The time at which the protein injection is stopped is indicated by the grey dashed line. In a different measurement (c,d) the response of neighbouring SiNW of different width for three FimH concentrations is compared. The response is similar, but the signal-to-noise ratio is clearly increased for the larger sensor area. The dashed lines in (c) show the response of the control gold-coated SiNW. No protein interaction is observed for the lipoic acid functionalized SiNWs.

expect that the ligand density on the Biacore chip is lower as compared to the SiNW surface due to the two step surface functionalization. Further, the space between the linkers is different. Whereas we expect the Biacore chip to be covered with a densely packed monolayer of MHDA, the linkers on the SiNWs are surrounded by gold. Fig. 5.5 compares the kinetics from the two different measurement systems. Since the same ligand was used, similar kinetics was expected. However, some clear differences were observed.

Fig. 5.5 a shows the real time SiNW sensor response for 50 μg/ml FimH. The data was fitted using the two-compartment model (Eq. 5.8 and 5.9). Including the mass transport limitation the association can be fitted reasonably well. Hence, the kink in the association could be attributed to a limited mass transport. With $k_a = 10^4 \, \mathrm{M}^{-1}\mathrm{s}^{-1}$, $k_d = 4 \cdot 10^{-2} \, \mathrm{s}^{-1}$, $k_M = 5 \cdot 10^{-3} \, \mathrm{s}^{-1}$ and $[B]_0 = 6 \cdot 10^{18} \, \mathrm{m}^{-2}$ we find a binding equilibrium constant of $K_D = 4 \, \mu$M. However, the model cannot explain the dissociation adequately. The initial fast dissociation indicates more complex binding kinetics or an additional signal from nonspecific binding. Fig. 5.5 b shows the Biacore data and the corresponding fits. The reference data from the control channels has been automatically subtracted. The association time scale is comparable to the SiNW measurement. At 600 s the protein injection was stopped and the signal did not saturate at the given concentrations. No kink is visible, which can be explained by the lower ligand density and the more sophisticated liquid delivery system as compared to our system. However, after 600 s the signal is almost flat, indicating an extremely low dissociation rate. Since no equilibrium was reached, K_D can not be determined exactly. Nevertheless, the fits to the Biacore measurement indicate an equilibrium constant in the low nanomolar range.

The discrepancy between the two different measurement methods could have various explanations. First, the sensing mechanism is not the same. While the SiNWs sense charges localized within a few nm from the surface, Biacore is based on surface plasmon resonance which measures the change in resonance frequency upon mass adsorption to the surface. The dept of the evanescent wave is roughly two orders of magnitude larger as the debye length, which results in a different sensitivity on analyte distance to the surface. Conformation changes of the adsorbed proteins and ligands due to mutual interactions could lead to different signals. Second, the different surface functionalization could have an effect on non-specific protein adsorption. In the case of the SiNW sensor no background signal was subtracted, since the control SiNWs showed no response. However, the control surface (SAM of lipoic acid) is negatively charged at pH 8 and repulses the negatively charged proteins. In case of the active SiNWs the gold surface surrounding the lig-

ands is expected to be neutral (PZC ≈pH 8), so nonspecific adsorption of proteins on the gold surface is likely to occur along with the protein linker interaction. This would lead to a superposition of two signals with different kinetics, which makes it impossible to extract the true rate and equilibrium constants. Research is ongoing to isolate and reduce non-specific binding by comparing different surface functionalizations with no or very low affinity to FimH.
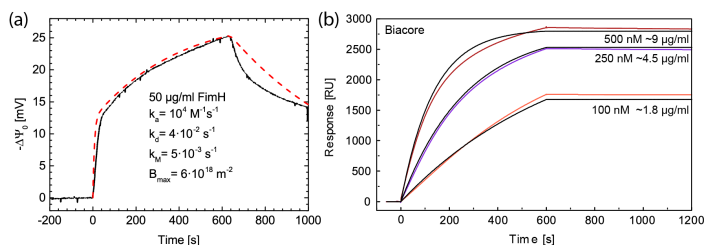
Figure 5.5: FimH binding kinetics. (a) The $50\,\mu g$/ml signal from Fig. 5.4 b fitted with the two-compartment model (dashed red line) with the following parameters: $k_a = 10^4\,\mathrm{M^{-1}s^{-1}}$, $k_d = 4\cdot10^{-2}\,\mathrm{s^{-1}}$, $k_M = 5\cdot10^{-3}\,\mathrm{s^{-1}}$ and $[B]_0 = 6\cdot10^{18}\,\mathrm{m^{-2}}$. (b)Biacore control measurement. A Biacore sensor chip Au (gold surface) was functionalized with the same ligand as it was used as in the nanowire experiment. However, the immobilization was done in a two step reaction (amine coupling to MHDA). The real-time response is given in response units (RU). At $600\,\mathrm{s}$ the protein injection was stopped. The fitted curves are shown in black.

5.4.2 Competing Surface Reactions

In section 1.2.4 we have seen that competing surface reactions of other species than the analyte can limit the sensitivity of the sensor. The competing adsorption reactions of the individual species are coupled via the surface potential. In our case of gold-coated BioFETs the response to pH affects the response to FimH proteins. Only due to a very low pH response we were able to detect clear signals from FimH adsorption.

Fig. 5.6 a shows the pH response for gold-coated SiNWs functionalized with the ligand with high affinity to FimH. Due to harsh surface treatments (cleaning and functionalization) in between different measurements, the gold film on the SiNW surface was altered. Thereby the pH response varied for the different measurements. Since the FimH measurements were performed at pH 8 we are interested in this pH range. The pH response (linear

fit from pH 5 to pH 10) varies from $\approx 19 - 29\,\text{mV/pH}$. With the extended site binding model where the FimH ligands are included (FimH concentration is set to $\approx 0\,\text{M}$) the pH response of the functionalized gold surface can be fitted to extract the density of hydroxyl groups (N_s). We find that N_s changed by roughly a factor of two.

Fig. 5.6 b compares the FimH response of the respective measurements. For the increased N_s the FimH response was clearly reduced. The data supports the model of competing surface reactions, which is shown in Fig. 5.6 c. It shows an example value for the response to FimH at a ligand density of $3 \cdot 10^{16}\,\text{m}^{-2}$ and $K_D = 333\,\text{nM}$ for two different N_s at pH 8. The curves denote the change in surface potential at equilibrium. With increasing N_s the response decreases. Simultaneously the sensitive concentration range becomes narrower. Fig. 5.6 b and c agree qualitatively. However, since no equilibrium was reached in the FimH measurements, the signal ratios cannot be compared accordingly. The bottom line is that the FimH signal increases for a low pH response. This holds for any ISFET system, where decreasing the number of surface sites of a competing reaction enhances the response to the targeted analyte.

5.5 Conclusion

We have successfully demonstrated the use of gold-coated SiNWs as biosensors by the detection of FimH, a physiologically relevant protein which plays a role in bacterial urinary tract infections. Real-time detection without labelling was achieved at a very high signal-to-noise ratio. The SNR is shown to increase with $\sqrt{\text{area}}$ (see section 3.2) which is an important aspect for the design of a biosensor with high device density. The use of gold as surface material has two tremendous advantages as compared to oxides. First, the pH response is strongly reduced which enables the detection of other species than protons. Second, surface functionalization of gold has been extensively investigated which simplifies the development of protocols for ligand immobilization on the sensor. Being able to observe association and dissociation enables the use of BioFETs as affinity sensors. However, the accurate determination of the protein binding affinity and kinetics was not possible when comparing the data with Biacore measurements. For this purpose further control measurements are needed to rule out superimposed signals (*e.g.* by nonspecific adsorption on gold).

There is significant room for improvement. On the one hand modifying the surface functionalization to minimize the mass transport limit and nonspecific adsorption. On the other hand, a more sophisticated liquid handling
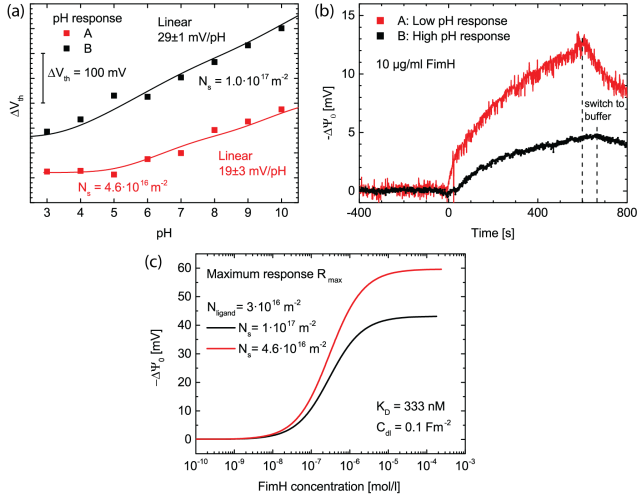
Figure 5.6: Competing surface reactions. (a) pH response (ΔV_{th} *vs.* pH) for gold-coated SiNWs functionalized with FimH ligands. The two different datasets show the same sample measured after different FimH measurement series. The lines correspond to the site binding model at different hydroxyl group density N_s ($pK_a = 9$, $pK_b = 7$). Depending on N_s the linear response around pH 8 varies from $\approx 19\,\text{mV/pH}$ to $29\,\text{mV/pH}$. (b) Real-time sensor response for $10\,\mu\text{g/ml}$ FimH. The curves correspond to the same functionalized SiNWs as shown in (a). The response to FimH is clearly increased by roughly a factor of two when N_s is low. However, the wire showed increased noise during this measurement. These voltage fluctuations were most probably induced by air bubbles. (c) Theoretical FimH response at equilibrium for various FimH concentrations based on the site binding model at two different hydroxyl group densities (N_s). On the basis of the pH and FimH measurement the following paramerters were chosen: $N_{\text{ligand}} = 3 \cdot 10^{16}\,\text{m}^{-2}$, $N_s = 1 \cdot 10^{17}\,\text{m}^{-2}$ and $4.6 \cdot 10^{16}\,\text{m}^{-2}$, $C_{dl} = 0.1\,\text{Fm}^{-2}$, $K_D = 333\,\text{nM}$ and pH= 8.

system would improve the reproducibility. Especially by replacing the flow cell with a microchannel system the flow speed and hence the mass transport increases drastically, while the total volume of the analyte solution can be reduced.

Based on these results we think that SiNW FETs have a great potential to be used in disease diagnosis and drug discovery. The large scale integration of SiNW arrays at low cost makes a good case for using biosensors based on silicon nanowires.

Additional Investigations

6.1 Selective Potassium Sensing with Oxide-coated SiNWFETs

In the last two chapters we demonstrated specific sensing of alkaline ions and proteins with gold-coated SiNWs. In addition, we also achieved potassium ion sensing on Al_2O_3 and HfO_2 surfaces using two different approaches: In the first place, a non-covalent surface modification where the SiNWs are covered by a water permeable membrane with embedded ion traps. Second, silanization of the oxide surface and the subsequent attachment of a crown ether.

Al_2O_3 and HfO_2 surfaces usually show a high response to pH, which competes with the signal from the targeted species (see section 1.2.4). Though, at reduced pH response ($\leq 40\,mV/pH$) detection of other species than protons is possible, as shown in the following section. Using silanes as surface modification, the number of surface hydroxyl groups gets reduced. However, this is not the case when using membranes. The following example shows a sensor with a reduced pH response (see Fig. 6.2 c, $\approx 40\,mV/pH$), which was probably due to etching of the Al_2O_3 surface at basic conditions.

6.1.1 Potassium Ion-Selective Membranes

To get a non-covalent surface modification, we functionalized Al_2O_3-coated SiNWs with Valinomycin ionophores embedded in a polyvinyl chloride (PVC) membrane to achieve a specific potassium ion (K+) sensing. We demonstrate a response of $\approx 38\,mV/decade$ for increasing KCl concentration. Having both functionalized and uncovered SiNWs (control) on the

same sample allows us to monitor the contribution of the background electrolyte. Thereby, we can extract the signal caused by the targeted potassium ion. Control measurements with $MgCl_2$ and pH demonstrate the selectivity of the ionophore. These results have been published in reference [116].

Surface Functionalization

For the PVC membranes a mixture of Valinomycin (1.3%), polyvinyl chloride (PVC, 30.4%) and Bis(1-butylpentyl) adipate (BBPA, 68.3%) was dissolved in cyclohexanone (50%) and tetrahydrofuran (THF, 50m%). All chemicals were purchased at Fluka. This mixture was deposited on individual NW arrays of UV/ozone treated samples (20min) by microdrop functionalization with a hamilton syringe ($\approx 0.2\,\mu$l). The membranes were then cured for 24h at 50°C. As highlighted in Fig. 6.1 a, only two of the four arrays of NWs were covered by the membrane. The two uncovered arrays were used as a control.
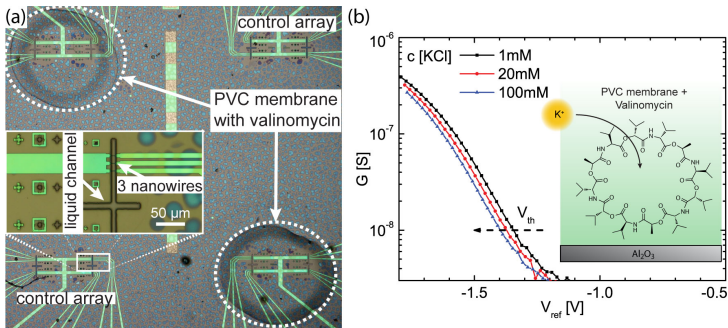
Figure 6.1: (a) Optical image of a sample with four arrays consisting of 12 NWs after functionalization. Two arrays were covered by PVC membranes with Valinomycin. The two other uncovered arrays contain NWs with bare Al_2O_3 surface used for control measurements. Inset: Zoom of a control array revealing three NWs and the aligned liquid channel on top of the wires. (b) Conductance G vs. V_{ref} for a NW covered by the PVC with Valinomycin. The curves shift to the left for increasing salt concentration. Inset: Schematics of Valinomycin embedded in a PVC membrane on a NW. Figure adapted from reference [116]

Results and Discussion

By micro-drop functionalization of single SiNW arrays with the ionophore embedded in the PVC membrane, the SiNWs become sensitive to potas-

sium ions (K^+). Fig. 6.1 b shows the subthreshold conductance G of a Valinomycin-coated NW against the liquid potential $V_{ref}$ in KCl electrolyte solutions with different concentrations. The transfer curve shifts to the left with increasing KCl concentration. Since the NW ISFETs are p-doped and operated in accumulation, the shift of the transfer curve to the left indicates adsorption of positive charges at the surface. To compare the functionalized SiNWs with the control SiNWs we use the threshold voltage V_{th} as a figure of merit. The threshold voltage is defined at a constant value of $G = 10\,\text{nS}$ as indicated by the black arrow in Fig. 6.1 b.

Fig. 6.2 a shows the shift in threshold voltage V_{th} with increasing KCl concentration for a Valinomycin-functionalized SiNW and a control SiNW. Solid squares correspond to Valinomycin coated SiNWs, which show a negative shift with increasing KCl concentration due to K^+ adsorption. Empty squares show the response of a SiNW with bare Al_2O_3 surface of the control array. We attribute the positive shift at concentrations above $10\,\text{mM}$ to unspecific chloride adsorption at the oxide surface (see section 3.4). To investigate the specificity of the ion-binding membrane in more detail, a control measurement with $MgCl_2$ solutions was done, shown in Fig. 6.2 b. Both Valinomycin coated wires (filled triangles) and control wires (empty triangles) show a positive shift in V_{th} with increasing $MgCl_2$ concentration, indicating adsorption of Cl^- according to the model described in section 3.4. This shows that the PVC membrane is permeable to Cl^- ions. Hence, the membrane does not passivate the oxide surface against the adsorption of chloride ions. A similar behavior is observed when repeating the measurement with different pH solutions (Fig. 6.2 c). Both surfaces respond in the same way, hence the ionophore PVC membrane is also permeable for protons. To obtain the response of the membrane we have to subtract the contribution of this two species from the measured signal. As a figure of merit, we therefore use the differential shift in threshold voltage $\Delta V_{th} = V_{th;\text{Valinomycin}} - V_{th;\text{control}}$ as shown in Fig. 6.2 d. A response of $-38\,\text{mV/decade}$ to a change in K^+ concentration is achieved. The differential threshold data for $MgCl_2$ in Fig, 6.2d emphasizes the insensitivity of Valinomycin to Mg^{2+}. Also, the second control measurement with varying pH confirms the high selectivity of the ionophore.

6.1.2 Covalent Surface Functionalization with Crown-Ethers

In a series of experiments, SiNWs with Al_2O_3 or HfO_2 surface were modified with a 18-crown-6 ether which is meant to be selective towards K^+ ions. To achieve covalent bonding, the oxide surface was activated by UV-
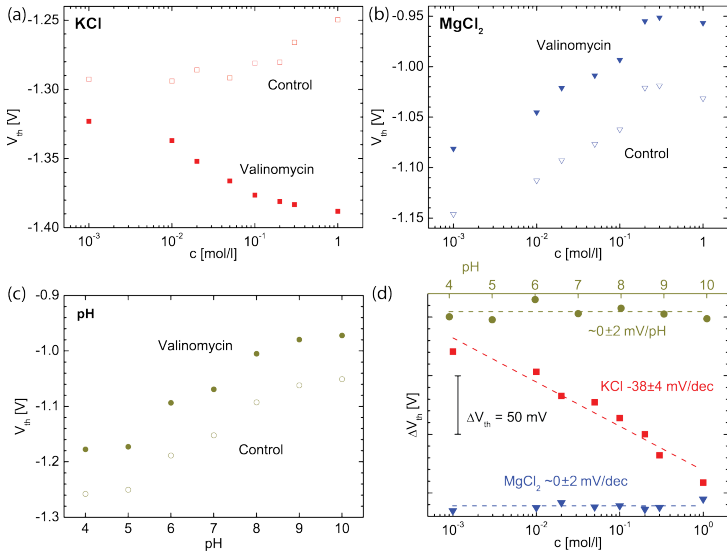
Figure 6.2: (a) V_{th} for a Valinomycin-functionalized NW and a control NW with bare oxide surface *vs.* increasing KCl concentration. While the control shows the characteristic shift towards positive V_{th} indicating anion adsorption, we observe an opposite behavior for the ionophore-covered NWs. (b,c) Control measurements for increasing MgCl$_2$ concentration and for solutions with increasing pH demonstrate the good selectivity of the ionophore towards K$^+$ ions. (d) Subtracting the signal of the control NW from the signal of the Valinomycin coated NW ($V_{th;\text{Valinomycin}} - V_{th;\text{control}}$) reveals the high response to KCl and no response to MgCl$_2$ and protons. Figure adapted from reference [116]

ozone and silanized with (3-Glycidoxypropyl)triethoxysilane (GOPS) by liquid phase deposition (Fig. 6.3 a). This results in a monolayer displaying epoxy moieties which allow the attachment of the amine terminated 18-crown-6 ether. Using a PDMS microchannel the samples were divided in active and control SiNWs, at which all SiNWs were silanized with GOPS and the 18-crown-6 ether was only on the active SiNWs. The samples were tested against KCl and NaCl solutions showing a good sensitivity towards K^+ ions (and only a weak response to Na^+ ions). Fig. 6.3 b shows $\Delta V_{th} = V_{th, \text{active oxide}} - V_{th, \text{control oxide}}$ of a sample with HfO_2 as dielectric material. The differential signal shows a linear response of $\approx -33\,\text{mV/dec}$ towards K^+ ions and almost no response to Na^+. It is known that the selectivity of crown ethers is limited. A weak affinity to several other types of alkaline ions is therefore not unexpected [117,118]. Due to the silanization the number of free surface hydroxyl groups and hence the pH response is reduced. Both active and control SiNWs show $\approx 38\,\text{mV/pH}$.
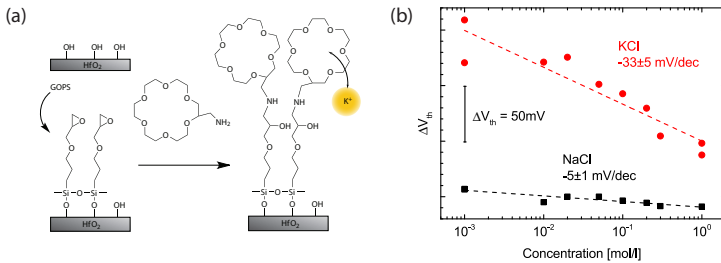
Figure 6.3: Surface functionalization for specific potassium ion sensing. (a) Immobilization reaction scheme. Silanization of a Al_2O_3 or HfO_2 surface with (3-Glycidoxypropyl)triethoxysilane (GOPS) as a first step. In a second reaction, the potassium selective crown ether 2-aminomethyl-18-crown-6 is immobilized by an epoxy-amine reaction in aqueous basic conditions. (b) Differential threshold voltage ΔV_{th} of HfO_2-coated SiNWs *vs.* electrolyte concentration. For KCl (circles) a response of $\approx -33\,\text{mV/dec}$ is observed, whereas for NaCl (squares) the response is $\approx -5\,\text{mV/dec}$.

6.1.3 Conclusion of Potassium Sensing

In conclusion, silicon nanowire field-effect transistors were modified for alkaline ions recognition. We show selective potassium ion sensing with high response of $30-40\,\text{mV/decade}$ in the concentration range of $1\,\text{mM}$ up to $1\,\text{M}$. The response for the target analyte is almost an order of magnitude larger

than for the control species. We find that the PVC membrane is permeable for chloride ions and protons. This means that the hydroxyl groups of the oxide surface can still interact with H^+ and Cl^- when measuring in KCl solution and influence the response of the sensor. Thanks to control SiNWs, we are able to subtract this background contribution to reveal the signal caused by the specific adsorption of potassium ions. The covalent attaching of crown ethers reduces the number of active surface hydroxyl groups. This has to be considered when using a differential measurement setup. However, by the self-assembly of GOPS on active and control SiNWs, the number of hydroxyl groups is reduced similarly.

This results show the potential of nanostructured ISFETs covered with membranes or covalently bound crown ethers for specific ion detection. Furthermore we demonstrate the importance of differential characterization.

6.2 Liquid Phase Surface Passivation

To passivate individual SiNW arrays on our sensor we tested liquid phase passivation of HfO_2-coated SiNWs. As described in section 3.3.1 we modified the surface by a SAM of octadecyldimethylmethoxysilane. Instead of vapor phase, we did liquid phase deposition of the silane molecule by drop-based functionalization. Therefore, the samples were cleaned in UV-ozone (20 min) and afterwards covered by a silane drop of $\approx 250\,\mu$l. To avoid evaporation of the silane, the sample was stored in a desiccator under N_2 atmosphere with a reservoir of exessive silane inside. The dessicator was stored at room temperature for several days.

We found a fully passivated surface after 114 h reaction time. Fig. 6.4 a shows the pH response for a clean and passivated SiNW. Testing the chip against different electrolyte concentrations showed that also the nonlinear response to different salt concentrations becomes flat upon passivation (Fig. 6.4 b shows the response to KCl). This supports our model of anion adorption described in section 3.4. The reduction of surface hydroxyl groups due to silanization reduces the binding sites for protons and anions.

Using the liquid method in combination with PDMS microchannels to passivate SiNWs individually, could result in on-chip reference electrodes for differential pH sensing.
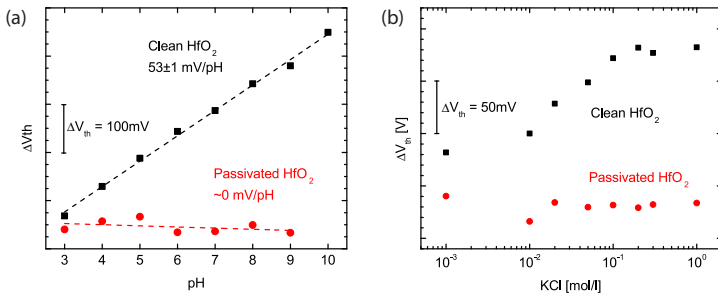
Figure 6.4: Surface passivation by liquid-phase silanization. A HfO$_2$-coated SiN-WFET chip before (squares) and after 114 h passivation (circles) (a) Change in threshold voltage *vs.* pH. The pH response is clearly reduced after passivation. (b) ΔV_{th} *vs.* KCl concentration. The reduction of hydroxyl groups also suppresses the response to salt concentration.

7

Conclusions and Outlook

In this work we have established a versatile sensor platform based on SiNWs. The sensor functionality was changed by surface modification for the detection of various analytes such as pH, alkaline ions and even FimH proteins. We achieved an ideal pH sensor with a response close to the Nernst limit. Full surface passivation for protons was accomplished for the implementation of a nanoscale reference electrode. Using the differential signal from differently functionalized SiNWs we could detect sodium and potassium ions selectively. Ultimately we present the detection of protein-ligand interactions of the physiologically relevant protein FimH. An extended site-binding model was derived to calculate the theoretical limits and assess the properties of the surface groups by evaluating the experimental results.

In conclusion we find that transducers based on ion-sensitive silicon nanowire field-effect transistors are in a promising stage for the realization of highly integrated biochemical sensors. The basic element is a reliable FET, showing a good transconductance (low subthreshold swing, extended linear regime, high on-off current ratio) which is achieved by maximizing the gate capacitance, while keeping the leakage current across the gate oxide at the minimum. The semiconductor-oxide interface quality is crucial, since charge trap states are the main source of electronic noise in ISFET devices. Studying SiNWs of different dimensions showed that larger sensor areas are beneficial in terms of signal-to-noise ratio, which is the basis for a good sensor performance. While the electronic noise decreases for larger structures, we find no effect on analyte response for the range of structure sizes used in this work. In contrast, the response is given by the surface properties such as the density and equilibrium constants of the active and competing surface

groups. We find that gold is a good surface material due to its low density of competing hydroxyl groups and the easy functionalization with thiol-based chemicals. However, for proton sensing Al_2O_3 and HfO_2 are to favour, given that both materials show a high pH response close to the Nernst limit. For all surfaces the response to the electrolyte background has to be considered. We find a strong nonspecific adsorption of anions on all surfaces containing hydroxyl groups which has to be considered for any biochemical sensing experiments.

The largest drawback of present ISFET sensors remains the reference electrode which is needed for a well defined liquid potential. Due to the size of commercial reference electrodes, the miniaturization of the liquid delivery system is limited. As we have seen, the fluidics play a major role regarding the stability and kinetics of a signal. Larger volumes limit the time scales and therefore the stability of the measurement since long time drift and induced air bubbles add additional noise to a signal baseline. However, measuring differential signals by using reference SiNWs could overcome the need for a true reference electrode. Another important aspect of BioFETs is the charge screening at high ionic strength. Most experiments are carried out at low or intermediate buffer concentration. For the reliable and accurate detection of large biomolecules under physiological conditions, new strategies for increasing the signals are needed.

Concerning the perspective for chemical sensing, we have achieved further results with calcium and fluoride ion selective linker molecules. Based on these results the influence of competing surface reactions will be studied in more details. The fact that ion selective molecules do not show full selectivity can be used for cross-reactive sensor arrays [119,120]. A large number of sensors with different selectivity to a large variety of chemical species could allow the detection of a broad range of molecules by using pattern recognition methods. To achieve the ultimate goal of a multifunctional sensor, different surface functionalization methods have to be considered. A feasible tool for local surface modification is micro drop printing. A different approach instead of direct detection of charged analytes is to detect secondary signals from binding reactions, such as protons. This has been successfully demonstrated for DNA sequencing [18,121] and glucose sensing [122,123]. Further, covering ISFETs with membranes with embedded channel proteins can be used to control the flow of specific ions [124].

A further step towards integration of many sensors has been done by our project collaborators. Paolo Livi from the Bio Engineering Laboratory at D-BSSE (ETH) has developed a CMOS chip for the current readout of our 48

SiNW sensor chip[125,126]. Having fast and parallel readout including digitalization on chip we can avoid the use of external electronics. This is an important step towards multiplexed sensing with highly integrated structures which can be produced at reasonable costs[127]. For the integration of a large number of transistors the question arises whether a local transistor underneath the sensing surface is needed. In a study by Guan *et al.*[128], off-chip extended gate field-effect transistors were used for pH sensing. This approach could be adopted for the gold-coated SiNWs to simplify the sensor design for a high sensor density device. However, it has to be considered that the capacitance of the sensing area has to be much larger as compared to the leads and FET capacitances.

Using the unique electronic properties of graphene as field-effect sensors can have several advantages compared to silicon. Graphene is intrinsically insensitive to pH[27] and can be used as reference electrode. By noncovalent functionalization of graphene specific analytes can be detected while the electrical properties of graphene are preserved[29]. Since no gate oxide is needed, variations in surface potential and double-layer capacitance can be measured simultaneously[129,130]. This additional quantity gives further information on electrolyte concentration and binding-adsorption kinetics. Further, the electronic properties of graphene allow high-frequency measurements in the gigahertz regime[29]. Reaching time resolutions in the range of nanoseconds can provide insights in double-layer formation and binding kinetics[131].

Considering recent scientific progress in the field of ISFETs and moreover the achievements within this project, FET based sensors show great promise for their use in healthcare and environmental industry.

Bibliography

[1] Bergveld, P. (1970) Development of an Ion-Sensitive Solid-State Device for Neurophysiological Measurements. *IEEE Trans. Biomed. Eng. BME-17*, 70–71.

[2] Cui, Y., Wei, Q., Park, H., and Lieber, C. M. (2001) Nanowire Nanosensors for Highly Sensitive and Selective Detection of Biological and Chemical Species. *Science 293*, 1289–1292.

[3] Knopfmacher, O., Tarasov, A., Fu, W., Wipf, M., Niesen, B., Calame, M., and Schönenberger, C. (2010) Nernst Limit in Dual-Gated Si-Nanowire FET Sensors. *Nano Lett. 10*, 2268–2274.

[4] Chen, S., Bomer, J. G., Carlen, E. T., and van den Berg, A. (2011) Al_2O_3/Silicon NanoISFET with Near Ideal Nernstian Response. *Nano Lett. 11*, 2334–2341.

[5] Janata, J. (1992) Chemical Sensors. *Anal. Chem. 64*, R196–R219.

[6] Sudhölter, E., van der Wal, P., Skowronska-Ptasinska, M., van den Berg, A., and Reinhoudt, D. (1989) Ion-Sensing using Chemically-Modified ISFETs. *Sensors and Actuators 17*, 189–194.

[7] Rocher, V., Jaffrezic-Renault, N., Perrot, H., Chevalier, Y., and Perchec, P. L. (1992) Nitrate-Sensitive Field-Effect Transistor with Silica Gate Insulator Modified by Chemical Grafting. *Anal. Chim. Acta 256*, 251 – 255.

[8] Reinhoudt, D. N., Engbersen, J. F. J., Brzozka, Z., van der Vlekkert, H. H., Honig, G. W. N., Holterman, H. A. J., and Verkerk, U. H. (1994) Development of Durable K^+-Selective Chemically Modified Field Effect Transistors with Functionalized Polysiloxane Membranes. *Anal. Chem. 66*, 3618–3623.

[9] Park, L., Hur, Y., and Sohn, B. (1996) Effect of Membrane Structure on the Performance of Field-Effect Transistor Potassium-Sensitive Sensor. *Sens. Actuators*, *A 57*, 239–243.

[10] Luo, L., Jie, J., Zhang, W., He, Z., Wang, J., Yuan, G., Zhang, W., Wu, L. C. M., and Lee, S.-T. (2009) Silicon Nanowire Sensors for Hg^{2+} and Cd^{2+} Ions. *Appl. Phys. Lett. 94*.

[11] Gao, A., Lu, N., Wang, Y., Dai, P., Li, T., Gao, X., Wang, Y., and Fan, C. (2012) Enhanced Sensing of Nucleic Acids with Silicon Nanowire Field Effect Transistor Biosensors. *Nano Lett. 12*, 5262–5268.

[12] Zheng, G., Patolsky, F., Cui, Y., Wang, W. U., and Lieber, C. M. (2005) Multiplexed Electrical Detection of Cancer Markers with Nanowire Sensor Arrays. *Nat Biotech 23*, 1294–1301.

[13] Stern, E., Klemic, J. F., Routenberg, D. A., Wyrembak, P. N., Turner-Evans, D. B., Hamilton, A. D., LaVan, D. A., Fahmy, T. M., and Reed, M. A. (2007) Label-Free Immunodetection with CMOS-Compatible Semiconducting Nanowires. *Nature 445*, 519–522.

[14] Stern, E., Vacic, A., Rajan, N. K., Criscione, J. M., Park, J., Ilic, B. R., Mooney, D. J., Reed, M. A., and Fahmy, T. M. (2010) Label-Free Biomarker Detection from whole Blood. *Nat Nano 5*, 138–142.

[15] Elfström, N., Karlström, A. E., and Linnros, J. (2008) Silicon Nanoribbons for Electrical Detection of Biomolecules. *Nano Lett. 8*, 945–949.

[16] Duan, X., Li, Y., Rajan, N. K., Routenberg, D. A., Modis, Y., and Reed, M. A. (2012) Quantification of the Affinities and Kinetics of Protein Interactions Using Silicon Nanowire Biosensors. *Nat Nano 7*, 401–407.

[17] Duan, X., Gao, R., Xie, P., Cohen-Karni, T., Qing, Q., Choe, H. S., Tian, B., Jiang, X., and Lieber, C. M. (2012) Intracellular Recordings of Action Potentials by an Extracellular Nanoscale Field-Effect Transistor. *Nat Nano 7*, 174–179.

[18] Rothberg, J. M. et al. (2011) An Integrated Semiconductor Device Enabling Non-Optical Genome Sequencing. *Nature 475*, 348–352.

[19] Tans, S. J., Verschueren, A. R. M., and Dekker, C. (1998) Room-temperature transistor based on a single carbon nanotube. *Nature 393*, 49–52.

[20] Kong, J., Franklin, N. R., Zhou, C., Chapline, M. G., Peng, S., Cho, K., and Dai, H. (2000) Nanotube Molecular Wires as Chemical Sensors. *Science 287*, 622–625.

[21] Collins, P. G., Bradley, K., Ishigami, M., and Zettl, A. (2000) Extreme Oxygen Sensitivity of Electronic Properties of Carbon Nanotubes. *Science 287*, 1801–1804.

[22] Krüger, M., Buitelaar, M. R., Nussbaumer, T., Schönenberger, C., and Forró, L. (2001) Electrochemical carbon nanotube field-effect transistor. *Applied Physics Letters 78*, 1291–1293.

[23] Olsen, T. J., Choi, Y., Sims, P. C., Gul, O. T., Corso, B. L., Dong, C., Brown, W. A., Collins, P. G., and Weiss, G. A. (2013) Electronic Measurements of Single-Molecule Processing by DNA Polymerase I (Klenow Fragment). *Journal of the American Chemical Society 135*, 7855–7860.

[24] Ang, P. K., Chen, W., Wee, A. T. S., and Loh, K. P. (2008) Solution-Gated Epitaxial Graphene as pH Sensor. *Journal of the American Chemical Society 130*, 14392–14393, PMID: 18850701.

[25] Ohno, Y., Maehashi, K., Yamashiro, Y., and Matsumoto, K. (2009) Electrolyte-Gated Graphene Field-Effect Transistors for Detecting pH and Protein Adsorption. *Nano Letters 9*, 3318–3322, PMID: 19637913.

[26] Cheng, Z., Li, Q., Li, Z., Zhou, Q., and Fang, Y. (2010) Suspended Graphene Sensors with Improved Signal and Reduced Noise. *Nano Letters 10*, 1864–1868.

[27] Fu, W., Nef, C., Knopfmacher, O., Tarasov, A., Weiss, M., Calame, M., and Schönenberger, C. (2011) Graphene Transistors Are Insensitive to pH Changes in Solution. *Nano Lett. 11*, 3597–3600.

[28] Fu, W., Nef, C., Tarasov, A., Wipf, M., Stoop, R., Knopfmacher, O., Weiss, M., Calame, M., and Schönenberger, C. Sensing with liquid-gated graphene field-effect transistors. Nanotechnology (IEEE-NANO), 2012 12th IEEE Conference on. 2012; pp 1–2.

[29] Fu, W., El Abbassi, M., Hasler, T., Jung, M., Steinacher, M., Calame, M., Schönenberger, C., Puebla-Hellmann, G., Hellmüller, S., Ihn, T., and Wallraff, A. (2014) Electrolyte gate dependent high-frequency measurement of graphene field-effect transistor for sensing applications. *Applied Physics Letters 104*, –.

[30] Elfström, N., Juhasz, R., Sychugov, I., Engfeldt, T., Karlström, A. E., and Linnros, J. (2007) Surface Charge Sensitivity of Silicon Nanowires: Size Dependence. *Nano Lett. 7*, 2608–2612.

[31] Patolsky, F., Zheng, G., and Lieber, C. M. (2006) Fabrication of silicon nanowire devices for ultrasensitive, label-free, real-time detection of biological and chemical species. *Nat. Protocols 1*, 1711–1724.

[32] Bergveld, P. (2003) Thirty years of ISFETOLOGY: What happened in the past 30 years and what may happen in the next 30 years. *Sens. Actuators*, *B 88*, 1–20.

[33] Nobel Media AB, The Transistor in a Century of Electronics. 2013; `http://www.nobelprize.org/educational/physics/transistor/history/`.

[34] Transistor count. 2014; `http://en.wikipedia.org/wiki/Transistor_count`.

[35] Nazarov, A., Colinge, J.-P., Balestra, F., Raskin, J.-P., Gamiz, F., and Lysenko, V. *Semiconductor-On-Insulator Materials for Nanoelectronics Applications*; 1612-1317; Springer Berlin Heidelberg, 2011.

[36] Singh, J. In *Semiconductor Devices: An Introduction*; Hoffman, G. T., Ed.; McGraw-Hill Book Co., 1994.

[37] Sze, S. M. *Physics of Semiconductor Devices*, 3rd ed.; Wiley-Interscience, 2006.

[38] Stockinger, M. Subthreshold Leakage. online, 2000; `http://www.iue.tuwien.ac.at/phd/stockinger/node13.html`, `http://www.iue.tuwien.ac.at/phd/stockinger/node13.html`.

[39] Colinge, J.-P., Lee, C.-W., Afzalian, A., Akhavan, N. D., Yan, R., Ferain, I., Razavi, P., O'Neill, B., Blake, A., White, M., Kelleher, A.-M., McCarthy, B., and Murphy, R. (2010) Nanowire transistors without junctions. *Nat Nano 5*, 225–229.

[40] Bagotsky, V. *Fundamentals of Electrochemistry*; The ECS Series of Texts and Monographs; Wiley, 2005.

[41] Chen, S., and Zhang, S.-L. (2011) Contacting versus Insulated Gate Electrode for Si Nanoribbon Field-Effect Sensors Operating in Electrolyte. *Analytical Chemistry 83*, 9546–9551.

[42] Chen, S., Nyholm, L., Jokilaakso, N., Eriksson Karlström, A., Linros, J., Smith, U., and Zhang, S.-L. (2011) Current Instability for Silicon Nanowire Field-Effect Sensors Operating in Electrolyte with Platinum Gate Electrodes. *Electrochemical and Solid-State Letters 14*, J34–J37.

[43] van Hal, R., Eijkel, J., and Bergveld, P. (1996) A general model to describe the electrostatic potential at electrolyte oxide interfaces. *Advances in Colloid and Interface Science 69*, 31–62.

[44] Vonau, W., Oelssner, W., Guth, U., and Henze, J. (2010) An all-solid-state reference electrode. *Sensors and Actuators B: Chemical 144*, 368 – 373.

[45] Temiz, Y., Ferretti, A., Leblebici, Y., and Guiducci, C. (2012) A comparative study on fabrication techniques for on-chip microelectrodes. *Lab Chip 12*, 4920–4928.

[46] Accastelli, E., Cappi, G., Buckley, J., Ernst, T., and Guiducci, C. Comparison between front- and back-gating of Silicon Nanoribbons in real-time sensing experiments. 13th IEEE Conference on Nanotechnology, 2013. 2013; pp 517–520.

[47] Schasfoort, R., Bergveld, P., Kooyman, R., and Greve, J. (1990) Possibilities and limitations of direct detection of protein charges by means of an immunological field-effect transistor. *Analytica Chimica Acta 238*, 323–329.

[48] Bousse, L., De Rooij, N., and Bergveld, P. (1983) Operation of Chemically Sensitive Field-Effect Sensors as a Function of the Insulator-Electrolyte Interface. *IEEE Trans. Electron Devices 30*, 1263–1270.

[49] Fung, C., Cheung, P., and Ko, W. (1986) A generalized theory of an electrolyte-insulator-semiconductor field-effect transistor. *Electron Devices, IEEE Transactions on 33*, 8–18.

[50] Tarasov, A., Wipf, M., Bedner, K., Kurz, J., Fu, W., Guzenko, V. A., Knopfmacher, O., Stoop, R. L., Calame, M., and Schönenberger, C. (2012) True Reference Nanosensor Realized with Silicon Nanowires. *Langmuir 28*, 9899–9905.

[51] Tarasov, A., Wipf, M., Stoop, R. L., Bedner, K., Fu, W., Guzenko, V. A., Knopfmacher, O., Calame, M., and Schönenberger, C. (2012) Understanding the Electrolyte Background for Biochemical Sensing with Ion-Sensitive Field-Effect Transistors. *ACS Nano 6*, 9291–9298.

[52] von Haartman, M., and Östling, M. *Low-Frequency Noise in Advanced MOS Devices*; Analog Circuits and Signal Processing; Springer, 2007.

[53] Bedner, K., Guzenko, V. A., Tarasov, A., Wipf, M., Stoop, R. L., Rigante, S., Brunner, J., Fu, W., David, C., Calame, M., Gobrecht, J., and Schönenberger, C. (2014) Investigation of the dominant 1/f noise source in silicon nanowire sensors. *Sensors and Actuators B: Chemical 191*, 270 – 275.

[54] Ghibaudo, G. (1989) On the theory of carrier number fluctuations in {MOS} devices. *Solid-State Electronics 32*, 563 – 565.

[55] Vacic, A., Criscione, J. M., Rajan, N. K., Stern, E., Fahmy, T. M., and Reed, M. A. (2011) Determination of Molecular Configuration by Debye Length Modulation. *Journal of the American Chemical Society 133*, 13886–13889.

[56] Bergveld, P. (1991) A critical evaluation of direct electrical protein detection methods. *Biosens. Bioelectron. 6*, 55 – 72.

[57] Meixner, L., and Koch, S. (1992) Simulation of {ISFET} operation based on the site-binding model. *Sensors and Actuators B: Chemical 6*, 315 – 318.

[58] Wipf, M., Stoop, R. L., Tarasov, A., Bedner, K., Fu, W., Wright, I. A., Martin, C. J., Constable, E. C., Calame, M., and Schönenberger, C. (2013) Selective Sodium Sensing with Gold-Coated Silicon Nanowire Field-Effect Transistors in a Differential Setup. *ACS Nano 7*, 5978–5983.

[59] Sheehan, P. E., and Whitman, L. J. (2005) Detection Limits for Nanoscale Biosensors. *Nano Letters 5*, 803–807.

[60] Knight, J. (2002) Microfluidics: Honey, I shrunk the lab. *Nature 418*, 474–475.

[61] Unger, M. A., Chou, H.-P., Thorsen, T., Scherer, A., and Quake, S. R. (2000) Monolithic Microfabricated Valves and Pumps by Multilayer Soft Lithography. *Science 288*, 113–116.

[62] Park, I., Li, Z., Pisano, A. P., and Williams, R. S. (2010) Top-down Fabricated Silicon Nanowire Sensors for real-time Chemical Detection. *Nanotechnology 21*, 015501.

[63] Li, Z., Chen, Y., Li, X., Kamins, T. I., Nauka, K., and Williams, R. S. (2004) Sequence-Specific Label-Free DNA Sensors Based on Silicon Nanowires. *Nano Letters 4*, 245–247.

[64] Knopfmacher, O. S. Sensing with Silicon Nanowire Field-Effect Transistors. PhD thesis, University of Basel, Department of Physics, 2011.

[65] Bedner, K. Fabrication and Characterization of Ion-Sensitive Field-Effect Transistors using Silicon-on-Insulator Technology. PhD thesis, University of Basel, Paul Scherrer Institut, 2013.

[66] Soitec, 2013; `http://www.soitec.com/en/`.

[67] Microchemicals, AZ nLOF. online, 2013; `http://www.microchemicals.com/products/photoresists/az_nlof_2020.html`.

[68] Kern, W. (1990) The Evolution of Silicon Wafer Cleaning Technology. *Journal of The Electrochemical Society 137*, 1887–1892.

[69] Nanotech, C. Savannah ALD 100. 2013; `http://www.cambridgenanotechald.com/thin-film-deposition.html`.

[70] Bedner, K., Guzenko, V. A., Tarasov, A., Wipf, M., Stoop, R. L., Just, D., Rigante, S., Fu, W., Minamisawa, R. A., David, C., Calame, M., Gobrecht, J., and Schönenberger, C. (2013) pH Response of Silicon Nanowire Sensors: Impact of Nanowire Width and Gate Oxide. *Sensors and Materials 25*, 567–576.

[71] Epotek, Epotek 353ND. online, 2013; `http://www.polyscience-ag.ch/index.php/de/aktuell/epo-tek-353nd-iso-10993`.

[72] Tarasov, A., Fu, W., Knopfmacher, O., Brunner, J., Calame, M., and Schönenberger, C. (2011) Signal-to-noise ratio in dual-gated silicon nanoribbon field-effect sensors. *Appl. Phys. Lett. 98*, 012114.

[73] Ulman, A. (1996) Formation and Structure of Self-Assembled Monolayers. *Chem. Rev. 96*, 1533–1554.

[74] Blöchl, P. E., and Stathis, J. H. (1999) Hydrogen Electrochemistry and Stress-Induced Leakage Current in Silica. *Phys. Rev. Lett. 83*, 372–375.

[75] Chang, C.-C., and Shu, M.-C. (2003) The Chemical Origin of Defects on Silicon Dioxide Exposed to Ethanol. *The Journal of Physical Chemistry B 107*, 7076–7087.

[76] Jakobson, C., and Nemirovsky, Y. (1999) 1/f noise in ion sensitive field effect transistors from subthreshold to saturation. *Electron Devices, IEEE Transactions on 46*, 259–261.

[77] Clément, N., Nishiguchi, K., Dufreche, J. F., Guerin, D., Fujiwara, A., and Vuillaume, D. (2011) A silicon nanowire ion-sensitive field-effect transistor with elementary charge sensitivity. *Applied Physics Letters 98*.

[78] Rajan, N. K., Routenberg, D. A., and Reed, M. A. (2011) Optimal signal-to-noise ratio for silicon nanowire biochemical sensors. *Applied Physics Letters 98*, 264107.

[79] Rajan, N. K., Brower, K., Duan, X., and Reed, M. A. (2014) Limit of detection of field effect transistor biosensors: Effects of surface modification and size dependence. *Applied Physics Letters 104*.

[80] Rajan, N. K., Duan, X., and Reed, M. A. (2013) Performance limitations for nanowire/nanoribbon biosensors. *Wiley Interdisciplinary Reviews: Nanomedicine and Nanobiotechnology*

[81] Heller, I., Chatoor, S., Männik, J., Zevenbergen, M. A. G., Oostinga, J. B., Morpurgo, A. F., Dekker, C., and Lemay, S. G. (2010) Charge Noise in Graphene Transistors. *Nano Letters 10*, 1563–1567.

[82] Mannik, J., Heller, I., Janssens, A. M., Lemay, S. G., and Dekker, C. (2008) Charge Noise in Liquid-Gated Single-Wall Carbon Nanotube Transistors. *Nano Letters 8*, 685–688, PMID: 18217786.

[83] Sharf, T., Kevek, J. W., DeBorde, T., Wardini, J. L., and Minot, E. D. (2012) Origins of Charge Noise in Carbon Nanotube Field-Effect Transistor Biosensors. *Nano Letters 12*, 6380–6384.

[84] Cheng, Z., Hou, J., Zhou, Q., Li, T., Li, H., Yang, L., Jiang, K., Wang, C., Li, Y., and Fang, Y. (2013) Sensitivity Limits and Scaling of Bioelectronic Graphene Transducers. *Nano Letters 13*, 2902–2907.

[85] Hunter, R. *Zeta Potential in Colloid Science: Principles and Applications*; Academic Press, 1981.

[86] Kosmulski, M. (2009) Compilation of PZC and IEP of sparingly soluble metal oxides and hydroxides from literature. *Advances in Colloid and Interface Science 152*, 14 – 25.

[87] Baucke, F. (2011) Fundamental and applied electrochemistry at an industrial glass laboratory an overview. *Journal of Solid State Electrochemistry 15*, 23–46.

[88] Belyustin, A. (2011) The centenary of glass electrode: from Max Cremer to F. G. K. Baucke. *Journal of Solid State Electrochemistry 15*, 47–65.

[89] Scholz, F. (2011) Nikolsky's ion exchange theory versus Baucke's dissociation mechanism of the glass electrode. *Journal of Solid State Electrochemistry 15*, 67–68.

[90] Bergveld, P. (1972) Development, Operation, and Application of the Ion-Sensitive Field-Effect Transistor as a Tool for Electrophysiology. *Biomedical Engineering, IEEE Transactions on BME-19*, 342–351.

[91] Sobczyńska, D., and Torbicz, W. (1984) ZrO2 gate pH-sensitive field effect transistor. *Sensors and Actuators 6*, 93 – 105.

[92] Zafar, S., D'Emic, C., Afzali, A., Fletcher, B., Zhu, Y., and Ning, T. (2011) Optimization of pH sensing using silicon nanowire field effect transistors with HfO 2 as the sensing surface. *Nanotechnology 22*, 405501.

[93] Nikolaides, M. G., Rauschenbach, S., Luber, S., Buchholz, K., Tornow, M., Abstreiter, G., and Bausch, A. R. (2003) Silicon-on-Insulator Based Thin-Film Resistor for Chemical and Biological Sensor Applications. *ChemPhysChem 4*, 1104–1106.

[94] Tarasov, A. Silicon Nanowire Field-Effect Transistors for Sensing Applications. PhD thesis, Universität Basel, 2013.

[95] Iler, R. K. *The Chemistry of Silica: Solubility, Polymerization, Colloid and Surface Properties and Biochemistry of Silica*; Wiley, 1979.

[96] Berube, Y., Onoda Jr, G., and De Bruyn, P. (1967) Proton adsorption at the ferric oxide/aqueous solution interface: II. Analysis of kinetic data. *Surface Science 7*, 448–461.

[97] Bousse, L., and Bergveld, P. (1984) The role of buried {OH} sites in the response mechanism of inorganic-gate pH-sensitive {ISFETs}. *Sensors and Actuators 6*, 65 – 78.

[98] Topkar, A., and Lal, R. (1993) Effect of electrolyte exposure on silicon dioxide in electrolyte-oxide-semiconductor structures. *Thin Solid Films 232*, 265 – 270.

[99] Williams, K., Gupta, K., and Wasilik, M. (2003) Etch rates for micromachining processing-Part II. *Microelectromechanical Systems*, *Journal of 12*, 761–778.

[100] Maciel, J., Martins, M. C. L., and Barbosa, M. A. (2010) The stability of self-assembled monolayers with time and under biological conditions. *J. Biomed. Mater. Res.*, *Part A 94A*, 833–843.

[101] Lohrengel, M., and Schultze, J. (1976) Electrochemical Properties of Anodic Gold Oxide Layers-I: Potentiostatic Oxide Growth and Double Layer Capacity. *Electrochim. Acta 21*, 957–965.

[102] Ron, H., and Rubinstein, I. (1994) Alkanethiol Monolayers on Preoxidized Gold. Encapsulation of Gold Oxide under an Organic Monolayer. *Langmuir 10*, 4566–4573.

[103] Ron, H., Matlis, S., and Rubinstein, I. (1998) Self-Assembled Monolayers on Oxidized Metals. 2. Gold Surface Oxidative Pretreatment, Monolayer Properties, and Depression Formation. *Langmuir 14*, 1116–1121.

[104] Steed, J., and Atwood, J. *Supramolecular Chemistry*; John Wiley & Sons, 2009.

[105] Wilson, G. S., and Gifford, R. (2005) Biosensors for real-time in vivo measurements. *Biosensors and Bioelectronics 20*, 2388 – 2403, 20th Anniversary of Biosensors and Bioelectronics.

[106] Cheng, M. M.-C., Cuda, G., Bunimovich, Y. L., Gaspari, M., Heath, J. R., Hill, H. D., Mirkin, C. A., Nijdam, A. J., Terracciano, R., Thundat, T., and Ferrari, M. (2006) Nanotechnologies for biomolecular detection and medical diagnostics. *Current Opinion in Chemical Biology 10*, 11 – 19, Proteomics and genomics.

[107] Healthcare, G. Biacore Sensor Surface Handbook. 2005;
`http://labs.idi.harvard.edu/springer/uploads/Protocols/`
`BiacoreSensorSurfaceHandbookweb.pdf`.

[108] Curreli, M., Zhang, R., Ishikawa, F., Chang, H.-K., Cote, R., Zhou, C.,
and Thompson, M. E. (2008) Real-Time, Label-Free Detection of Bi-
ological Entities Using Nanowire-Based FETs. *Nanotechnology, IEEE
Transactions on 7*, 651–667.

[109] Stern, E., Vacic, A., and Reed, M. A. (2008) Semiconducting Nanowire
Field-Effect Transistor Biomolecular Sensors. *Electron Devices, IEEE
Transactions on 55*, 3119–3130.

[110] Bunimovich, Y. L., Shin, Y. S., Yeo, W.-S., Amori, M., Kwong, G., and
Heath, J. R. (2006) Quantitative Real-Time Measurements of DNA Hy-
bridization with Alkylated Nonoxidized Silicon Nanowires in Elec-
trolyte Solution. *Journal of the American Chemical Society 128*, 16323–
16331.

[111] DeChancie, J., and Houk, K. N. (2007) The Origins of Femtomolar
Protein-Ligand Binding: Hydrogen-Bond Cooperativity and Desolva-
tion Energetics in the Biotin-(Strept)Avidin Binding Site. *Journal of the
American Chemical Society 129*, 5419–5429, PMID: 17417839.

[112] Scharenberg, M., Jiang, X., Pang, L., Navarra, G., Rabbani, S.,
Binder, F., Schwardt, O., and Ernst, B. (2014) Kinetic Properties of
Carbohydrate Lectin Interactions: FimH Antagonists. *ChemMedChem
9*, 78–83.

[113] Oshannessy, D., Brighamburke, M., Soneson, K., Hensley, P., and
Brooks, I. (1993) Determination of Rate and Equilibrium Binding
Constants for Macromolecular Interactions Using Surface Plasmon
Resonance: Use of Nonlinear Least Squares Analysis Methods. *Ana-
lytical Biochemistry 212*, 457 – 468.

[114] Myszka, D. G., He, X., Dembo, M., Morton, T. A., and Goldstein, B.
(1998) Extending the range of rate constants available from BIACORE:
interpreting mass transport-influenced binding data. *Biophys. J* 583–
594.

[115] RCSB Protein Data Bank, FimH adhesin receptor binding domain
from uropathogenic E. coli. online, 2014; `http://www.rcsb.org/`
`pdb/explore.do?structureId=1uwf`.

[116] Wipf, M., Stoop, R. L., Tarasov, A., Bedner, K., Fu, W., Calame, M., and Schönenberger, C. Potassium sensing with membrane-coated silicon nanowire field-effect transistors. 2013 Transducers Eurosensors XXVII: The 17th International Conference on Solid-State Sensors, Actuators and Microsystems. 2013; pp 1182–1185.

[117] Izatt, R. M., Bradshaw, J. S., Nielsen, S. A., Lamb, J. D., Christensen, J. J., and Sen, D. (1985) Thermodynamic and kinetic data for cation-macrocycle interaction. *Chemical Reviews 85*, 271–339.

[118] Inokuchi, Y., Boyarkin, O. V., Kusaka, R., Haino, T., Ebata, T., and Rizzo, T. R. (2012) Ion Selectivity of Crown Ethers Investigated by UV and IR Spectroscopy in a Cold Ion Trap. *The Journal of Physical Chemistry A 116*, 4057–4068.

[119] Albert, K. J., Lewis, N. S., Schauer, C. L., Sotzing, G. A., Stitzel, S. E., Vaid, T. P., and Walt, D. R. (2000) Cross-Reactive Chemical Sensor Arrays. *Chemical Reviews 100*, 2595–2626.

[120] Natale, C. D., D'Amico, A., and Davide, F. A. (1993) Redundancy in sensor arrays. *Sensors and Actuators A: Physical 37-38*, 612 – 617, Proceedings of Eurosensors {VI}.

[121] Guiducci, C., and Spiga, F. M. (2013) Another transistor-based revolution: on-chip qPCR. *Nat Meth 10*, 617–618.

[122] Wang, X., Chen, Y., Gibney, K. A., Erramilli, S., and Mohanty, P. (2008) Silicon-based nanochannel glucose sensor. *Applied Physics Letters 92*.

[123] Park, K.-Y., Choi, S.-B., Lee, M., Sohn, B.-K., and Choi, S.-Y. (2002) {ISFET} glucose sensor system with fast recovery characteristics by employing electrolysis. *Sensors and Actuators B: Chemical 83*, 90 – 97.

[124] Zhang, X., Fu, W., Palivan, C. G., and Meier, W. (2013) Natural channel protein inserts and functions in a completely artificial, solid-supported bilayer membrane. *Sci. Rep. 3*.

[125] Livi, P., Wipf, M., Tarasov, A., Stoop, R., Bedner, K., Rothe, J., Chen, Y., Stettler, A., Schönenberger, C., and Hierlemann, A. Silicon nanowire ion-sensitive field-effect transistor array integrated with a CMOS-based readout chip. 2013 Transducers Eurosensors XXVII: The 17th International Conference on Solid-State Sensors, Actuators and Microsystems. 2013; pp 1751–1754.

[126] Livi, P., Rigante, S., Chen, Y., Ionescu, A., and Hierlemann, A. (2012) A Hybrid FinFET-based Biosensor with Integrated Readout Capability. *Procedia Engineering 47*, 821 – 824, 26th European Conference on Solid-State Transducers, Eurosensor 2012.

[127] Benini, L., Guiducci, C., and Paulus, C. (2007) Electronic Detection of DNA Hybridization: Toward CMOS Microarrays. *Design & Test of Computers, IEEE 24*, 38–48.

[128] Guan, W., Rajan, N., Duan, X., and Reed, M. (2013) Quantitative probing of surface charges at dielectric-electrolyte interfaces. *Lab Chip 13*, 1431–1436–.

[129] Chen, S., Zhang, Z.-B., Ma, L., Ahlberg, P., Gao, X., Qiu, Z., Wu, D., Ren, W., Cheng, H.-M., and Zhang, S.-L. (2012) A graphene field-effect capacitor sensor in electrolyte. *Applied Physics Letters 101*, –.

[130] Xia, J., Chen, F., Li, J., and Tao, N. (2009) Measurement of the quantum capacitance of graphene. *Nat Nano 4*, 505–509.

[131] Kulkarni, G. S., and Zhong, Z. (2012) Detection beyond the Debye Screening Length in a High-Frequency Nanoelectronic Biosensor. *Nano Lett. 12*, 719–723.

A

Fabrication Protocols

The fabrication protocol is taken from the PhD thesis of Kristine Bedner [65]

Device Fabrication

SOI wafer characteristics

Wafer:	8" silicon-on-insulator (SOI)
Supplier:	SOITEC France
Device layer:	
Orientation:	(100)
Dopant:	p-type, boron
Resistivity:	$8.5 - 11.5\,\Omega\mathrm{cm}$
Thickness:	$88\,\mathrm{nm}$
Buried oxide (SiO$_2$)	
Thickness:	$145\,\mathrm{nm}$
Silicon handle wafer:	
Type:	CZ, p-type
Resistivity:	$8 - 22\,\Omega\mathrm{cm}$
Thickness:	$725\,\mu\mathrm{m}$

Thinning

- 1. Sample cleaning
    - Piranha solution: H_2O_2:H_2SO_4 - 2 : 1, for $10\,\mathrm{min}$ at $95°C$

– HF dip

2. Thermal oxidation of silicon device layer

Alignment marker fabrication

- 1. Spin coating:
  PMMA 672.11, 1500 rpm, thickness $\approx 3\,\mu$m
  Bake on hotplate for 5 min at 175°C
  Gradual cooling of the sample to avoid cracks in PMMA

  2. Electron beam lithography: Vistec EBPG 5000$^+$
  Resolution = 0.03 μm, beam step size = 0.03 μm
  Beam current = 150 nA, dose = 1000 μC/cm^2
  Marker size: 10 μm $\times$ 10 μm

  3. Development: Hamatech
  IPA:MIBK - 3 : 1, 2 min, rinse in IPA 30 s

  4. Reactive ion etching (RIE): Oxford RIE 100

    – *Top SiO$_2$:* CHF$_3$ 12 sccm, Ar 38 sccm, 30 mTorr, 100 W, 300 K, V_{DC} = 485 V for 2 min

    – *Device Si layer:* CHF$_3$ 12 sccm, SF$_6$ 4 sccm, O$_2$ 3 sccm, 50 mTorr, 100 W, 300 K, V_{DC} = 365 V for 5 min

    – *Buried SiO$_2$:* CHF$_3$ 12 sccm, Ar 38 sccm, 30 mTorr, 100 W, 300 K, V_{DC} = 485 V for 8 min

    – *Si handle wafer:* CHF$_3$ 30 sccm, SF$_6$ 30 sccm, O$_2$ 2 sccm, 50 mTorr, 100 W, 300 K, V_{DC} = 365 V for 21 min

    – Resulting alignment marker depth: $\approx 1\,\mu$m

  5. Sample cleaning: Remove PMMA in acetone and then in Piranha solution H$_2$O:H$_2$SO$_4$ - 2 : 1 for 10 min at 95°C Piranha

Electron beam lithography: Device pattern

- 1. Spin coating:
  Ti primer, 4000 rpm, bake for 1 min at 110°C
  nLOF:EBR : 4, 4000 rpm, bake for 1 min at 110°C

  2. Exposure:

    – *SiNWs:* Resolution = 0.005 μm, beam step size = 0.005 μm, beam current 2 nA, dose 180 μC/cm^2

- *Large structures:* Resolution = 0.005 µm, beam step size = 0.03 µm, beam current 50 nA, dose 165 µC/cm^2

3. Post exposure bake: 1 min at 110°C

4. Development: AZ MIF 826 for 25 s, rinse in DI-water

Device etching

- 1. RIE etching of SiO$_2$ top oxide: Oxford RIE 100; CHF$_3$ 12 sccm, Ar 38 sccm, 30 mTorr, 100 W, 300 K, V_{DC} = 485 V for 27 s

2. Buffered HF dip to remove remaining oxide

3. Chemical wet etching of Si device layer: Tetramethylammonium hydroxide (TMAH) and IPA (10 vol%) for 2 min at 45°C

4. Sample cleaning: Piranha solution H$_2$O$_2$:H$_2$SO$_4$ 2 : 1 for 10 min at 95°C

Contact fabrication I

- 1. Spin coating PMMA 672.08, 3000 rpm, bake for 30 min at 175°C, gradual cooling of the sample

2. Electron beam lithography: Vistec EBPG 5000$^+$

   - *SiNWs:* Resolution = 0.005 µm, beam step size = 0.005 µm, beam current 2 nA, dose 850 µC/cm^2

   - *Large structures:* Resolution = 0.005 µm, beam step size = 0.03 µm, beam current 190 nA, dose 850 µC/cm^2

3. Development: Hamatech; IPA:MIBK 3 : 1 2 min, rinse in IPA 30 s

4. Ion implantation at Ion Beam Services (IBS), Peynier, France; BF$_2^+$, energy = 43 keV, dose = 2.3 · 10^{15} cm^{-2}

5. Removal of PMMA implantation mask in acetone

6. Sample cleaning: RIE O$_2$, 40 sccm, 200 mTorr, 30 W, afterwards Piranha solution

7. Thermal activation of dopants: PPC Process Product Corporation annealing oven; annealing for 6 min at 950°C in forming gas and N$_2$

RCA cleaning and ALD deposition

- 1. Piranha solution H_2O_2:H_2SO_4 2 : 1 for 10 min at 95°C
  2. Buffered HF for 35 s to remove thermal top oxide layer
  3. RCA 1 cleaning: H_2O:H_2O_2:NH_4OH 20 : 4 : 1 for 10 min at 65°C
  4. Buffered HF dip
  5. RCA 2 cleaning: H_2O:H_2O_2:HCl 20 : 1 : 1 for 10 min at 65°C
  6. Atomic layer deposition (ALD) at 225°C for Al_2O_3 and at 200°C for HfO_2

Contact fabrication II

- 1. Dehydration bake for 10 min at 200°C
  2. Spin coating: HMDS, 4000 rpm, bake for 1 min at 110°C
  3. Optical lithography: Karl SÃijss MJB 3, 6 s
  4. Development: AZ MIF 826 for 80 s
  5. Opening of the contact window in the gate oxide:
     - Al_2O_3 200 deposition cycles: Buffered HF 35 s
     - HfO_2 200 deposition cycles: Buffered HF $\approx$ 5 min
  6. Metallization by electron beam evaporation (BAK 600), AlSi (1 %) 300 nm
  7. Lift-off in n-methyl-2-pyrrolidon (NMP) at room temperature
  8. Annealing of contact metal and ALD oxide: Annealing for 10 min at 450°C in forming gas

SU-8 protection layer and liquid opening

- 1. Dehydration bake for 10 min at 200°C
  2. Spin coating: SU-8 2002, 4000 rpm, bake 1 min at 95°C
  3. Optical lithography, 18 s
  4. Post exposure bake: 1 min at 110°C
  5. Development: EC 11 90 s, rinse in IPA
  6. Hard bake of SU-8 on hotplate: Bake sample for 25 min at 180°C, gradual cooling of the sample

Dicing

- 1. Spin coating of microposit S1813, 1000 rpm, bake 2 min at 110°C
  2. Sawing: Disco DAT 341 or Esec 8003, sample size 9 mm × 9 mm
  3. Removal of resist with acetone

Packaging

- 1. Scratch back side of the sample with diamond scriber, glue the sample in 64 pin chip carrier (IPK64F1-2219A, NTK Technologies Inc.) by silver epoxy
  2. Aluminum wire wedge bonding: MEI Marpet Enterprises Inc
  3. PDMS microchannel
     - Mix polydimethylsiloxane (PDMS, *SYLGARD 184 Silicone Elastomer*) with curing agent (10 : 1)
     - Pour PDMS onto SU-8 patterned Si wafers, keep at room temperature for ≈ 1 h until all the bubbles have cleared
     - Heating at 60°C for 2 h.
     - Pierce inlets with *Harris Uni-Core* 0.75 mm for tubing
     - Cut PDMS with razorblade and align to sample
  4. Epoxy sealing: Epotek 353ND, degass, bake for 5 min at 120°C
  5. Tubing: Polytetrafluoroethylene (PTFE) 0.3 mm ID × 0.76 mm OD

Au-film for gold-coated SiNWs

1. Spin coating:
   - O_2 plasma: RIE O_2, 40 sccm, 200 mTorr, 30 W, 300 K, $V_{DC} = 87$ V, 8 s
   - Spin coating of PMMA 669.04, 6000 rpm, thickness ≈ 220 nm
   - Bake on hotplate for 3 min at 175°C

2. Electron beam lithography: Vistec EBPG 5000$^+$, resolution = 0.01 μm, beam step size = 0.01 μm, beam current 2 nA, dose 850 μC/cm^2

3. Development: Hamatech, IPA:MIBK 3 : 1, 2 min, rinse in IPA 65 s
   O_2 plasma: O_2 40 sccm, 200 mTorr, 30 W, 300 K, $V_{DC} = 87$ V, 8 s

4. Metal evaporation: Electron beam evaporation with UNIVEX, Cr 5 nm, Au 20 nm

5. Lift-off in acetone for several hours

SU-8 structures for PDMS microchannels

1. Clean oxidized Si wafer in DI water, acetone, IPA

2. Dehydration bake for 10 min at 200°C

3. Spin coating: SU-8 50 (1250 rpm for 100 μm and 2000 rpm for 50 μm thick layers), bake 10 min at 65°C

4. Electron beam lithography: Vistec EBPG 5000$^+$, resolution = 0.05 μm, beam step size = 0.05 μm, beam current = 1 nA, dose = 5 μC/cm^2

5. Post exposure bake: 90 s at 110°C

6. Development: EC 11 12 min, rinse in IPA

7. Hard bake of SU-8 on hotplate: Bake sample for 20 min at 180°C, gradual cooling of the sample

Electrolyte solutions

Standard pH buffer solutions were used for the pH measurement (Titrisol, *Merck*). KCl (ACS 99.0 – 100.5%, Alfa Aesar), NaCl ($\geq$ 99.5%, *Fluka*), CaCl$_2$, MgCl$_2$, NaF and CaCO$_3$ (*Sigma-Aldrich*, ACS $\geq$ 99%) were dissolved in deionized water (resistivity = 17 MΩ·cm) with $\approx$ 4 mM HEPES buffer and $\approx$ 1.5 mM KOH, resulting in a pH value around 7. For the solutions at different pH no buffer was used and pH was adjusted by adding KOH, NH$_3$ or acetic acid (C$_2$H$_4$O$_2$) and controlled by a pH meter.

Supporting Measurements

Ohmic Contact Characterization

Ohmic contacts were characterized in air. We measured the source-drain current I_{sd} *vs.* source-drain voltage V_{sd} at different back-gate voltages. The current through the SiNW including contacts is proportional to the voltage applied, according to Ohm's law. Fig. B.1 shows the $I - V$ curves for two SiNWs of 100 nm and 500 nm width.
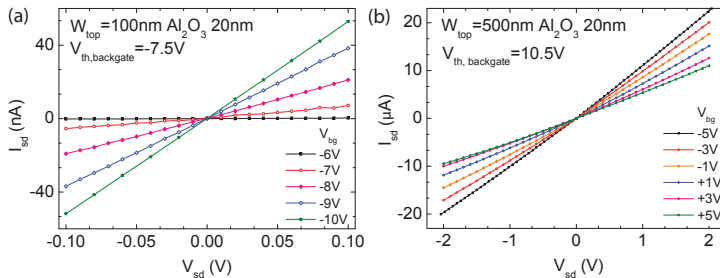
Figure B.1: Source-drain current I_{sd} *vs.* V_{sd} at different back-gate voltages measured in air (liquid gate floating). (a) 100 nm wide SiNW, (b) 500 nm wide SiNW. I_{sd} is proportional to V_{sd}, which is characteristic for Ohmic contacts. At voltages up to 100 mV I_{sd} is virtually linear. Figure adapted from [65].

Conductance at Different Electrolyte Concentrations

We measured conductance at different salt concentrations to study the change in V_{th} (see section 3.4). Fig. B.2 shows the conductance as a function of V_{ref} at different KCl concentrations. While V_{th} shifts to more positive voltage for higher concentrations, the shape of the transfer curve and especially the subthreshold swing does not change with increasing KCl concentration. Hence, the total liquid gate capacitance is insignificantly affected by the change in double layer capacitance, given by the electrolyte concentration. This indicates that the total gate capacitance is dominated by the oxide capacitance.
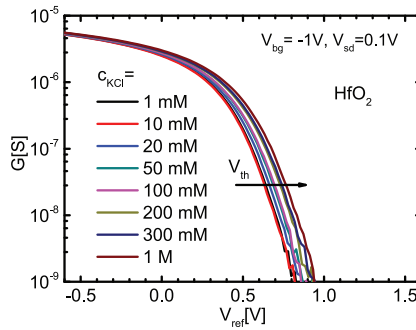
Figure B.2: Conductance G vs. V_{ref} for a HfO$_2$ coated SiNW measured at different KCl concentrations. V_{th} shifts to more positive values with increasing ionic strength. No significant dependence of the transfer curve on the ionic strength is found.

Appendix C

The Two-Compartment Model

A typical model to describe the binding kinetics of a surface immobilized ligand to capture an analyte in solution is the two-compartment reaction model[16]. Initially the analyte and the ligands are separated. The transport rate k_M describes the exchange of analytes from bulk solution to the proximity of the ligands. The interaction of analytes close to the surface and the ligands is described by the association rate k_a and dissociation rate k_d as given in Eq. 5.8 and 5.9. To illustrate the influence of the transport rate, Fig. C.1 shows a model system with $k_a = 10^4\,\mathrm{M^{-1}s^{-1}}$, $k_d = 10^{-4}\,\mathrm{s^{-1}}$ ($K_D = 10\,\mathrm{nM}$) for different ligand densities and different k_M.
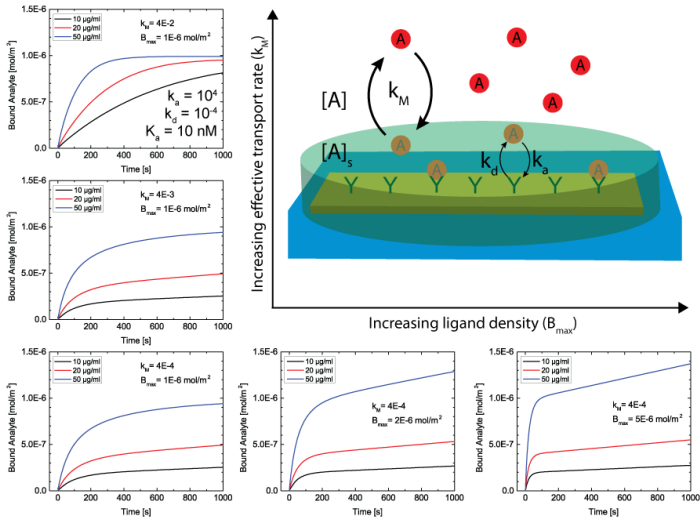
Figure C.1: Schematic representation a two-compartment model. A model system with $k_a = 10^4$, $k_d = 10^{-4}$ illustrates the influence of the rate constant k_M (vertical) and the ligand density $[B]_{max}$ (horizontal) on the kinetics during association. The curves show the number of bound analytes ($[AB]$) in mol/m^2 vs. time.

Publication List

Peer-Reviewed Journal Publications

1. O. Knopfmacher, A. Tarasov, W. Fu, M. Wipf, B. Niesen, M. Calame and C. Schönenberger. Nernst Limit in Dual-Gated Si-Nanowire FET Sensors. *Nano Lett. 10*, 2268–2274 (2010)

2. A. Tarasov, M. Wipf, K. Bedner, J. Kurz, W. Fu, V.A. Guzenko, O. Knopfmacher, R.L. Stoop, M. Calame and C. Schönenberger. True Reference Nanosensor Realized with Silicon Nanowires. *Langmuir 28*, 9899–9905 (2012)

3. A.Tarasov, M. Wipf, R.L. Stoop, K. Bedner, W. Fu, V.A. Guzenko, O. Knopfmacher, M. Calame and C. Schönenberger. Understanding the Electrolyte Background for Biochemical Sensing with Ion-Sensitive Field-Effect Transistors. *ACS Nano 6*, 9291–9298 (2012)

4. O. Knopfmacher, A. Tarasov, M. Wipf, W. Fu, M. Calame and C. Schönenberger Silicon-Based Ion-Sensitive Field-Effect Transistor Shows Negligible Dependence on Salt Concentration at Constant pH. *ChemPhysChem 13*, 1157–1160 (2012)

5. K. Bedner, V.A. Guzenko, A. Tarasov, M. Wipf, R.L. Stoop, D. Just, S. Rigante, W. Fu, R.A. Minamisawa, C. David, M. Calam, J. Gobrecht and C. Schönenberger. pH Response of Silicon Nanowire Sensors: Impact of Nanowire Width and Gate Oxide. *Sensors and Materials 25*, 567–576 (2013)

6. M. Wipf, R.L. Stoop, A. Tarasov, K. Bedner, W. Fu, I.A. Wright, C.J. Martin, E.C. Constable, M. Calame and C. Schönenberger. Selective Sodium Sensing with Gold-Coated Silicon Nanowire Field-Effect Transistors in a Differential Setup.*ACS Nano 7*, 5978–5983 (2013)

7. P. Livi, K. Bedner, A. Tarasov, M. Wipf, Y. Chen, C. Schönenberger and A. Hierlemann. A Verilog-A model for silicon nanowire biosensors: From theory to verification. *Sensors and Actuators B: Chemical*, 293–300 (2013)

8. W. Fu, C. Nef, A. Tarasov, M. Wipf, R.L. Stoop, O. Knopfmacher, M. Weiss, M. Calame and C. Schönenberger. High mobility graphene ion-sensitive field-effect transistors by noncovalent functionalization. *Nanoscale 5*, 12104–12110 (2013)

9. K. Bedner, V.A. Guzenko, A. Tarasov, M. Wipf, R.L. Stoop, S. Rigante, J. Brunner, W. Fu, C. David, M. Calame, J. Gobrecht and C. Schönenberger. Investigation of the dominant 1/f noise source in silicon nanowire sensors. *Sensors and Actuators B: Chemical 191*, 270 – 275 (2014)

Conference Proceedings

1. W. Fu, C. Nef, A. Tarasov, M.Wipf, R.L. Stoop, O. Knopfmacher, M. Weiss, M. Calame and C. Schönenberger. Sensing with liquid-gated graphene field-effect transistors. Conference on Nanotechnology *(12th IEEE-NANO)*. 2012; pp 1–2

2. M. Wipf, R.L. Stoop, A. Tarasov, K. Bedner, W. Fu, M. Calame and C. Schönenberger. Potassium sensing with membrane-coated silicon nanowire field-effect transistors. *Transducers Eurosensors XXVII:* The 17th International Conference on Solid-State Sensors, Actuators and Microsystems. 2013; pp 1182–1185

3. S. Rigante, M. Wipf, A. Tarasov, D. Bouvet, K. Bedner, R.L. Stoop and A. Ionescu. Integrated FinFET based sensing in a liquid environment. *Transducers Eurosensors XXVII:* The 17th International Conference on Solid-State Sensors, Actuators and Microsystems. 2013; pp 681–684

4. P. Livi, M. Wipf, A. Tarasov, R.L. Stoop, K. Bedner, J. Rothe, Y. Chen, A. Stettler, C. Schönenberger and A. Hierlemann. Silicon nanowire ion-sensitive field-effect transistor array integrated with a CMOS-based readout chip. *Transducers Eurosensors XXVII:* The 17th International Conference on Solid-State Sensors, Actuators and Microsystems. 2013; pp 1751–1754

5. S. Rigante, P. Scarbolo, D. Bouvet, M. Wipf, A. Tarasov, K. Bedner and A. Ionescu. High-k dielectric FinFETs towards sensing integrated circuits. 14th International Conference on Ultimate Integration on Silicon *(ULIS)*. 2013; pp 73–76

6. S. Rigante, M. Wipf, A. Bazigos, K. Bedner, D. Bouvet and A. Ionescu. Finfet with fully PH-responsive HfO_2 as highly stable biochemical sensor. IEEE 27th International Conference on Micro Electro Mechanical Systems *(MEMS)*. 2014; pp 1063-1066

International Conference Contributions

1. M. Wipf, A. Tarasov, O. Knopfmacher, K. Bedner, W. Fu, M.Calame and C. Schönenberger". Silicon Nanowire FET sensor platform for versatile sensing applications. *Sensors & their Applications XVI*. 2011 (poster)

2. M. Wipf, A. Tarasov, R.L. Stoop, O. Knopfmacher, K.Bedner, J. Kurz, A. Odedra, W. Fu, M. Calame and C. Schönenberger. Sensing with dual-gated silicon nanowire field-effect transistors. 14th International Meeting on Chemical Sensors *IMCS*. 2012 (talk)

3. M. Wipf, R.L. Stoop, A. Tarasov, K.Bedner, W. Fu, M. Calame and C. Schönenberger. Silicon Nanowire Ion-Sensitive Field-Effect Transistors for Sensing Applications. *Transducers Eurosensors XXVII:* The 17th International Conference on Solid-State Sensors, Actuators and Microsystems. 2013 (poster)

Curriculum Vitae

Mathias Wipf

Wielandplatz 8
4054 Basel
Switzerland
☎ +41 (0)79 681 65 32
✉ mathias.wipf@gmail.com

Personal Information

Date of birth	November 20, 1985
Place of birth	Arlington Heights IL, USA
Nationality	Swiss and US-American
Hometown	Dorf, ZH
Family status	Single

Education

10/2010–05/2014	**PhD in Experimental Physics**, *Nanoelectronics group (Prof. Dr. Christian Schönenberger), University of Basel, Switzerland*. Topic: Chemical and Biochemical Sensors Based on Silicon Nanowire Field-Effect Transistor Arrays
2008–2010	**Master of Science**, *Nanoscience (major physics), University of Basel, Switzerland*. Topic: Dual-gated field-effect transistors for sensing applications.
02/2009–04/2009	Project thesis, *Interdisciplinary Nanoscience Center (Prof. Dr. Jørgen Kjems), Aarhus University, Denmark*. Topic: Nanoparticles for drug delivery.
2005–2008	**Bachelor of Science**, *Nanoscience, University of Basel, Switzerland*.
2000–2004	**Matura**, *Kantonsschule Schaffhausen, Switzerland*.

Professional Experience

10/2010–present	**Research and Teaching Assistant**, *Department of Physics, University of Basel*.
07/2008–09/2008	**Internship**, *Rio Tinto Alcan*, Research & Development at EMPA labs, Thun. Topic: Carbon Nanotube reinforcement of aluminium.

115

List of Symbols & Abbreviations

$[B]_0$	Ligand surface density
ϵ	Relative permittivity
Λ_D	Debye length
μ	Mobility
μ_i	Chemical potential of species i
ν	Surface group density
Ψ	Electrostatic potential
Ψ_0	Surface potential
σ_0	Surface charge
A	Analyte
$a_{H_b^+}$	Proton activity in the bulk solution
$a_{H_s^+}$	Proton activity at the surface
AB	Analyte-ligand pair
B	Ligand
C_{dl}	Double layer capacitance
C_{ox}	Oxide capacitance
C_s	Surface buffer capacitance
e	Elementary charge
E_F	Fermi energy
F	Faraday constant
G	Conductance
g_m	Transconductance
I_{sd}	Source-drain current
k_a, k_d	Association, dissociation rate constant
k_b	Boltzmann constant $1.38 \cdot 10^{-23}$ J/K
K_D	Dissociation equilibrium constant
L	Channel length, Linker molecule
N_A	Avogadro constant $6.022 \cdot 10^{23}$ mol^{-1}
N_a	Number of charge carriers
N_i	Intrinsic carrier concentration
N_{ot}	Number of trap states

N_s	Number of surface sites
$R(t)$, R_{max}	Response, maximum response
S	Subthreshold swing
S_I	Current noise power spectral density
S_{JN}	Johnson-Nyquist (thermal) noise power spectral density
$S_{Q_{ox}}$	Oxide charge noise power spectral density
S_{VG}	Gate referred voltage noise
T	Temperature [K]
t	Channel Tickness
V_{fb}	flatband voltage
V_g	Gate voltage
V_{lg}	Liquid gate voltage
V_{sd}	Source-drain voltage
V_{th}	Threshold voltage
W	Channel width
z_i	Charge number of ion i
ALD	Atomic layer deposition
BioFET	Biologically modified field-effect transistor
CMOS	Complementary metal-oxide semiconductor
EBL	Electron beam lithography
EDL	Electric double layer
eV	Electron volt
FET	Field-effect transistor
ISFET	Ion-sensitive field-effect transistor
LOD	Limit of detection
MeOH	Metal oxide
MOSFET	Metal oxide semiconductor field-effect transistor
NW	Nanowire
OHP	Outer Helmholtz plane
PDMS	Polydimethylsiloxane
pI	Isoelectric point
PMMA	Poly(methyl methacrylat)
PZC	Point of zero charge
RMS	Root mean square
SAM	Self-assembled monolayer
SiNW	Silicon nanowire
SiNWFET	Silicon nanowire field-effect transistor
SNR	Signal to noise ratio
SOI	Silion on insulator

TMAH   Tetramethylammonium hydroxide

Acknowledgements

At this point I would like to thank all the people who supported me during my PhD and helped me finish this thesis. First of all, a very special thanks goes to my supervisors Christian Schönenberger and Michel Calame. In countless meetings I could profit from your inspiring keen perception and your analytical way of thinking. I'm extremely glad that I had the possibility to be a part of your group. Having a perfect mix of support, pressure and freedom led to a perfect working atmosphere. A huge thanks goes to the nanowire sensor team. Especially to Ralph Stoop, the perfect parter; As busy as a bee, unremittingly motivated, always in for endless fruitful discussions and a good friend who never refuses a beer! Alexey Tarasov who taught me how to sell our results, turn them into good results and finally have a reason to celebrate with a "good-results schnapps". He is a true friend who showed me how to believe in myself and my abilities. Oren Knopfmacher, the basis and founder of the "Prolo Team" from whom I've learned all cleanroom and lab techniques. Without his experience the project would not have advanced so far. Wangyang, the master of graphene who was always there for discussions. It has been fun working with all of you!

I like to thank all our collaborators who helped getting the project working. A special thanks goes to Kristine Bedner and Vitaliy Guzenko for providing us with thousands of nanowires, each batch of better quality. The surface chemists: Jolanta Kurz and Johann Grognux. The synthesis chemists: Iain Wright, Colin Martin, Steffen Müller and Edwin Constable. The molecular pharmacists: Giulio Navarra, Meike Scharenberg, Arjan Odedra, Florian Binder and Beat Ernst. The physical engineers: Sara Rigante and Paolo Livi. The biomedical engineers: Bernd Dielacher and Janos Vörös. The industrial partner: Matthias Streiff. Thank you all so much for the good cooperation, it was a very enriching experience and a lot of fun!

I am grateful to Prof. Dr. Carlotta Guiducci and Prof. Dr. Shili Zhang for being co-referees of my thesis.

Further I like to thank the other members of the room temperature office: Cornelia Nef for the loud and detailed narrations and discussions about tiny

little details of sports gear. You have been a great mate ever since the beginning of my scientific career! Jan Brunner for launching an interesting discussion from everything imaginable just to keep himself from working. From him I learned a lot about science and anything and everything. Toni Fröhlich, although I spent more time searching for him than actually talking to him was a true enrichment for the working atmosphere in the office. Anton Vladyka for teaching me all sorts of computer tricks and Kishan Thodkar for his enthusiasm and his cheerful character.

I owe thanks to the rest of the Schönenberger group: Andreas Baumgartner, Claire Barrett, Minkyung Jung, Romain Maurand Peter Makk, Markus Weiss, Gulibusitan Abulizi, Hagen Aurich, Samuel d'Hollosy, Lukas Hofstetter, Gabor Fabian, Frank Freitag Jörg Gramich, Clevin Handschin, Mihai-Cezar Harabula, Thomas Hasler, Stefan Nau, Vishal Ranjan, Peter Rickhaus, Julia Samm, Jens Schindele, Samuel Vogel, Simon Zihlmann. We had so much fun together! I will never forget the adventurous group excursions and ski trips.

I thank the technical and administrative staff Heinz Breitenstein, Silvester Jakob, Michael Steinacher, Astrid Kalt and Barbara Kammermann. I thank Liz, Laura, Doris, Felix and Sergei for proofreading my thesis and Cyrill for his help with the illustrations and cover picture. Further I thank my former flat-mates Lucas, Lukas, Martin and Philipp for a wonderful time off the job.

A very special thanks goes to my family for supporting me and believing in me for all these years. Lara, thank you for being so close, enduring me when I gave you a hard time and for showing me how to look at the world from another perspective.